

# 4,4'-bis(carbazol-9-yl)biphenyl (CBP): beyond the single molecule picture using ab-initio methods

Zur Erlangung des akademischen Grades eines

**DOKTORS DER NATURWISSENSCHAFTEN**

**(Dr. rer. nat.)**

von der KIT-Fakultät für Chemie und Biowissenschaften  
des Karlsruher Instituts für Technologie (KIT)

genehmigte

**DISSERTATION**

von

**M.Sc. Rodrigo Cortés Mejía**

1. Referent: PD Dr. Sebastian Höfener

2. Referent: Prof. Dr. Marcus Elstner

Tag der mündlichen Prüfung: 26. Oktober 2022



# Abstract

In this thesis, 4-4'-bis(carbazol-9-yl)biphenyl, CBP, is investigated using accurate and efficient quantum chemical methods to identify key factors for the correct description of excited states. Investigation of local-minima geometries reveal that the charge transfer states of CBP are accurately described by the *GW*-BSE approach, while time-dependent density functional theory yields incorrect state ordering. It is also shown that the relative orientation of carbazole and phenyl groups causes smaller excitation energy shifts, while the bond distance of the biphenyl moiety has a stronger effect. These observations are supported by an ensemble approach used to simulate the temperature dependence of absorption and emission spectra. The statistical analysis indicates that the reduction of charge-transfer absorption bands is related to a large spread in the distribution of oscillator strengths, which reflects considerable changes in the transition moments. The excited-state properties of CBP dimers are also assessed. Using PNO-ADC(2) reference calculations, it is shown that TD-LC-DFTB is a good alternative to compute excitonic couplings employing the two-state approximation. A comparison of relaxed and unrelaxed dimer geometries from an MD-equilibrated CBP slab reveal that constrained structural optimization can significantly improve geometries, and thus couplings, while preserving monomer arrangements from the bulk. Additionally, the influence of explicit environment on couplings is investigated using the FDE approach on CBP clusters. The shifts in excitonic couplings due to polarization from the environment highlight the importance of the bulk structure.



# Kurzfassung

In dieser Arbeit wird 4-4'-bis-(carbazol-9-yl)-biphenyl, CBP, mit akkuraten und effizienten quantenchemischen Methoden untersucht, um Schlüsselfaktoren für die korrekte Beschreibung angeregter Zustände zu identifizieren. Die Untersuchung der Geometrien lokaler Minima zeigt, dass die *Charge-Transfer*-Zustände von CBP durch den GW-BSE-Ansatz mit hoher Genauigkeit beschrieben werden, während die zeitabhängige Dichtefunktionaltheorie eine falsche Reihenfolge der angeregten Zustände liefert. Es wird auch gezeigt, dass die relative Orientierung der Carbazol- und Phenylgruppen kleinere Verschiebungen der Anregungsenergie verursacht, während der Bindungsabstand der Biphenyleinheit einen stärkeren Effekt hat. Diese Beobachtungen werden durch einen Ensemble-Ansatz unterstützt, der zur Simulation der Temperaturabhängigkeit von Absorptions- und Emissionsspektren verwendet wird. Die statistische Analyse zeigt, dass die Verringerung der *Charge-Transfer*-Absorptionsbanden mit einer großen Streuung in der Verteilung der Oszillatorstärken zusammenhängt, die erhebliche Veränderungen in den Übergangsmomenten widerspiegelt. Die Eigenschaften von CBP-Dimeren im angeregten Zustand werden ebenfalls untersucht. Anhand von PNO-ADC(2)-Referenzrechnungen wird gezeigt, dass TD-LC-DFTB eine gute Alternative zur Berechnung der exzitonischen Kopplungen unter Verwendung einer Zweizustandsnäherung ist. Ein Vergleich von relaxierten und nicht relaxierten Dimergeometrien aus einer MD-ausgeglichenen CBP-Auswahl zeigt, dass eine Strukturoptimierung mit Einschränkungen die Geometrien und damit die Kopplungen erheblich verbessern kann, während die Monomeranordnungen aus der Masse erhalten bleiben. Zusätzlich wird der Einfluss der expliziten Umgebung auf die Kopplungen mit Hilfe des *frozen density embedding* Ansatzes an CBP-Clustern untersucht. Die Verschiebungen der exzitonischen Kopplungen aufgrund der Polarisierung durch die Umgebung unterstreichen die Wichtigkeit der Berücksichtigung einer Umgebungsstruktur.



# Contents

<b>Abstract</b>	<b>i</b>
<b>Kurzfassung</b>	<b>iii</b>
<b>1 Introduction</b>	<b>1</b>
<b>2 Theoretical background</b>	<b>5</b>
2.1 <i>Ab initio</i> methods . . . . .	5
2.1.1 Electron correlation . . . . .	7
2.1.2 Configuration interaction . . . . .	8
2.1.3 CIS(D) method . . . . .	9
2.1.4 The algebraic-diagrammatic construction scheme . . . . .	10
2.1.5 Scaled opposite-spin ADC(2) . . . . .	12
2.1.6 Pair natural orbitals . . . . .	13
2.2 Density functional theory . . . . .	13
2.2.1 Time-dependent DFT . . . . .	16
2.2.2 Considerations on TD-DFT and charge transfer excitations . . . . .	20
2.3 The <i>GW</i> method and the Bethe-Salpeter equation . . . . .	21
2.3.1 The single-particle Green's function approach . . . . .	21
2.3.2 Hedin's equations and the <i>GW</i> approximation . . . . .	23
2.3.3 The Bethe-Salpeter equation . . . . .	24
2.4 Frozen density embedding (FDE) . . . . .	26
<b>3 Properties of CBP in the single molecule picture</b>	<b>31</b>
3.1 Computational details . . . . .	31
3.1.1 Ground-state geometry optimizations . . . . .	31
3.1.2 Ionization energies . . . . .	32
3.1.3 Excited-state calculations using TD-DFT and <i>GW</i> -BSE . . . . .	32
3.2 CBP in the electronic ground state . . . . .	33
3.2.1 CBP ionization energies . . . . .	35

3.3	Singlet vertical excitations . . . . .	39
3.3.1	Method comparison: TD-DFT and <i>GW</i> -BSE . . . . .	39
3.3.2	Absorption spectra of stable rotamers . . . . .	42
3.3.3	The charge-transfer state in CBP . . . . .	43
3.4	Relaxed excited-state geometries and fluorescence . . . . .	46
3.4.1	Emission and charge-transfer states . . . . .	49
<b>4</b>	<b>Effects of rotational conformation of CBP on excited-state properties</b>	<b>51</b>
4.1	Computational details . . . . .	52
4.1.1	Rotation scan of CBP and electronic structure calculations . .	52
4.1.2	Boltzmann averaging to simulate temperature-dependent spectra	53
4.2	Fragment charge analysis . . . . .	53
4.3	Temperature dependence of absorption spectra . . . . .	55
4.3.1	Statistical analysis: ground-state rotamers . . . . .	57
4.3.2	Transition densities of vanishing and non-vanishing bands . . .	63
4.4	Effects of rotational conformation and temperature on emission of CBP	64
<b>5</b>	<b>CBP dimers: excitonic coupling in different environments</b>	<b>69</b>
5.1	Computational details . . . . .	69
5.1.1	Geometry optimizations . . . . .	70
5.1.2	Excitation energies . . . . .	71
5.1.3	Frozen density embedding . . . . .	72
5.1.4	Excitonic coupling . . . . .	73
5.2	Gas-phase CBP dimers . . . . .	74
5.2.1	Optimized geometries . . . . .	74
5.2.2	Excitation energies . . . . .	76
5.2.3	Excitonic couplings . . . . .	79
5.3	Influence of dimer geometry . . . . .	80
5.3.1	Excitation energies . . . . .	81
5.3.2	Excitonic couplings . . . . .	84
5.4	Electronic polarization due to explicit environment . . . . .	88
5.4.1	Relaxed embedded dimers . . . . .	90
5.4.2	Excitonic couplings and embedding . . . . .	91
<b>6</b>	<b>Summary and conclusion</b>	<b>95</b>

---

<b>A Appendix</b>	<b>99</b>
A.1 Singlet excitation energies of CBP dimers . . . . .	101
A.1.1 Excitation energies of gas-phase dimers . . . . .	101
A.1.2 Excitation energies of sampled dimers: unrelaxed MD geometries	107
A.1.3 Excitation energies of sampled dimers: relaxed DFT geometries	111
A.1.4 Excitation energies of molecular clusters . . . . .	115
A.2 Excitonic couplings of CBP dimers . . . . .	123
A.2.1 Excitonic couplings of sampled dimers: comparison of MD and DFT geometries . . . . .	123
A.2.2 Excitonic couplings of dimers at the centre of CBP clusters with and without environment . . . . .	124
A.3 Structural parameters of unrelaxed MD and relaxed DFT geometries of sampled dimers . . . . .	125
<b>Bibliography</b>	<b>127</b>
<b>Acronyms and Abbreviations</b>	<b>135</b>
<b>Permissions to Print</b>	<b>137</b>
<b>List of Publications</b>	<b>139</b>
<b>Acknowledgments</b>	<b>141</b>



# 1 Introduction

Research on organic light emitting diodes, OLEDs, has become an increasingly active field in past years due to their properties and potential applications in lighting and display technologies. This has led to the development of several subclasses, with phosphorescent OLEDs, PhOLEDs, among the most efficient.<sup>[1]</sup> PhOLEDs use organometallic compounds as emitters embedded in an organic semiconductor matrix.<sup>[2]</sup> However, they suffer from degradation through various processes that limit their lifetime by gradually decreasing their luminosity.<sup>[3]</sup> One of the mechanisms proposed to explain degradation through molecular aggregation involves the interaction of excitons and polarons generated in host molecules by electrical driving.<sup>[4]</sup> Studying degradation processes in OLEDs and PhOLEDs is not a trivial task, as they span through a wide range of time and length scales. This highlights the need to develop a multi-scale approach capable of giving a detailed description of PhOLED degradation. This thesis aims to identify key aspects for the accurate description of excited-state properties of 4-4'-bis(carbazol-9-yl)biphenyl, CBP, and to help establish a balanced framework of methods to compute these properties.

In general, OLEDs consist of thin layers of organic materials sandwiched between two electrodes, all deposited on a substrate, which emit light when subjected to electrical driving.<sup>[5]</sup> A special variant are PhOLEDs, which use organometallic compounds as triplet emitters like Ir(ppy)<sub>3</sub> or Ir(Fppy)<sub>2</sub>(acac).<sup>[2]</sup> These are embedded into so-called host materials, which work as a dispersion matrix for the emitters while ensuring appropriate transport of charge carriers and excitons towards the emissive dopant. One essential requirement for host molecules is that the lowest triplet excited state, T<sub>1</sub>, should be higher in energy than the phosphorescent emitter to avoid back transfer.<sup>[6,7]</sup> Such characteristic becomes more challenging when using blue emitters, as they typically have triplet energies of 2.7 eV or higher.<sup>[8]</sup>

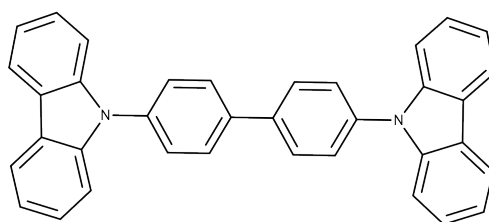


Figure 1: 4-4'-bis(carbazol-9-yl)biphenyl, CBP

At the same time, host materials can be used to fulfill charge transport roles. Depending on the type of charge carrier, they are classified in three categories: hole-, electron- and bipolar transport. In particular, hole-transport materials are used for positive polaron/charge mobility. Typical molecules employed for this purpose should contain electron-donating groups, provide a good hole mobility, and have a relatively high glass transition temperature to ensure thermal stability. The characteristics of their highest occupied and lowest unoccupied molecular orbitals, HOMO and LUMO respectively, should also be considered: the HOMO should guarantee a low hole-injection barrier into the emission layer, EML, while the LUMO should inhibit the passing of electrons from the EML back to the hole-transport layer.<sup>[8]</sup>

Carbazole based compounds are often used as host materials given their relative high triplet energies, typically in the 2.7-3.3 eV range.<sup>[9]</sup> One particularly common hole-transport host molecule is 4-4'-bis(carbazol-9-yl)biphenyl, CBP, shown in Fig. 1. It is composed of two carbazole moieties, one at each end of a biphenyl group. Blue-green and green PhOLEDs containing CBP have been reported to have remarkable efficiencies of up to 89.1 cd A<sup>-1</sup>.<sup>[10]</sup> In contrast, using CBP as host for typical blue emitters will lead to poor device performance because the higher triplet energies of the dopant lead to inefficient host-guest energy transfer.<sup>[8]</sup>

The use of device architectures with embedded organometallic phosphorescent emitters has led to PhOLEDs with internal quantum efficiencies close to 100%.<sup>[1]</sup> Still, PhOLEDs have some stability problems that make them susceptible to degradation, significantly reducing their lifetimes.<sup>[3,11,12]</sup> The consequences of OLED and PhOLED degradation can be typically observed as a decrease in their luminosity. Among the different causes for loss of luminance, intrinsic degradation remains the most problematic, as it occurs from long-term operation under normal circumstances.<sup>[3]</sup> One such mechanism is proposed to involve aggregation of hole-transport host molecules

---

used in PhOLEDs, which occurs through the interaction of excitons and positive polarons generated by electrical driving, hence the name exciton-polaron induced aggregation, EPIA.<sup>[4,13-17]</sup> The problem of EPIA is reported to be most severe in blue and blue-green PhOLEDs, where wide band-gap materials like CBP are typically used as hosts.<sup>[18-20]</sup>

The study of OLED and PhOLED degradation processes requires the combination of different methods that can correctly model the generation of reactive charged-excited species, the interactions with their environment, their transport properties and rate constants. High-level quantum chemical methods are amongst the fundamental ingredients to investigate excited-state species involved in normal PhOLED operation, and degradation processes. These approaches can also provide reference data to parametrize and validate low-scaling methods, which can simulate considerably larger systems.<sup>[21]</sup> On the other hand, highly-accurate methods can become very expensive due to the computational scaling with system size. Thus, one of the aims of this work is to help establish a framework of excited-state methods that offer good balance between cost-effectiveness and accuracy.

Time-dependent density functional theory, TD-DFT, is a widespread method for excited-state calculations due to its relative ease of use, and computational efficiency. It allows calculations of relatively large systems yielding results that can be in good agreement with experiments, with typical errors between 0.2 and 0.4 eV for valence excited-states.<sup>[22,23]</sup> Additionally, it is widely available in most popular computational chemistry codes, with implementations that allow the calculation of oscillator strengths and analytic gradients. TD-DFT results can have a strong dependence on the choice of exchange-correlation functional, and the type of excitation being described.<sup>[24]</sup> Some problematic cases include Rydberg states, excitations in extended  $\pi$ -systems, double excitations and charge-transfer, CT, states.<sup>[25-28]</sup> A cost-effective alternative to TD-DFT is the Bethe-Salpeter equation based on the single-particle Green's function, *GW*-BSE. With a scaling similar to TD-DFT, the *GW*-BSE method can yield excitation energies with typical errors of 0.1-0.3 eV, while also avoiding problems with Rydberg or CT states.<sup>[23,29-31]</sup> Though high-level wavefunction-based methods can be used to obtain very accurate excitation energies, their inherent computational scaling restricts their use to small systems. Nonetheless, local correlation approaches, like pair natural orbitals, PNOs, have become a viable alternative to accurately describe excited states in larger systems, like CBP, without significant loss in accuracy.<sup>[32]</sup> In

case of CBP, the accurate description of CT states is particularly important as there is evidence of a low-lying excited state with charge-transfer character.<sup>[33]</sup>

This thesis aims to characterize CBP for the accurate description of excited-state properties, and to help establish a balanced framework of accurate and efficient quantum chemical methods that can correctly describe excited states and excitonic couplings of CBP. The main research objectives are:

1. The structural determination of ground- and excited-state geometries of the CBP monomer in gas phase.
2. The benchmark of different quantum-chemical methods for excited-state computations.
3. The assessment of influence of molecular conformation on absorption and emission.
4. The study of the influence of different environments on dimer structure and excitonic couplings.
5. The evaluation of environmental effects on dimers embedded inside molecular clusters.

This thesis is structured as follows. Chapter 2 gives a brief review of the main quantum chemistry methods used in the present work, which consist of CIS(D), ADC(2), DFT, TD-DFT and *GW*-BSE. The frozen density embedding approach in quantum chemical calculations is also included. Chapter 3 investigates the electronic properties of CBP as a single molecule in the gas phase. It is shown that the CT-type state is poorly describe by TD-DFT, while *GW*-BSE manages to give a correct description of both absorption and emission. Chapter 4 presents a study of the effects of rotational conformation on absorption and emission spectra of the CBP molecule. The analysis is extended by using Boltzmann averaging to simulate temperature-dependent effects of fragment orientation in a free-rotating CBP picture. Chapter 5 explores the effects of different environments on the excitation energies and excitonic couplings of CBP dimers. Here, the frozen density embedding approach is used to assess the effects of environment polarization on dimers inside CBP clusters. Finally, a summary and the main conclusions of this thesis are given in Chapter 6.

## 2 Theoretical background

The scope of this chapter is to motivate the choice of methods used in this work. The chapter is split into four main parts: Section 2.1 focuses on the wave function based methods for excited-states. Section 2.2 deals with Density Functional Theory. Section 2.3 describes the many-body Green's function formalism and the Bethe-Salpeter equation. Finally, Section 2.4 introduces the frozen density embedding approach as an effective method to account for relevant environmental effects.

### 2.1 *Ab initio* methods

The time-independent Schrödinger equation describes the quantum state of non-relativistic systems in a stationary state:

$$\hat{H}\Psi = E\Psi . \quad (1)$$

Here,  $E$  is the energy of the system,  $\Psi$  is the wave function, and  $\hat{H}$  is the Hamilton operator for a many electron-system, which under the Born-Oppenheimer (BO) approximation reads:

$$\hat{H} = \underbrace{-\sum_{i=1}^n \frac{1}{2} \nabla_i^2}_{\hat{T}_e} - \underbrace{\sum_{i=1}^n \sum_{I=1}^N \frac{Z_I}{r_{iI}}}_{\hat{V}_{Ne}} + \underbrace{\sum_{i=1}^{n-1} \sum_{i < j}^n \frac{1}{r_{ij}}}_{\hat{V}_{ee}} + \underbrace{\sum_{I=1}^{N-1} \sum_{I < J}^N \frac{Z_I Z_J}{r_{IJ}}}_{\hat{V}_{NN}}, \quad (2)$$

where the nuclear charges are represented by  $Z_I$  and  $Z_J$ , while  $r_{ij}$ ,  $r_{IJ}$ , and  $r_{iI}$  refer to the electron-electron, nucleus-nucleus, and electron-nucleus distance, respectively.<sup>[34,35]</sup>

The labels  $\hat{T}_e$ ,  $\hat{V}_{Ne}$ ,  $\hat{V}_{ee}$  and  $\hat{V}_{NN}$  in Eq. (2) correspond to the electron kinetic energy, nucleus-electron attraction, and electron-electron and nucleus-nucleus repulsion respectively. In the BO approximation, the motion of nuclei and electrons is decoupled

due to the large mass differences. As a result, the potential energy of the nuclei,  $\hat{V}_{NN}$ , is treated as a constant.

In the Hartree-Fock, HF, approximation, each electron occupies a spin orbital, which is the product of a spacial one-electron function  $\psi(\mathbf{r})$  and an  $\alpha$  or  $\beta$  spin function,  $\sigma$ .<sup>[36]</sup> The space and spin coordinates can be expressed together as a product, so that the spin orbital becomes

$$\phi(\mathbf{x}) = \psi(\mathbf{r})\sigma(s) \quad , \quad \sigma = \alpha, \beta . \quad (3)$$

The many-electron wave function,  $\Psi$ , is then the product of  $n$  one-electron spin orbitals

$$\Psi(\mathbf{x}_1, \mathbf{x}_2, \dots, \mathbf{x}_n) = \phi_1(\mathbf{x}_1)\phi_2(\mathbf{x}_2), \dots, \phi_n(\mathbf{x}_n) . \quad (4)$$

Following the Pauli exclusion principle, the total electronic wave function should be antisymmetric when any two electron coordinates are interchanged. This can be represented by the Slater determinant, SD:

$$\Psi_0 = \frac{1}{\sqrt{n!}} \begin{vmatrix} \phi_1(\mathbf{x}_1) & \phi_2(\mathbf{x}_1) & \dots & \phi_n(\mathbf{x}_1) \\ \phi_1(\mathbf{x}_2) & \phi_2(\mathbf{x}_2) & \dots & \phi_n(\mathbf{x}_2) \\ \vdots & \vdots & \vdots & \vdots \\ \phi_1(\mathbf{x}_n) & \phi_2(\mathbf{x}_n) & \dots & \phi_n(\mathbf{x}_n) \end{vmatrix} . \quad (5)$$

The representation of the total  $n$ -electron wave function as an SD is a good first approximation to the real many-body wave function. It can be improved to obtain the energy closest to the ground state,  $\mathcal{E}_0$ , using the variational principle:

$$\frac{\langle \tilde{\Psi} | \hat{H} | \tilde{\Psi} \rangle}{\langle \tilde{\Psi} | \tilde{\Psi} \rangle} = E \geq \mathcal{E}_0 , \quad (6)$$

which means that the energy  $E$  obtained from some trial wave function  $\tilde{\Psi}$  cannot be lower than  $\mathcal{E}_0$ , which is given only by the true wave function  $\Psi$ .<sup>[34,37]</sup>

The variation of the spin orbitals, such that the energy from the SD is minimized, represents the core of the Hartree-Fock method. This minimization leads to the

Hartree-Fock equations, of the form

$$f\phi(\mathbf{x}_i) = \varepsilon_i\phi(\mathbf{x}_i) , \quad (7)$$

where  $\varepsilon_i$  is the energy of the  $i^{\text{th}}$  spin orbital, and  $f$  is the Fock operator, which contains the kinetic energy, the potential due to the nuclei, and the Coulomb and exchange operators. The latter is a purely quantum chemical contribution and a direct consequence of the Pauli principle.

The HF equations can be solved using the Roothaan-Hall method, which introduces a set of  $K$  known basis functions,  $\chi_i$ , to express the spatial part of the spin orbitals,  $\phi_i$ , as a linear combination with expansion coefficients  $C_{\mu i}$ :

$$\phi_i = \sum_{\mu=1}^K C_{\mu i} \chi_{\mu} , \quad (8)$$

This procedure is known as linear combination of atomic orbitals (LCAO).<sup>[34,35]</sup>

Combination of the LCAO method with the HF equations results in the matrix equation

$$\mathbf{FC} = \mathbf{SC}\varepsilon , \quad (9)$$

known as the Roothaan-Hall equation. Here,  $\mathbf{F}$  is the Fock matrix,  $\mathbf{C}$  is a  $K \times K$  matrix containing the molecular orbital, MO, expansion coefficients  $C_{\mu i}$ ,  $\mathbf{S}$  contains the overlap elements between basis functions, and  $\varepsilon$  is the  $K \times K$  diagonal matrix containing the orbital energies  $\varepsilon_i$ .

A solution of the Roothaan-Hall equations requires the diagonalization of the Fock matrix, which in turn gives the expansion coefficients and the MO energies. The total electronic energy,  $E_{HF}$ , is given by the expectation value  $E_{HF} = \langle \Psi_0 | \hat{H} | \Psi_0 \rangle$ . Addition of the nuclear repulsion to  $E_{HF}$  yields the total energy of the system.<sup>[38]</sup>

### 2.1.1 Electron correlation

Electron correlation refers to the motion of electrons under the influence of all other individual moving electrons in the system. The correlation affecting electrons with same spin is known as Fermi correlation, and is introduced by the Pauli antisymmetry

principle. The correlation caused by electron-electron repulsion is known as Coulomb correlation. Fermi correlation is well described in the HF approach due to the use of SDs. On the other hand, the use of the mean-field approximation and single-particle functions in HF does not allow to model the correlated motion of electrons. Thus, HF fails to describe Coulomb correlation correctly, which is one of the major drawbacks of this approach for  $n$ -electron systems.<sup>[36,37]</sup>

The correlation energy is defined as the difference between the exact non-relativistic of the system,  $\mathcal{E}_0$ , and the HF energy,  $E_{HF}$ ,

$$E_{corr} = \mathcal{E}_0 - E_{HF} , \quad (10)$$

and it typically represents a small fraction of the exact energy, as HF can recover around 99% of the electronic energy. To correctly account for electron-electron interactions, the so-called correlated methods are used. These are also known as post-HF since they try to improve upon a HF reference solution.<sup>[34,35,38]</sup>

### 2.1.2 Configuration interaction

In the configuration interaction, CI, method the wave function is expressed as a linear combination of Slater determinants, each representing a specific electronic configuration:

$$\Psi_{CI} = C_0 \Psi_{HF} + \sum_{i,a} C_i^a \Psi_i^a + \sum_{\substack{i<j \\ a<b}} C_{ij}^{ab} \Psi_{ij}^{ab} + \sum_{\substack{i<j<k \\ a<b<c}} C_{ijk}^{abc} \Psi_{ijk}^{abc} + \dots , \quad (11)$$

where  $\Psi_{HF}$  is the HF reference and  $\Psi_i^a$ ,  $\Psi_{ij}^{ab}$ , and  $\Psi_{ijk}^{abc}$  are the excited Slater determinants due to single, double, and triple excitations, respectively. The corresponding CI coefficients are written as  $C_i^a$ ,  $C_{ij}^{ab}$ ,  $C_{ijk}^{abc}$ , etc.

The coefficients are variationally optimized, and the resulting eigenvalues correspond to the CI energies: the lowest is equal to the ground-state energy, the second lowest to the first excited state, and so on. Due to the variational principle, the total ground- and excited-state energies represent upper bounds of their true values.<sup>[35,38,39]</sup>

Calculations including all possible SDs, known as full CI, are limited to small systems, since the number of determinants is  $\sim N^n$ , with  $N$  unoccupied and  $n$  occupied spin orbitals in the reference wave function.<sup>[39]</sup> Truncated CI methods limit the number of excited determinants in the CI expansion by considering one or few types of excitations. For example, if only single excitations are considered one arrives to CI with singles, CIS, while single and double excitations result in the CISD approximation.

One drawback of truncated CI schemes is that, in contrast to full CI, they are not size consistent. Also, the description of the electron correlation as a function of the number of atoms decreases with the system size.<sup>[35,39]</sup> Excitation energies computed with CIS tend to be overestimated, with errors of up to 1 eV.<sup>[23]</sup> One source of this problem comes from using HF determinant to construct the excited SDs. The other problem stems from neglecting dynamic correlation as single excitations do not mix with the ground state, therefore not improving over HF.<sup>[22]</sup>

### 2.1.3 CIS(D) method

The CIS approximation can be improved by introducing electron correlation through a second-order perturbative correction, similar to Møller-Plesset perturbation theory to second order, MP2. The resulting method is known as CIS(D).<sup>[40,41]</sup>

In CIS(D), a triple excitation relative to the ground state requires an initial single excitation to obtain  $\Psi_{CIS}$ . Then, the triple excitation can be generated from a double promotion of orbitals not involved in the first excitation. Additionally, promoting orbitals that had been excited in the initial step will give an overall double excitation relative to  $\Psi_{HF}$ . A triples operator can be replaced by a product of the ground-state double,  $T_2$ , and excited-state single,  $U_1$ , substitutions. This gives the CIS(D) correction to a CIS state

$$E^{CIS(D)} = \langle \Psi_{CIS} | V | U_2 \Psi_0 \rangle + \langle \Psi_{CIS} | V | T_2 U_1 \Psi_0 \rangle , \quad (12)$$

where  $V$  is the perturbation potential due to correlation, and  $U_2$  is the excited state operator of the double substitutions. The first term on the right-hand side describes double excitations relative to  $\Phi_0$ . The CIS(D) correction to the excitation energies is then

$$\omega^{CIS(D)} = E^{CIS(D)} - E^{MP2} . \quad (13)$$

The CIS(D) method is size consistent, and has a computational scaling of  $N^5$ , with molecular size.<sup>[40]</sup>

### 2.1.4 The algebraic-diagrammatic construction scheme

An alternative to wave function-based methods for electronic excited states of molecules comes from the so-called electron propagator approaches, which originate from many-body Green's function theory. The algebraic-diagrammatic construction, ADC, methods have become popular for excited state calculations due to comparable accuracy to the approximate coupled-cluster method to second order, CC2, at a slightly lower computational cost.<sup>[42]</sup> The ADC scheme is based on the diagrammatic perturbation expansion of the polarization propagator, which can be done up to different orders of perturbation theory.<sup>[43]</sup>

The polarization propagator describes the time evolution of the polarization of a many-electron system, and thus contains information about the excited states of such system. The spectral representation of the polarization propagator is

$$\begin{aligned} \Pi_{pq,rs}(\omega) = & \sum_{n \neq 0} \frac{\langle \Psi_0 | c_q^\dagger c_p | \Psi_n \rangle \langle \Psi_n | c_r^\dagger c_s | \Psi_0 \rangle}{\omega + E_0^N - E_n^N} \\ & + \sum_{n \neq 0} \frac{\langle \Psi_0 | c_r^\dagger c_s | \Psi_n \rangle \langle \Psi_n | c_q^\dagger c_p | \Psi_0 \rangle}{-\omega + E_0^N - E_n^N}. \end{aligned} \quad (14)$$

where  $\Psi_0$  and  $\Psi_n$  correspond to the electronic many-body ground state, and  $n^{th}$  excited state of the system respectively.  $c_q^\dagger$  and  $c_p$  are creation and annihilation operators for electrons in the corresponding one-electron state.  $E_0^N$  and  $E_n^N$  are the ground- and excited-state energies. The polarization propagator, Eq. (14), has poles at excitations  $\omega_n = E_n^N - E_0^N$ , while the corresponding transition probabilities are given by the residues.

Eq. (14) can be written in a simplified manner as

$$\mathbf{\Pi}(\omega) = \mathbf{\Pi}^+(\omega) + \mathbf{\Pi}^-(\omega). \quad (15)$$

Since the two sums contain the same information, it is sufficient to consider  $\mathbf{\Pi}^+(\omega)$ .<sup>[43,44]</sup>

The general algebraic form of the polarization propagator is

$$\mathbf{\Pi}^+(\omega) = \mathbf{f}^\dagger(\omega - \mathbf{M})^{-1} \mathbf{x} , \quad (16)$$

where  $\mathbf{M}$  is a matrix representation of the Hamiltonian, while  $\mathbf{f}$  is the matrix of transition moments. Through diagrammatic perturbation theory,  $\mathbf{M}$  and  $\mathbf{f}$  can be expanded with respect to their perturbation order,<sup>[42,44]</sup> in agreement with the partitioning of the Hamiltonian used in Møller-Plesset theory<sup>[45]</sup>

$$\mathbf{M} = \mathbf{M}^{(0)} + \mathbf{M}^{(1)} + \mathbf{M}^{(2)} + \dots \quad (17)$$

$$\mathbf{f} = \mathbf{f}^{(0)} + \mathbf{f}^{(1)} + \mathbf{f}^{(2)} + \dots . \quad (18)$$

By using these expansions in the algebraic, or ADC, form of Eq. (16), the formal perturbation expansion of the propagator is obtained. Analysis through perturbation theory at order  $n$  allows the determination of contributions to  $\mathbf{M}$  and  $\mathbf{f}$  in increasing order, generating the hierarchy of ADC( $n$ ) approximations.<sup>[42,44]</sup>

The excitation energies are obtained by diagonalizing the  $\mathbf{M}$  matrix at a desired order of perturbation theory. Vertical excitation energies,  $\omega_n$  and corresponding eigenvectors,  $\mathbf{y}$ , are obtained by solving the Hermitian eigenvalue problem

$$\mathbf{M}\mathbf{Y} = \mathbf{Y}\mathbf{\Omega}; \mathbf{Y}^\dagger\mathbf{Y} = 1 . \quad (19)$$

The transition moments,  $\mathbf{x}$ , are calculated from  $\mathbf{y}$  by solving

$$\mathbf{x} = \mathbf{y}^\dagger \mathbf{f} . \quad (20)$$

The ADC( $n$ ) approximations are size-consistent respect to excitation energies, transition moments and excited-state properties.<sup>[42,44]</sup> By adopting the the intermediate state representation, ISR, the ADC( $n$ ) schemes allow the explicit calculation of excited-state wave functions. This enables access to excited-state properties, like nuclear gradients or dipole moments, as well as transition moments between different excited states<sup>[46]</sup>

In particular, the ADC(2) scheme considers singly excited particle-hole,  $p - h$ , states  $\Psi_i^a$ , and doubly excited states  $\Psi_{ij}^{ab}$ , known as two particle-two hole states,  $2p - 2h$ . The ADC(2) approximation is a reliable method for electronic excitations of relatively large molecules, with typical mean errors of 0.2-0.6 eV and 0.1-0.3 eV for singlet and

triplet excitations respectively, while having a moderate computational scaling of  $N^5$ .<sup>[42]</sup> Moreover, ADC(2) yields a correct description of CT excited states, making it a suitable tool to study organic semiconductors.<sup>[47]</sup>

### 2.1.5 Scaled opposite-spin ADC(2)

Spin-component scaled MP2, SCS-MP2, was proposed to improve the description of electron correlation in MP2. The justification for this approximation is rooted in the differences in contribution to the correlation energy of electrons with same, SS, and opposite, OS, spins. In the SS case, contribution to the electron is overestimated, while for SO, the contribution is underestimated. The SCS-MP2 correlation energy has the form

$$E_{SCS-MP2} = c_{OS}E_{MP2}^{OS} + c_{SS}E_{MP2}^{SS}, \quad (21)$$

where  $c_{OS}$  and  $c_{SS}$  are the scaling parameters for opposed and same spin, respectively, with values of 6/5 and 1/3, determined by fitting to high quality ab-initio data.<sup>[48]</sup>

Further simplification can be achieved by scaling only the OS component, leading to the scaled opposite-spin second order correlation energy, SOS-MP2, defined as

$$E_{SOS-MP2} = c_{SOS}E_{MP2}^{OS}, \quad (22)$$

with a scaling factor  $c_{SOS}$  of 1.3. Evaluation of the SOS-MP2 energy scales as  $N^4$ , compared to  $N^5$  of MP2, when used in combination with resolution-of-the-identity, RI, approximation, and Laplace transformations for the energy denominators.<sup>[49]</sup>

The SOS approach can be extended to the ADC(2) scheme, yielding the SOS-ADC(2) approximation, which also scales as  $N^4$ .<sup>[48,50]</sup> Removal of same-spin components in the  $2p - 2h$  configurations reduce the dimensionality of the ADC matrix, thus cutting the computational cost by reducing the prefactor of the time-determining step. SOS-ADC(2) gives excitation energies that are comparable to non-scaled CC2, with mean errors of less than 0.15 eV for singlet, and triplet excitations.<sup>[48]</sup>

### 2.1.6 Pair natural orbitals

The Pair Natural Orbital, PNO, method exploits the locality of electron correlation to ease the computational cost of correlated calculations, while introducing small errors to the correlation energy. It is based on the use of NOs to correlate each electron pair in a system of interest. The PNO approach works as follows: starting from a single-determinant reference calculation, the occupied orbitals are localized, and the electron correlation of the entire system becomes the sum over the correlation energies of the electron pairs. The pair correlation energy is estimated via a local MP2 calculation, and the electron pairs are separated into “strong” and “weak”, depending on their pair correlation value with respect to a threshold. The pairs classified as strong, are treated using the high-accuracy correlated method, *e.g.* coupled cluster or ADC(2), while for the weak group only the MP2 estimates are added to the total correlation energy. Afterwards, the virtual space for the correlation is constructed, only for strong pairs, using PNOs from the MP2 pair densities. Only the PNOs with occupation numbers above a specified threshold are kept, for which an MP2 correction for the truncation of the virtual space is calculated.<sup>[32]</sup>

## 2.2 Density functional theory

Density functional theory, DFT, provides an alternative to wave function-based methods to describe quantum systems. It is based on the idea that all properties of such systems can be obtained from the electronic density, defined as

$$\rho(\mathbf{r}_1) = n \int \cdots \int |\Psi(\mathbf{r}_1, \mathbf{r}_2, \dots, \mathbf{r}_n)|^2 d\mathbf{r}_2 \dots d\mathbf{r}_n, \quad (23)$$

with  $n$  as the number of electrons. Since the electron density depends only on three spatial and a spin variable, the DFT approach simplifies the electronic structure problem compared to wave function methods, where an  $n$  electron system has  $4n$  variables.<sup>[34,35]</sup>

The use of the electron density,  $\rho(\mathbf{r})$ , as key in determining the energy and properties of the systems was established by the Hohenberg-Kohn, HK, theorems.<sup>[51]</sup> The first HK theorem states that there is a one-to-one correspondence between  $\rho(\mathbf{r})$  and the number of electrons, the nuclear (external) potential,  $v_{\text{ext}}$ , and the ground-state energy. Thus, the total electronic ground-state energy of the system, within the BO approximation,

can be given as a functional of the ground-state density,  $\rho_0$

$$\mathcal{E}_0[\rho_0] = T[\rho_0] + E_{ee}[\rho_0] + E_{Ne}[\rho_0], \quad (24)$$

with  $T[\rho_0]$  being the electronic kinetic energy,  $E_{ee}[\rho_0]$  is the electron repulsion, and  $E_{Ne}[\rho_0]$  is the electron-nuclei interaction. The expression of the energy functional can be simplified by grouping the system independent contributions,  $T[\rho_0]$  and  $E_{ee}[\rho_0]$ , inside the Hohenberg-Kohn functional,  $F_{\text{HK}}[\rho]$

$$E_{\text{HK}}[\rho] = E_{Ne}[\rho_0] + F_{\text{HK}}[\rho] = \int \rho(\mathbf{r})V_{Ne}d\mathbf{r} + F_{\text{HK}}[\rho]. \quad (25)$$

The second HK theorem works as the DFT analogue to the variational principle, showing that the energy functional can obtain its lowest value, the ground state energy,  $\mathcal{E}_0$ , only if the the ground-state density is used,

$$\mathcal{E}_0 \leq E_{\text{HK}}[\tilde{\rho}]. \quad (26)$$

The work of Hohenberg and Kohn established an exact theory for computing the energy of any electronic system. Unfortunately, it provides no information about the exact form of  $F_{\text{HK}}[\rho]$ .

Using DFT as computational tool in chemistry was made possible by the Kohn-Sham, KS, ansatz.<sup>[52]</sup> The central idea of this contribution was to use a model system of non-interacting electrons that have the same electron density as the real, interacting system by introducing an effective potential.

For this model system, first a Hamiltonian with no electron-electron interactions is constructed by introducing an effective local potential,  $V_s(\mathbf{r})$ ,

$$\hat{H}_{\text{KS}} = -\frac{1}{2} \sum_{i=1}^n \nabla^2 + \sum_{i=1}^n V_s(\mathbf{r}_i). \quad (27)$$

The ground-state wave function of this system can be represented by a single Slater determinant, where the corresponding spin orbitals, known as Kohn-Sham orbitals,  $\varphi^{\text{KS}}$ , are determined through the KS equations,

$$f^{\text{KS}} \varphi_i^{\text{KS}} = \varepsilon_i^{\text{KS}} \varphi_i^{\text{KS}} , \quad (28)$$

where  $f^{\text{KS}}$  is the one-electron Kohn-Sham operator

$$f^{\text{KS}} = -\frac{1}{2} \nabla^2 + V_s(\mathbf{r}) . \quad (29)$$

Introduction of the non-interacting system allows to recover most of the total kinetic energy through the exact solution of the non-interacting kinetic term,  $T_s[\rho]$ , given by

$$T_s[\rho] = \sum_{i=1}^N \left\langle \varphi_i \left| -\frac{1}{2} \nabla^2 \right| \varphi_i \right\rangle . \quad (30)$$

A similar treatment can be done for the electronic potential, where one part can be approximated via semi-classical electron-electron repulsion,  $J[\rho]$ , and nuclei-electron interaction,  $E_{Ne}[\rho]$ . The remaining contributions to the total kinetic and electronic energies, which come from the real interacting system, are then grouped within the so-called exchange correlation term  $E_{xc}$ ,

$$E_{xc} = (T[\rho] - T_s[\rho]) + (E_{ee} - J_s[\rho]) . \quad (31)$$

Thus the expression of the total DFT energy takes the form

$$E[\rho] = T_s[\rho] + J[\rho] + E_{Ne}[\rho] + E_{xc} . \quad (32)$$

The expression for the electron density in terms of KS orbitals

$$\rho_s = \sum_{i=1}^n |\varphi_i^{\text{KS}}(\mathbf{r})|^2 = \rho_0 , \quad (33)$$

can be used to write the KS energy from Eq. (32) in terms of non-interacting orbitals, which can be then subjected to the variational principle relative to the independent orbitals. The resulting equation indicates that the sum of the nuclear potential,  $V_{Ne}$ , semi-classical Coulomb potential, and the potential from  $E_{xc}$ ,  $V_{xc}$ , correspond to the

effective potential,  $V_{\text{eff}}$ ,

$$\left( -\frac{1}{2}\nabla^2 + \left[ \int \frac{\rho(\mathbf{r}_2)}{\mathbf{r}_{12}} d\mathbf{r}_2 + V_{\text{xc}}(\mathbf{r}_1) - \sum_I^N \frac{Z_I}{\mathbf{r}_{1I}} \right] \right) \varphi_i^{\text{KS}} = \varepsilon_i^{\text{KS}} \varphi_i^{\text{KS}} \quad (34)$$

$$\left( -\frac{1}{2}\nabla^2 + V_{\text{eff}}(\mathbf{r}) \right) \varphi_i^{\text{KS}} = \varepsilon_i^{\text{KS}} \varphi_i^{\text{KS}} . \quad (35)$$

Also, the term  $V_{\text{eff}}$  corresponds to  $V_s$  in the KS one-electron operator in Eq. (29):

$$V_s(\mathbf{r}) \equiv \int \frac{\rho(\mathbf{r}_2)}{\mathbf{r}_{12}} d\mathbf{r}_2 + V_{\text{xc}}(\mathbf{r}_1) - \sum_I^N \frac{Z_I}{\mathbf{r}_{1I}} , \quad (36)$$

with the exchange correlation potential,  $V_{\text{xc}}(\mathbf{r})$ , defined as the functional derivative of  $E_{\text{xc}}$ :

$$V_{\text{xc}}(\mathbf{r}) \equiv \frac{\delta E_{\text{xc}}}{\delta \rho} . \quad (37)$$

The KS equations are solved in an iterative scheme, in which orbitals are expanded in sets of basis functions and the coefficients are optimized to compute the corresponding energies. The KS approach is in principle exact. However, since the exact form of  $E_{\text{xc}}$ , and thus  $V_{\text{xc}}$ , is not known, it is necessary to use of approximate forms for the exchange-correlation energy. These explicit forms are known as exchange-correlation functionals,  $E_{\text{xc}}[\rho]$ .

### 2.2.1 Time-dependent DFT

The traditional formulation of DFT, based on the HK theorems and the KS approach, can only be used to describe the properties of ground states. Nonetheless, it is possible to use a time-dependent variant of DFT, called time-dependent DFT, TD-DFT, to deal with excited-state properties of systems of interest. This is achieved by using time-dependent versions of the HK theorems, as well as the KS formulation.<sup>[22]</sup>

The time-dependent analogue for the first Hohenberg-Kohn theorem was proposed by Runge and Gross.<sup>[53]</sup> It establishes the existence of a one-to-one correspondence between the time dependent density  $\rho(\mathbf{r}, t)$  and the time dependent external potential  $V_{\text{ext}}(\mathbf{r}, t)$  up to an additive time function  $\Psi(t)$ . If this time dependent external potential determines the time dependent wave function,  $\Psi(\mathbf{r}, t)$ , then the wave function is a

functional of the time dependent electron density,  $\rho(\mathbf{r}, t)$ :

$$\rho(\mathbf{r}, t) \longleftrightarrow v_{ext}(\mathbf{r}, t) + \Psi(t) .$$

The requirement for a variational principle, is satisfied by introducing the action integral

$$A[\rho] = \int_{t_0}^{t_f} dt \left\langle \Psi(\mathbf{r}, t) \left| i\hbar \frac{\partial}{\partial t} - \hat{H}(\mathbf{r}, t) \right| \Psi(\mathbf{r}, t) \right\rangle . \quad (38)$$

When the time-dependent wave function is a solution of the time-dependent SE, then the wave function will correspond to a stationary point of the action integral, which is a functional of the time-dependent density. Hence, the exact electron density can be obtained from the Euler equation

$$\frac{\delta A[\rho]}{\delta \rho(\mathbf{r}, t)} = 0 . \quad (39)$$

The Kohn-Sham ansatz can also be formulated within a time-dependent framework by introducing a time-dependent reference system of non-interacting electrons. Like in the time-independent KS approach, this system should have an electron density,  $\rho_s(\mathbf{r}, t)$ , equal to that of the real system  $\rho(\mathbf{r}, t)$ , expressed as a sum of one-electron orbitals

$$\rho(\mathbf{r}, t) = \rho_s(\mathbf{r}, t) = \sum_{i=1}^n |\varphi_i(\mathbf{r}, t)|^2 . \quad (40)$$

These orbitals correspond to the solution of the time-dependent Schrödinger equation,

$$i \frac{\partial}{\partial t} \phi_i(\mathbf{r}, t) = \left( -\frac{1}{2} \nabla_i^2 + V_S(\mathbf{r}, t) \right) \phi_i(\mathbf{r}, t) , \quad (41)$$

where  $V_S(\mathbf{r}, t)$  is the time-dependent effective one-particle potential, which has the form

$$V_S(\mathbf{r}, t) = V(\mathbf{r}, t) + \int d^3 r' \frac{\rho(\mathbf{r}', t)}{|\mathbf{r} - \mathbf{r}'|} + \frac{\delta A_{xc}[\rho]}{\delta \rho(\mathbf{r}, t)} . \quad (42)$$

$A_{xc}[\rho]$  is known as the exchange-correlation action functional and, in a similar fashion to the time-independent formulation, the functional derivative  $\delta A_{xc}[\rho]/\delta \rho(\mathbf{r}, t)$ , will carry all unknown exchange correlation parts that need to be addressed using an approximate functional. Insertion of  $V_S(\mathbf{r}, t)$ , Eq. (42), into Eq. (41) yields the time-dependent Kohn-Sham equations, TDKS. Assuming that the density remains in its instantaneous state when a slow enough perturbation acts on it, then the functional dependence of the xc potential at time  $t$  will be only at that exact time  $t$ . This enables

the use of ground-state xc DFT functionals in combination with the time-dependent density, defining the adiabatic local density approximation.<sup>[54]</sup>

The extension of TD-DFT with linear response, LR, theory made excited-state calculations accessible to practical applications.<sup>[24]</sup> Linear response refers to the expansion of the response function up to linear terms in a perturbation, which in this case is the electric field. Thus, excitation energies can be computed from the linear time-dependent response of a time-independent, ground-state electron density to a time-dependent electric field.<sup>[22]</sup>

Considering the expansion of the density response in powers of a small perturbation

$$\delta\rho(t) = \rho(\mathbf{r}, t) - \rho_0(\mathbf{r}) = \rho_1(\mathbf{r}, t) + \rho_2(\mathbf{r}, t) + \rho_3(\mathbf{r}, t) + \dots, \quad (43)$$

the first-order response of the electron density of a KS system, also known as the TD-DFT linear response equation, takes the form

$$\delta\rho_1(\mathbf{r}, t) = \int dt' \int d\mathbf{r}' \chi_s(\mathbf{r}, \mathbf{r}', t - t') \delta V_{s1}(\mathbf{r}', t'), \quad (44)$$

where  $\chi_s$  is the density-density response function for non-interacting particles in the KS framework

$$\chi_s(\mathbf{r}, t, \mathbf{r}', t') = \left. \frac{\delta\rho[V_s](\mathbf{r}, t)}{\delta V_s(\mathbf{r}, t)} \right|_{V_s[\rho_0](\mathbf{r})}, \quad (45)$$

and  $\delta V_{s1}$  is the linearized effective potential:

$$V_{s1}[\rho](\mathbf{r}, t) = V_1(\mathbf{r}, t) + \int d\mathbf{r}' \frac{\rho_1(\mathbf{r}', t)}{|\mathbf{r} - \mathbf{r}'|} + V_{xc1}(\mathbf{r}', t). \quad (46)$$

The term  $V_{xc1}$  in Eq. (46) is the linear exchange-correlation potential. Its explicit form contains the exchange-correlation kernel  $f_{xc} = \delta V_{xc}/\delta\rho$ .

The Fourier transform of Eq. (44) leads to the frequency-dependent, non-interacting KS response function

$$\chi_s(\mathbf{r}, \mathbf{r}', \omega) = \sum_{j,k=1}^{\infty} (f_k - f_j) \frac{\varphi_j^0(\mathbf{r}) \varphi_k^{0*}(\mathbf{r}) \varphi_j^{0*}(\mathbf{r}') \varphi_k^0(\mathbf{r}')}{\omega - \omega_{jk} + i\eta}, \quad (47)$$

where  $f_k$  and  $f_j$  are the occupation numbers of the Kohn-Sham ground-state orbitals, and  $\omega_{jk}$  correspond to KS energy eigenvalue differences  $\varepsilon_j - \varepsilon_k$ . The only contributing terms are those where the sum indexes refer to one occupied and one virtual orbital, while the rest are cancelled. As a result, the absolute values of  $\omega_{jk}$  will correspond to the excitation energies of the Kohn-Sham system, which corresponds to poles in  $\chi_s$ .

Equation (44) can be related to its interacting analogue, resulting in a Dyson-type equation which connects the interacting and non-interacting response functions.<sup>[24]</sup> The corresponding Fourier transformed Dyson equation is

$$(1 - \chi_s(\omega)f_{\text{Hxc}}(\omega))\chi(\omega) = \chi_s(\omega) , \quad (48)$$

with the combined Hartree-xc kernel as

$$f_{\text{Hxc}}(\mathbf{r}, \mathbf{r}', \omega) = \frac{1}{|\mathbf{r} - \mathbf{r}'|} + f_{\text{xc}}(\mathbf{r}, \mathbf{r}', \omega) . \quad (49)$$

The frequency dependent response function, Eq. (47), has an indetermination when  $\omega = \omega_{jk}$ . This can be circumvented by forcing the left hand side of Eq. (48) to be 0 at these points, which can be done by solving the eigenvalue problem given by the linear response TD-DFT equation

$$(1 - \chi_s(\omega)f_{\text{Hxc}}(\omega))\chi(\omega) = \omega\chi_s(\omega) . \quad (50)$$

When expanded in the Kohn-Sham orbital basis, Eq. (50) acquires the form known as the Casida equation

$$\begin{pmatrix} \mathbf{A} & \mathbf{B} \\ \mathbf{B}^* & \mathbf{A}^* \end{pmatrix} \begin{pmatrix} \mathbf{X} \\ \mathbf{Y} \end{pmatrix} = \omega \begin{pmatrix} \mathbf{1} & \mathbf{0} \\ \mathbf{0} & -\mathbf{1} \end{pmatrix} \begin{pmatrix} \mathbf{X} \\ \mathbf{Y} \end{pmatrix} . \quad (51)$$

The matrix elements are defined as

$$A_{ia,jb} = (\varepsilon_a - \varepsilon_i)\delta_{ij}\delta_{ab} + \langle ib|aj \rangle + \langle ib|f_{\text{xc}}|aj \rangle \quad (52)$$

$$B_{ia,jb} = \langle ij|ab \rangle + \langle ij|f_{\text{xc}}|ab \rangle . \quad (53)$$

By assuming  $\mathbf{B} = \mathbf{0}$ , the excitations and de-excitations from linear response TDDFT become decoupled. This is known as the Tamm-Dancoff approximation, which leads

to the Hermitian eigenvalue equation

$$\mathbf{A}\mathbf{X} = \omega\mathbf{X} . \tag{54}$$

The TD-DFT/TDA approach offers a simplified computational method with accuracy comparable to TD-DFT, while avoiding the triplet instability problem.<sup>[28,55]</sup>

### 2.2.2 Considerations on TD-DFT and charge transfer excitations

Some considerations are needed when using TD-DFT to investigate excited states. For example, as with regular DFT, use of time-dependent DFT for practical applications requires the use of some approximation to the exchange-correlation potential, having a high sensitivity to the choice of the functional.<sup>[56]</sup> Another thing to take into account is the type of excitation being studied. For example, the accuracy for valence excitations is comparable with high-accuracy correlated methods.<sup>[24]</sup> On the other hand, it has severe problems when describing local valence excitations, Rydberg states, extended  $\pi$  systems, double excitations, and charge transfer, CT, excited states.<sup>[22,24]</sup>

In particular, an excitation is considered to have CT character if the transition of electrons occurs between two separated regions, meaning the particle and hole contributions are situated on different parts of the molecule.<sup>[27,57]</sup> One source of this problem is the underestimation of excitation energies. This is due to typically overbound LUMOs, caused by the KS potential. Since in TD-DFT the excitation energy is given by the energy difference between electron accepting and donating orbitals, from the  $\mathbf{A}$  matrix, Eq. (51), the lowered LUMOs yield orbital energies that are considerably underestimated. This problem can be diminished by using range-separated functionals.<sup>[26]</sup>

Another source of error stems from an incorrect  $1/R$  behaviour. This has been regarded as a type of electron transfer self-interaction error caused by using pure exchange-correlation functionals. The problem occurs because the orbital energy difference includes the electrostatic repulsion between  $a$  and  $i$  orbitals. This means that in the CT state, the electron that transitioned to orbital  $a$  experiences electrostatic repulsion from still being in orbital  $i$ . This can be avoided by using exchange-correlation functionals with exact exchange.<sup>[25,26]</sup>

A third source of error originates from so-called “triplet instabilities”, which can lead to severe underestimation of triplet energies and wrong ordering of states.<sup>[58–60]</sup> It has been observed that imaginary triplet excitation energies will occur in cases where the symmetry broken solution becomes lower in energy than the non-broken solution for the ground state. This is typical in systems with large internuclear distances. The stability of the KS determinant, with respect to triplet rotations, is quantified by the eigenvalues of the triplet part of the  $\mathbf{A} - \mathbf{B}$  matrix. If one of these eigenvalues approaches zero, the corresponding excitation energy will also be close to zero, thus significantly underestimating it. By allowing only excitations between occupied-virtual pairs, and ignoring de-excitations, the Tamm-Dancoff approximation eliminates the occurrence of imaginary excitation energies since  $\mathbf{A}$  becomes Hermitian.

## 2.3 The GW method and the Bethe-Salpeter equation

One solution to the problems encountered by TD-DFT concerning charge-transfer type excitations comes from the Bethe-Salpeter equation (BSE) based on the GW approximation, commonly known as GW-BSE. The use of this approach to assess intramolecular CT-type excitations can yield results in excellent agreement with experiments through the correct description of long-range electron-hole interactions.<sup>[29,30]</sup> In addition to this, the GW-BSE method maintains a favourable computational scaling, of  $N^4$ , making it also an appealing alternative to wavefunction based methods.<sup>[23,31,61]</sup> This method is briefly described in the following.

### 2.3.1 The single-particle Green’s function approach

Through the single-particle Green’s function, many body perturbation theory, MBPT, provides a rigorous and systematic framework to describe spectral properties of a system, which can overcome some deficiencies from DFT, like the self-interaction error, or the lack of long range polarization.<sup>[62]</sup>

Single-particle Green’s function is defined as

$$\begin{aligned} G(\mathbf{1}, \mathbf{2}) &= -i \left\langle \Psi_0^N \left| T \left[ \hat{\psi}(\mathbf{1}) \hat{\psi}^\dagger(\mathbf{2}) \right] \right| \Psi_0^N \right\rangle \\ &= -i\theta(\tau) \left\langle \Psi_0^N \left| \hat{\psi}(\mathbf{1}) \hat{\psi}^\dagger(\mathbf{2}) \right| \Psi_0^N \right\rangle + i\theta(-\tau) \left\langle \Psi_0^N \left| \hat{\psi}^\dagger(\mathbf{2}) \hat{\psi}(\mathbf{1}) \right| \Psi_0^N \right\rangle, \end{aligned} \quad (55)$$

where, for a system of  $N$  electrons,  $|\Psi_0^N\rangle$  is the many-electron ground state,  $\hat{\psi}^\dagger$  is the field operator that creates an electron at point  $\mathbf{r}$ , and  $T$  is the time ordering operator. Considering  $\tau = t_1 - t_2$ ,  $\theta(\tau)$  is the Heaviside step function which is equal to 1 for  $\tau > 0$  and 0 otherwise. For simplicity, the spacial  $\mathbf{r}$ , spin  $\sigma$ , and time  $t$  coordinates are collected under the notation  $\mathbf{1} = (\mathbf{r}, \sigma, t)$ . When  $t_1 > t_2$ , the single-particle Green's function gives the probability amplitude that a hole created at  $\mathbf{r}_1 t_1$  will propagate to  $\mathbf{r}_2 t_2$ , while  $t_2 > t_1$  yields the probability amplitude of an electron added at  $\mathbf{2}t_2$  propagating to  $\mathbf{1}t_1$ . Thus the single-particle Green's function is related to photoemission and inverse photoemission.<sup>[63]</sup>

By introducing a complete set of  $(N \pm 1)$  electron states ( $f_A(\mathbf{x}) = \langle \Psi_0^N | \hat{\psi}(\mathbf{x}) | \Psi_A^{N+1} \rangle$ , and  $f_I(\mathbf{x}) = \langle \Psi_0^N | \hat{\psi}(\mathbf{x}) | \Psi_I^{N-1} \rangle$ , with  $\mathbf{x}_i = \mathbf{r}_i \sigma_i$ ), followed by a Fourier transformation, the Lehmann, or spectral, representation of the one-particle Green's function is obtained

$$\begin{aligned} G(\mathbf{x}_1, \mathbf{x}_2, \omega) &= \sum_A \frac{f_A(\mathbf{x}_1) f_A^*(\mathbf{x}_2)}{\omega - \epsilon_A + i\eta} + \sum_I \frac{f_I(\mathbf{x}_1) f_I^*(\mathbf{x}_2)}{\omega - \epsilon_I - i\eta} \\ &= \sum_S \frac{f_S(\mathbf{x}_1) f_S^*(\mathbf{x}_2)}{\omega - \epsilon_S + i\eta \operatorname{sgn}(\epsilon_S - E_F)}. \end{aligned} \quad (56)$$

$A$  and  $I$  indicate electron and hole states respectively, which are collected under  $S$ , and  $\eta$  is an infinitely small positive regularization parameter.  $E_F$  is the energy of the Fermi level, and  $\epsilon$  are the single-particle excitation energies, also known as quasiparticle, QP, energies. The term quasiparticle is used to refer to the combination of a particle, or hole, and a cloud of virtual electron-hole pairs around it, which screens the interactions with its environment. This can be regarded as the representation of the particle and the perturbation it introduces in the system.<sup>[62,64]</sup> Addition of an electron is described by  $\epsilon_A = E_A^{N+1} - E_0^N$ , while removal is  $\epsilon_I = E_0^N - E_I^{N-1}$ , which correspond to the negative of the electron affinities (EAs) and ionization potentials (IPs).<sup>[62]</sup>

As shown by Equation (56), the single-particle Green's function has singularities at the quasiparticle energies. In a non-interacting scenario, for which a non-interacting Green's function  $G_0$  is used, the Lehmann amplitudes and energies will correspond to the eigenfunctions and eigenvalues of the one-electron Hamiltonian. Thus, the QP energies will be replaced by the one-electron eigenvalues in the poles of  $G_0$ .<sup>[64]</sup>

Through the equation of motion of the one-particle Green's function the Dyson equation can be constructed<sup>[62,63]</sup>

$$G(\mathbf{1}, \mathbf{2}) = G_0(\mathbf{1}, \mathbf{2}) + \int G_0(\mathbf{1}, \mathbf{3}) \Sigma(\mathbf{3}, \mathbf{4}) G(\mathbf{4}, \mathbf{2}) d\mathbf{3}d\mathbf{4} . \quad (57)$$

The Dyson equation connects the fully-interacting one-particle Green's function,  $G(\mathbf{1}, \mathbf{2})$ , to the non-interacting  $G_0(\mathbf{1}, \mathbf{2})$ . This allows, in principle, to calculate the fully interacting  $G(\mathbf{1}, \mathbf{2})$  from a suitable reference, like a KS system, and some approximate form of the self energy,  $\Sigma$ , which contains all exchange and correlation effects.<sup>[62,63]</sup>  $\Sigma$  describes the interaction energy of the quasiparticle with the induced potential due to the screening of the electrons around the QP.<sup>[63]</sup>

### 2.3.2 Hedin's equations and the GW approximation

Hedin proposed an expansion of the Green's function and self energy in terms of the screened Coulomb potential,  $W$ , as alternative to the bare Coulomb potential.<sup>[65]</sup> This expansion allows to write the many-body problem as a set of five coupled integral equations from which the Green's function and the self-energy can be calculated. Hedin's equations have a hierarchical relation which can, in principle, be solved iteratively until self consistency is achieved. These equations relate the self-energy,  $\Sigma$ , the Dyson equation, Eq. (57), the vertex function,  $\Gamma(\mathbf{1}, \mathbf{2}, \mathbf{3})$ , the time-ordered polarization operator,  $P(\mathbf{1}, \mathbf{2})$ , and the dynamical screened interaction,  $W(\mathbf{1}, \mathbf{2})$

$$\Sigma(\mathbf{1}, \mathbf{2}) = i \int G(\mathbf{1}, \mathbf{3}^+) W(\mathbf{1}, \mathbf{4}) \Gamma(\mathbf{3}, \mathbf{2}, \mathbf{4}) d\mathbf{3}d\mathbf{4} \quad (58)$$

$$G(\mathbf{1}, \mathbf{2}) = G_0(\mathbf{1}, \mathbf{2}) + \int G_0(\mathbf{1}, \mathbf{3}) \Sigma(\mathbf{3}, \mathbf{4}) G(\mathbf{4}, \mathbf{2}) d\mathbf{3}d\mathbf{4} \quad (59)$$

$$\Gamma(\mathbf{1}, \mathbf{2}, \mathbf{3}) = \delta(\mathbf{1}, \mathbf{2})\delta(\mathbf{1}, \mathbf{3}) + \int \frac{\delta\Sigma(\mathbf{1}, \mathbf{2})}{\delta G(\mathbf{4}, \mathbf{5})} G(\mathbf{4}, \mathbf{6}) G(\mathbf{7}, \mathbf{5}) \Gamma(\mathbf{6}, \mathbf{7}, \mathbf{3}) d\mathbf{4}d\mathbf{5}d\mathbf{6}d\mathbf{7} \quad (60)$$

$$P(\mathbf{1}, \mathbf{2}) = -i \int G(\mathbf{1}, \mathbf{3}) \Gamma(\mathbf{3}, \mathbf{4}, \mathbf{2}) G(\mathbf{4}, \mathbf{1}^+) d\mathbf{3}d\mathbf{4} \quad (61)$$

$$W(\mathbf{1}, \mathbf{2}) = v(\mathbf{1}, \mathbf{2}) + \int v(\mathbf{1}, \mathbf{3}) P(\mathbf{3}, \mathbf{4}) W(\mathbf{4}, \mathbf{2}) d\mathbf{3}d\mathbf{4} . \quad (62)$$

The bare Coulomb interaction is given by  $v$ , and the superscript “+” indicates addition of a positive infinitesimal time step after  $t$ .

The dependence between Hedin's equations makes them rather difficult to solve, thus further simplifications are needed. One of such approximations is based on the assumption that only diagonal contributions of  $\Gamma(\mathbf{1}, \mathbf{2}, \mathbf{3})$  are kept. By only keeping the first term from Equation (60),  $\Gamma$  becomes

$$\Gamma(\mathbf{1}, \mathbf{1}, \mathbf{3}) = \delta(\mathbf{1}, \mathbf{2})\delta(\mathbf{2}, \mathbf{3}) , \quad (63)$$

which neglects the so-called vertex corrections. Thus, the polarizability is given by non-interacting quasielectron and quasihole pairs

$$P_0(\mathbf{1}, \mathbf{2}) = iG(\mathbf{2}, \mathbf{1})\mathbf{G}(\mathbf{1}, \mathbf{2}^+) , \quad (64)$$

and the self-energy is simplified to

$$\Sigma(\mathbf{1}, \mathbf{2}) = iG(\mathbf{1}, \mathbf{2})W(\mathbf{1}^+, \mathbf{2}) . \quad (65)$$

The screened Coulomb potential  $W$  becomes,

$$W(\mathbf{1}, \mathbf{2}) = v(\mathbf{1}, \mathbf{2}) + \int d3d4v(\mathbf{1}, \mathbf{3})\chi(\mathbf{3}, \mathbf{4})v(\mathbf{4}, \mathbf{2}) , \quad (66)$$

where  $\chi$  is the interacting electron susceptibility. The expression  $v\chi v$  represents the field created in  $\mathbf{2}$  by the rearrangement of charge in the system upon the addition of a particle, or hole, at  $\mathbf{1}$ . This is known as the  $GW$  approximation. The simplified form of the self-energy operator allows, in principle, for the calculation of the Green's function of an interacting many-electron system using the Green's function  $G_0$  of a non-interacting KS system with an effective one-electron energy-dependent potential, which is then iterated within the self-consistent scheme until convergence is achieved.<sup>[64,66]</sup> The  $GW$  method can be used to improve Kohn-Sham single-particle excitations, under the consideration that these are already a good approximation to the QP states.<sup>[62]</sup>

### 2.3.3 The Bethe-Salpeter equation

The Green's function formalism can be used to model optical processes, like photon absorption. This is done by the Bethe-Salpeter equation, which is a Dyson-like equation that connects the two-particle correlation,  $L$ , with the non-interacting correlation

function,  $L_0$ ,

$$L(1, 2, 1', 2') = L_0(1, 2, 1', 2') + \int L_0(1, 3', 1', 3)\Xi(3, 4', 3', 4)L(4, 2, 4'2')d3d3'd4d4' . \quad (67)$$

$L$  describes the propagation of the difference between the correlated and uncorrelated motions of pair states, such as a two particle, or particle-hole state.  $L_0$  describes the propagation of an electron and a hole separately. The term  $\Xi$  is known as the BSE kernel

$$i\Xi(3, 4', 3', 4) = v(3, 4)\delta(3, 3')\delta(4^+, 4') + i\frac{\partial\Sigma(3, 3')}{\partial G(4, 4')} \quad (68)$$

where  $v$  is the instantaneous Coulomb potential, and  $\Sigma$  is the self energy, defined in Eq. (58).

The BSE can be expressed in a simplified manner as

$$L = L_0 + L_0(v + \Xi)L , \quad (69)$$

which resembles TD-DFT, but instead of the two-point exchange correlation kernel  $f_{xc}(\partial V_{xc}/\partial\rho)$ , the BSE uses  $\Xi$  which has an intrinsic two-particle character. Introducing the self energy from the  $GW$  approximation gives the approximate BSE kernel

$$i\Xi(3, 4', 3', 4) = \delta(3, 3')\delta(4^+, 4')v(3, 4) - \delta(3, 4)\delta(3', 4')W(3^+, 3') . \quad (70)$$

The problem is further simplified by only considering the static limit for the Coulomb interaction,  $W(\omega = 0)$ , which is similar to the adiabatic approximation for the exchange-correlation kernel in TD-DFT. Projection of the BSE into a suitable basis leads to a matrix eigenvalue problem similar to Casida's equation Eq. (51)

$$\begin{pmatrix} \mathbf{A} & \mathbf{B} \\ \mathbf{B}^* & \mathbf{A}^* \end{pmatrix} \begin{pmatrix} \mathbf{X} \\ \mathbf{Y} \end{pmatrix} = \omega \begin{pmatrix} \mathbf{1} & \mathbf{0} \\ \mathbf{0} & \mathbf{1} \end{pmatrix} \begin{pmatrix} \mathbf{X} \\ \mathbf{Y} \end{pmatrix} , \quad (71)$$

where  $\omega$  are the excitation energies, and  $\mathbf{X}$  and  $\mathbf{Y}$  are the orbital rotation parameters.

The matrix elements of  $\mathbf{A}$  and  $\mathbf{B}$  are

$$A_{ia,jb}^{BSE} = \delta_{ij}\delta_{ab}(\varepsilon_a^{GW} - \varepsilon_i^{GW}) + (ai|bj) - W_{ij,ab}^{GW} \quad (72)$$

$$B_{ia,jb}^{BSE} = (ai|bj) - W_{ib,aj}^{GW}. \quad (73)$$

If compared to TD-DFT, the Kohn-Sham eigenvalues are replaced by the QP energies obtained from the  $GW$  approximation, and the screened Coulomb interaction  $W$  replaces the DFT exchange-correlation kernel. Solution of these equations using the QP energies, and  $W$  obtained from an underlying  $GW$  calculation defines the  $GW$ -BSE scheme. The BSE eigenvalue problem can be solved at the exact same cost as the standard TD-DFT analogue.<sup>[66]</sup>

## 2.4 Frozen density embedding (FDE)

Typical quantum-chemical methods employed to treat excited states quickly become prohibitively expensive with an increase of the size of the system. This is particularly problematic for systems where the environment has a considerable influence on the excited-state properties.<sup>[67]</sup> One possible approach is to truncate the system by using only the molecule of interest and the closest neighbours in the first solvation shell, known as the supermolecular approach.<sup>[68]</sup> An alternative approach in treating environmental effects are the so-called embedding methods. The main advantage of these methods resides in the possibility to partition the whole supermolecule into smaller interacting subsystems. This allows the accurate treatment of the subsystem of interest, while also accounting for the environment in a more approximate manner.<sup>[69]</sup> Such an approach is particularly useful when dealing with local excitations, because the surrounding subsystem can be of a smaller size, thus facilitating convergence.

The frozen density embedding, FDE, method is based on partitioning the electronic density of the total system,  $\rho_{\text{tot}}(\mathbf{r})$ ,

$$\rho_{\text{tot}}(\mathbf{r}) = \rho_I(\mathbf{r}) + \rho_{II}(\mathbf{r}) = \rho_I(\mathbf{r}) + \sum_n \rho_{II}^{(n)}(\mathbf{r}), \quad (74)$$

where  $\rho_I(\mathbf{r})$  is the density of the active subsystem, and  $\rho_{II}^n(\mathbf{r})$  refers to the subsystems that compose the environment.

Since FDE is based on DFT, the partitioning of the density allows to express the total energy of the system,  $E_{\text{tot}}$ , as the sum of the subsystem energies and their interaction energy,  $E_{\text{int}}[\rho_I, \rho_{II}]$ :

$$E_{\text{tot}} = E_I[\rho_I] + E_{II}[\rho_{II}] + E_{\text{int}}[\rho_I, \rho_{II}] . \quad (75)$$

The contribution of the subsystems to the total energy is given by the method chosen to describe each subsystem, e.g. DFT for the environment, and PNO-ADC(2) for the active subsystem.

The interaction energy,  $E_{\text{int}}[\rho_I, \rho_{II}]$ , Eq. (75), is given by

$$E_{\text{int}}[\rho_I, \rho_{II}] = \int \rho_I(\mathbf{r}) V_{\text{nuc}}^{II}(\mathbf{r}) d\mathbf{r} + \int \rho_{II}(\mathbf{r}) V_{\text{nuc}}^I(\mathbf{r}) d\mathbf{r} + E_{\text{nuc}}^{I,II} + \int \int \frac{\rho_I(\mathbf{r}) \rho_{II}(\mathbf{r}')}{|\mathbf{r} - \mathbf{r}'|} + E_{\text{xck}}^{\text{nadd}}[\rho_I, \rho_{II}] , \quad (76)$$

where  $E_{\text{nuc}}^{I,II}$  is the nuclear repulsion energy between subsystems,  $V_{\text{nuc}}^i$  is the electrostatic potential of the nuclei of system  $i$ , and the non-classical contributions to the interaction energy are included through  $E_{\text{xck}}^{\text{nadd}}[\rho_I, \rho_{II}]$ , which consists of the sum of exchange-correlation and kinetic energy contributions<sup>[68]</sup>

$$E_{\text{xck}}^{\text{nadd}}[\rho_I, \rho_{II}] = E_{\text{xck}}[\rho_I + \rho_{II}] - E_{\text{xck}}[\rho_I] - E_{\text{xck}}[\rho_{II}] , \quad (77)$$

whose evaluation requires the use of the exchange-correlation and kinetic energy functionals.

The next step in the FDE approach is to account for the effects of the interaction of the electron density of the environment,  $\rho_{II}(\mathbf{r})$ , with the density of the active system,  $\rho_I(\mathbf{r})$ .<sup>[69,70]</sup> This is done by including the interaction with the environment in the quantum-chemical description of the active subsystem. In a KS framework, the electron density of the active system,  $\rho_I(\mathbf{r})$ , can be calculated by minimizing the total FDE energy, eq. (75), with respect to  $\rho_I(\mathbf{r})$ , while fixing  $\rho_{II}(\mathbf{r})$ :

$$\frac{\delta E_I[\rho_I]}{\delta \rho_I} + \frac{\delta E_{\text{int}}[\rho_I, \rho_{II}]}{\delta \rho_I} = \mu_I . \quad (78)$$

where the Lagrange multiplier,  $\mu_I$ , is introduced to keep a constant number of electrons in the active subsystem. This yields the KS equations of the active subsystem<sup>[69,71]</sup>

$$\left[ -\frac{\nabla^2}{2} + V_{\text{KS}}[\rho_I] + V_{\text{emb}}^I[\rho_I, \rho_{II}] \right] \varphi_i^I = \varepsilon_i^I \varphi_i^I. \quad (79)$$

The term  $V_{\text{KS}}[\rho_I]$  corresponds to the  $\delta E_I/[\rho_I]\delta\rho_I$  term in Eq. (78), which is the KS potential of subsystem  $I$ , and includes the nuclear, inter-electronic Coulomb, and exchange-correlation potentials. On the other hand,  $V_{\text{emb}}^I[\rho_I, \rho_{II}]$ , known as the embedding potential, has the form

$$V_{\text{emb}}^I[\rho_I, \rho_{II}] = \frac{\delta E_{\text{int}}[\rho_I, \rho_{II}]}{\delta\rho_I} = V_{\text{nuc}}^{II}(\mathbf{r}) + \int \frac{\rho_{II}(\mathbf{r}')}{|\mathbf{r} - \mathbf{r}'|} d\mathbf{r}' + \left[ \frac{\delta E_{\text{xck}}}{\delta\rho} \Big|_{\rho_{\text{tot}}} - \frac{\delta E_{\text{xck}}}{\delta\rho} \Big|_{\rho_I} \right], \quad (80)$$

and it describes the effects of the environment on the density of the active system. It is also possible to obtain such embedding potential using a wave-function description of the active subsystem, where the electron density is represented instead with a wave function.

To fulfill Equation (74), where the total density,  $\rho_{\text{tot}}$ , from an FDE treatment is equal to the one calculated from a complete system, some requirements need to be filled. First,  $\rho_{\text{tot}}(\mathbf{r}) \geq \rho_{II}(\mathbf{r})$ . This is often troublesome for most frozen densities, because they can vary significantly depending on the region, thus not yielding the exact density. This condition ensures that the complimentary density of the active system is always positive. Second, is that the complementary form  $\rho_{\text{tot}} - \rho_{II}$  needs to be  $V$  representable.

As a solution to  $\rho_{II}(\mathbf{r})$  being too large or small, the densities of  $I$  and  $II$  can be separately determined while taking into account the frozen density of the other subsystem. One procedure to solve this system of equations is known as the freeze-thaw scheme, which is an iterative method where the density of each system is computed, one at a time, while considering the frozen densities of all other subsystems. This can be regarded as a way to account for polarization, both of the environment on the active subsystem and vice versa. The densities are updated in this manner until convergence is achieved.<sup>[68,69,71]</sup>

The FDE scheme can be employed to compute excitation energies within the formalism of linear response theory.<sup>[70,72]</sup> The effective environmental response function can be

simplified for local excited states situated in the active subsystem. However, since there is no exchange of particles between subsystems, the description of excitations with significant contributions from the environment is not always adequate.<sup>[68]</sup>



## 3 Properties of CBP in the single molecule picture

In this chapter<sup>1</sup> CBP is investigated in the the gas-phase, single molecule picture. To do so, a set of stable torsional conformers is employed to investigate electronic properties such as ionization energies, singlet vertical excitations, and emission. The ionization energy, IE, of the ground-state geometries are computed. Also, a comparison of vertical absorption transitions is done between TD-DFT, and the *GW*-BSE approaches to assess performance regarding charge-transfer type excitations reported in CBP.<sup>[33]</sup> The singlet vertical absorption spectra of the stable CBP rotamers are calculated using the *GW*-BSE method, and the charge-transfer states are further discussed. Finally, the relaxed excited-state geometries and fluorescence of the stable rotamers are studied.

### 3.1 Computational details

The TURBOMOLE computational chemistry package was used to perform all electronic structure calculations.<sup>[73,74]</sup> The details on the different job types are described in the following.

#### 3.1.1 Ground-state geometry optimizations

All ground-state geometries presented in this chapter were obtained through gas-phase geometry optimizations performed at the DFT level<sup>[75,76]</sup> using the PBE0 functional<sup>[77,78]</sup> with a medium sized grid (grid 4), and the def2-TZVP basis set.<sup>[79]</sup> The RI-*J* approximation<sup>[80,81]</sup> was employed with the corresponding auxiliary basis set.<sup>[82]</sup> The derivatives of quadrature weights for correct derivatives of the DFT energy were enabled using the `weight derivatives` option. Optimization thresholds were set to  $10^{-8}$  E<sub>h</sub> for the energy, and  $10^{-5}$  E<sub>h</sub> a<sub>0</sub><sup>-1</sup> for the gradient residual norm. Convergence

---

<sup>1</sup>Partially adapted from R. Cortés-Mejía, S. Höfener, W. Klopper, *Mol. Phys.* **2021**, *119*, e1876936

of the SCF energy of the geometries was set to  $10^{-9} E_h$ . Minima and transition states, TS, in this section were characterized through vibrational frequency analysis.<sup>[83]</sup>

#### 3.1.2 Ionization energies

The ionization energies, IE, of the optimized ground-state CBP rotamers  $R_1$ ,  $R_2$ , and  $R_3$  were calculated through the vertical and adiabatic  $\Delta$ SCF approaches. For the vertical IEs, the geometries of the stable rotamers were used for both neutral, and singly-charged cation (doublet spin multiplicity). The cations for the adiabatic IEs correspond to the relaxed geometries of the  $R_i$  rotamers with a +1 charge and doublet multiplicity. The cation structures were optimized as detailed in Sec. 3.1.1. Ionization energies were also approximated through the QP energies of the relaxed, and unrelaxed CBP radical cations, computed using the *GW* method. These calculations were carried out using a PBE0/def2-TZVP reference of the neutral, and singly-charged geometries. The energies of the HOMO and LUMO levels from the DFT references were corrected using the *GW* approximation.<sup>[84]</sup> The default value of 128 was used for the imaginary frequency integration points, and Padé approximants.

#### 3.1.3 Excited-state calculations using TD-DFT and *GW*-BSE

Reference single-point calculations of the ground-state optimized geometries were converged to at least  $10^{-9} E_h$  respect to the energy, and  $10^{-7}$  respect to changes the electron density. These were done at the DFT level using the PBE0<sup>[77,78]</sup> and the def2-TZVP basis set. The singlet vertical excitation energies were computed at the TD-DFT<sup>[85-87]</sup> level of theory, using the same functional and basis set as the ground-state calculations. Again, the RI-*J* approximation<sup>[80,81]</sup> was used with the def2-TZVP auxiliary basis.<sup>[82]</sup> Excitation energies were converged to an Euclidean residual norm of at least  $10^{-5}$ .

The geometry of the CBP rotamers was also optimized in the corresponding lowest-lying singlet excited-state. These optimizations were carried out at the TD-DFT level<sup>[87-89]</sup> using the PBE0 functional and def2-TZVP basis set. The convergence criteria was set to the same thresholds as the ground-state geometry optimizations.

The absorption and emission spectra of the CBP rotamers were also computed employing the *GW* approximation and Bethe-Salpeter equation as implemented in

TURBOMOLE.<sup>[61,90]</sup> For these calculations, a PBE0/def2-TZVP reference was used. The energies of the HOMO and LUMO were corrected by eigenvalue-only self-consistent *GW*, *evGW*, calculations employing the contour deformation, CD, variant for the self-energy, and the RI algorithm for accelerated convergence (RI-CD-*evGW* variant).<sup>[84]</sup> In this work, only the RI-CD-*evGW* variant is employed, so for simplicity the *GW*-BSE label will be used. As additional calculation parameters, the imaginary frequency integration points and Padé approximants was set to 128. The lowest 25 excitation energies were computed employing both the TD-DFT, and *GW*-BSE methods for the simulation of the absorption spectra within the experimental spectral window of 200-350 nm, or 3.5-6.0 eV.<sup>[4,91]</sup> The simulated Gaussian spectra were plotted using TURBOMOLE’s Peak ANalyzing MACHine, PANAMA,<sup>[92]</sup> with 0.10 eV for the full width at half maximum, FWHM.

## 3.2 CBP in the electronic ground state

Several CBP rotational conformers were generated through manual variation of the dihedral angles between the carbazole, CBZ, and phenyl, Ph, moieties displayed in Fig. 2: 1 carbazole (red), 2 phenyl (green), 3 phenyl (orange), and 4 carbazole (blue). The geometries of these conformers were optimized as indicated in the computational details, *cf.* Sec. 3.1.1. The colour coding is used as reference for measuring the different structural parameters of the optimized geometries: 1-2 refers to the torsion angle of carbazole 1 (atoms *a*, *b*), and phenyl 2 (atoms *c*, *d*), 2-3 is the dihedral angle between the two phenyl rings (atoms *e*, *f*, *g*, and *h*), 3-4 is the torsion angle between the opposite phenyl-carbazole pair (atoms *i*, *j*, *k*, and *l*), and 1-4 is the dihedral angle of the carbazole systems at both ends of CBP (atoms *a*, *b*, *k*, *l*). Additionally the angle of the carbazoles were measured using the  $c - b - x$ , and  $j - k - y$  points.

The relative energies with respect to the lowest lying geometry, structural parameters, and symmetries of selected optimized isomers are displayed in Tab. 1. The optimized geometries can be seen in Fig. 3. Conformer R<sub>1</sub> was identified as the global minimum rotamer. R<sub>2</sub>, and R<sub>3</sub> have small energy differences of less than 1 kJ/mol, as shown by the first row of Tab. 1. Concerning symmetry, rotamers R<sub>1</sub>, and R<sub>3</sub> correspond to a D<sub>2</sub> point group, while R<sub>2</sub> belongs to the C<sub>2</sub> point group. In the table it can be observed that the central biphenyl (Dihedral 2-3) ranges between 36.4°, and 37.2° for the local minima conformers. The torsion angles of the carbazole-phenyl moieties 1-2, and

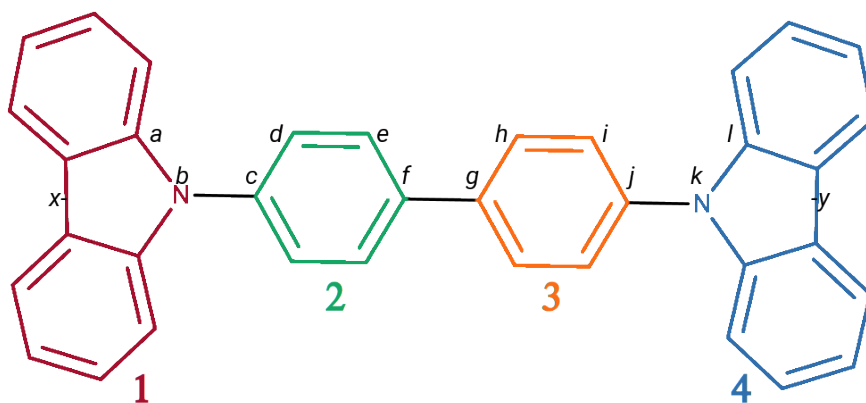


Figure 2: Colour coding of the moieties of CBP: 1 carbazole (red), 2 phenyl (green), 3 phenyl (orange), 4 carbazole (blue). The  $a - l$  tags mark the atoms used to measure torsion angles and bond distances. The CBZ angles are measured between points  $c - b - x$ , and  $j - k - y$ .

3-4, of the tree geometries are similar, with sign variations due to the measurement references. Despite these changes in sign, the overall relative orientation is preserved in the three conformers with the CBZ fragment at  $\pm 50^\circ$  relative to the phenyl group. The CBZ angles,  $c - b - x$ , and  $j - k - y$  in Fig. 2, are  $180^\circ$  in all local minima geometries. These small differences suggest a potential energy surface, PES, with several close-lying local minima.

One example of the close-lying minima stems from the TS structure,  $R_{2-TS}$  in Tab.1. Analysis of the vibrational normal modes revealed a single imaginary frequency at  $i65.99 \text{ cm}^{-1}$  in which the phenyl rings twist out of plane in opposing directions.  $R_{2-TS}$  connects  $R_2$  with its enantiomer,  $R_{2'}$ . The structures are shown in Fig. 4, while the corresponding relative energies, symmetries, and structural parameters are collected in the right section of Tab. 1. Comparison of the  $R_2$  and  $R_{2'}$  geometries shows that the torsion angles are identical except for a flip in signs. In case of  $R_{2-TS}$ , it can be seen that both carbazole moieties are on the same plane, which is also the case for the phenyl rings, though CBZ and Ph are not coplanar. The activation barrier of the isomerization, shown in Fig. 4, is  $7.57 \text{ kJ/mol}$ . Also noteworthy is the change in symmetry along the process:  $R_2$ , and  $R_{2'}$  belong to a  $C_2$  point group, whereas  $R_{2-TS}$  has a  $C_{2h}$  symmetry.

Table 1: Relative energies  $E_{\text{rel}}$ , symmetries, and relevant geometrical parameters of the ground-state CBP rotamers  $R_1$ ,  $R_2$ , and  $R_3$ . Columns  $R_{2\text{-TS}}$  and  $R_2'$  correspond to species related to the isomerization of  $R_2$ , shown in Fig. 4.

	$R_1$	$R_2$	$R_3$	$R_{2\text{-TS}}$	$R_2'$
$E_{\text{rel}}$ [kJ/mol]	0	+0.49	+0.83	+8.06	+0.49
Symmetry	$D_2$	$C_2$	$D_2$	$C_{2h}$	$C_2$
<b>Dih. ang.<sup>a</sup></b>					
1-2	-53.9	-54.1	+54.8	+53.7	+54.1
2-3	+36.4	+36.8	+37.3	0.0	-36.8
3-4	-53.9	+55.0	+54.8	-53.7	-55.0
1-4	-70.5	+37.7	-33.9	0.0	-37.7
<b>Bond dist.<sup>b</sup> [Å]</b>					
$r$ 1-2	1.41	1.41	1.41	1.41	1.41
$r$ 2-3	1.47	1.47	1.47	1.48	1.47
<b>CBZ ang.<sup>c</sup></b>					
1-2	180.0	180.0	180.0	180.0	180.0
3-4	180.0	180.0	180.0	180.0	180.0

<sup>a</sup> Dihedral angle.

<sup>b</sup> Bond distance.

<sup>c</sup> Carbazole angle.

### 3.2.1 CBP ionization energies

Motivated by the use of CBP as hole-transport material, this section focuses on computing ionization energies to study the formation of single-charge radical CBP cations. The calculated IEs are collected in Tab. 2 and the structural parameters of the radical cations are shown in Tab. 3. The relaxed CBP radical cations have overall lower IEs than the non-optimized counterparts, with a difference close to 50 meV. The IEs from the  $GW$  quasi-particle energies are practically the same for both relaxed, and unrelaxed geometries, showing little sensitivity to small structural changes. The IEs from the HOMO QPs are about 0.24 eV larger than the vertical  $\Delta\text{SCF}$  IEs, and 0.28 eV larger than the adiabatic  $\Delta\text{SCF}$  ionization energies. A comparison with the geometries of the neutrally-charged CBP, *cf.* Tab. 1, show that removal of one electron has rather small effects on the conformation of the molecule. Changes in dihedral

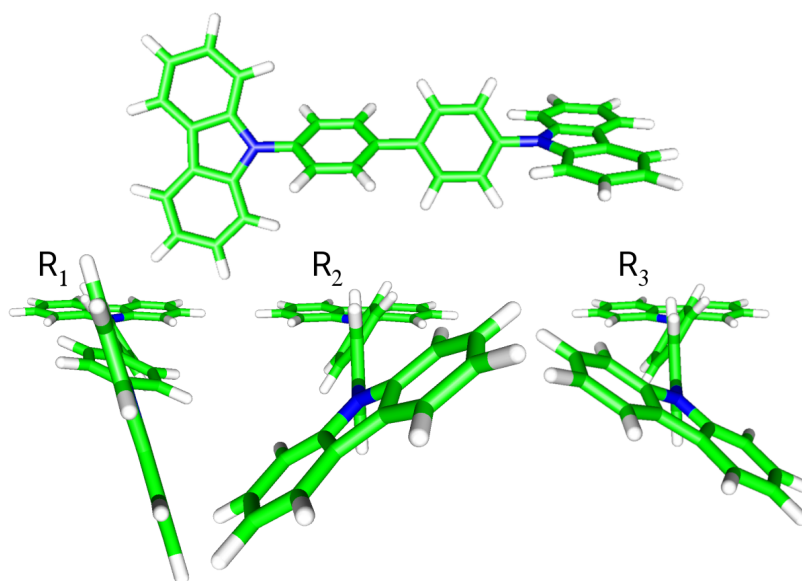


Figure 3: Front view of  $R_1$ , and side view of the CBP rotamers  $R_1$ ,  $R_2$ , and  $R_3$ .

angles 1-2, 2-3, and 3-4 are, for most cases, smaller than  $4^\circ$ . In case of bond distances, the Ph-Ph bond is slightly increased by about  $0.01 \text{ \AA}$ , while the CBZ-Ph bonds remain unchanged. The results suggest that a  $\Delta\text{SCF}$  approach would be better suited to compute the first ionization energy of CBP since it seems more sensitive to slight structural changes caused by the removal of one electron. On the other hand, it should be noted that the  $\Delta\text{SCF}$  approach can suffer from spin contamination which is not the case for  $\text{GW}$ .

The main reference value for these results consists of the experimental IEs measured by ultraviolet photoelectron spectroscopy on a thin film of CBP, which are within the 6.10-6.20 eV range.<sup>[93,94]</sup> We also refer to the adiabatic  $\Delta\text{SCF}$  IE, of 6.65 eV, from a DFT (B3LYP/def2-TZVP) calculation with implicit solvent model PCM, for qualitative comparison.<sup>[95]</sup> The adiabatic  $\Delta\text{SCF}$  results are overestimated about 0.20 eV relative to the DFT qualitative reference, and at least 0.60 eV relative to the experiment. In case of the experimental values, the deviation is significantly larger. The overestimation relative to the experimental IEs could be related to environmental effects, but studying the influence of the environment on the properties of charged molecules is beyond the scope of this thesis.

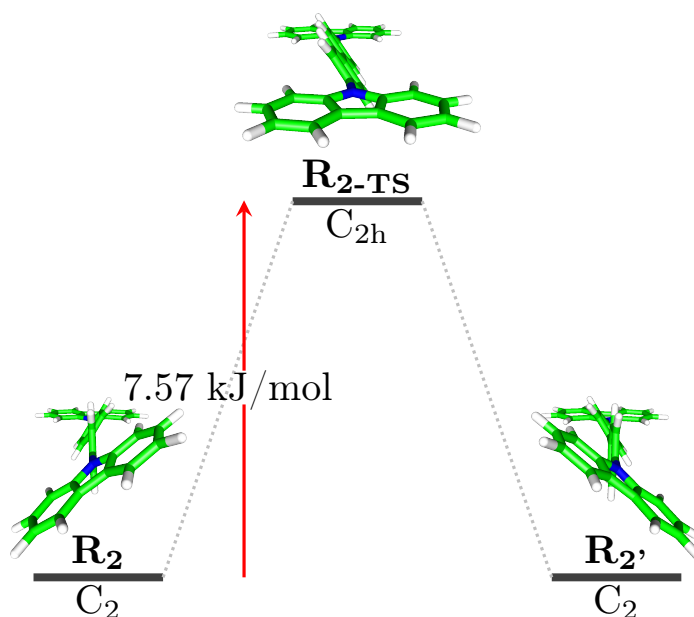


Figure 4: Energy diagram of the rotation of CBP  $R_2$  into its enantiomer  $R_2'$  including symmetry labels. Geometrical parameters are collected in Tab. 1.

Table 2: Ionization energies, IE, in eV, of the CBP rotamers. Experimental reference values from ultraviolet photoelectron spectroscopy are in the 6.10-6.20 eV range.<sup>[93,94]</sup>

	PBE0		GW	
	adiab <sup>a</sup>	vert <sup>b</sup>	w/o <sup>c</sup>	w/ <sup>d</sup>
$R_1^{\bullet+}$	6.85	6.89	7.13	7.13
$R_2^{\bullet+}$	6.86	6.89	7.13	7.13
$R_3^{\bullet+}$	6.86	6.89	7.12	7.12

<sup>a</sup>  $\Delta$ SCF, adiabatic ionization.

<sup>b</sup>  $\Delta$ SCF, vertical ionization.

<sup>c</sup> GW approximation, without geometry relaxation.

<sup>d</sup> GW approximation, with geometry relaxation.

Table 3: Symmetries and geometrical parameters of relaxed-geometry ground-state CBP radical cations.

	$\mathbf{R}_1^{\bullet+}$	$\mathbf{R}_2^{\bullet+}$	$\mathbf{R}_3^{\bullet+}$
<b>Symmetry</b>	D <sub>2</sub>	C <sub>2</sub>	D <sub>2</sub>
<b>Dih. ang.<sup>a</sup></b>			
1-2	-58.4	-60.9	+58.7
2-3	+40.2	+40.9	+40.0
3-4	-58.4	+56.9	+58.7
1-4	-76.1	+36.9	-23.1
<b>Bond dist.<sup>b</sup> [Å]</b>			
<i>r</i> 1-2	1.41	1.41	1.41
<i>r</i> 2-3	1.48	1.48	1.48
<b>CBZ ang.<sup>c</sup></b>			
1-2	180.0	180.0	180.0
3-4	180.0	180.0	180.0

<sup>a</sup> Dihedral angle.<sup>b</sup> Bond distance.<sup>c</sup> Carbazole angle

### 3.3 Singlet vertical excitations

Previous studies have revealed that one of the lower-lying excited states of CBP has a charge-transfer character, dominated by the N-phenylcarbazole and biphenyl moieties.<sup>[33]</sup> As discussed in Sec. 2.2.1, CT states are prone to be inaccurately described by TD-DFT.<sup>[25,26]</sup> Thus, in this section a comparison of singlet absorption spectra computed with the TD-DFT and *GW*-BSE methods is performed. The *GW*-BSE approach is further used to study the absorption spectra of the local minima, as well as the emission of the corresponding relaxed excited-state geometries.

#### 3.3.1 Method comparison: TD-DFT and *GW*-BSE

In this section singlet vertical absorption results from TD-DFT and *GW*-BSE calculations are compared. The density functionals employed are PBE0,<sup>[77,78]</sup> CAM-B3LYP,<sup>[96]</sup> and  $\omega$ B97X.<sup>[97]</sup> The calculations were performed as indicated in the computational details section, *cf.* Sec. 3.1.3, using only the ground-state geometry of the global minimum,  $\mathbf{R}_1$ . Results of the first singlet excitation,  $S_1$ , are collected in Tab. 4. The corresponding absorption spectra are shown in Fig. 5.

Table 4: First vertical singlet transition ( $S_1$ ) of CBP calculated with TD-DFT, employing the functionals PBE0, CAM-B3LYP and  $\omega$ B97X, and the *GW*-BSE approach. Values are given in eV.

	PBE0	CAM-B3LYP	$\omega$ B97X	<i>GW</i> -BSE
$\mathbf{R}_1$	3.69	4.25	4.46	3.99
$\mathbf{R}_2$	3.68	4.25	4.46	3.98
$\mathbf{R}_3$	3.68	4.26	4.46	3.99

The PBE0 absorption, followed by BSE, have the best agreement with experimental values of the first excitation located near 3.70 eV.<sup>[4,91]</sup> Regarding the spectra in Fig. 5, the intensities of the first two states from the PBE0 and BSE calculations are inverted, the latter being in better agreement with the experimental absorption.<sup>[4]</sup> The first root is also much stronger than the second one in the CAM-B3LYP spectrum. In case of  $\omega$ B97X, there first state has about half the intensity of the second one, but the roots are blue-shifted about 0.5 eV relative to the experiment.

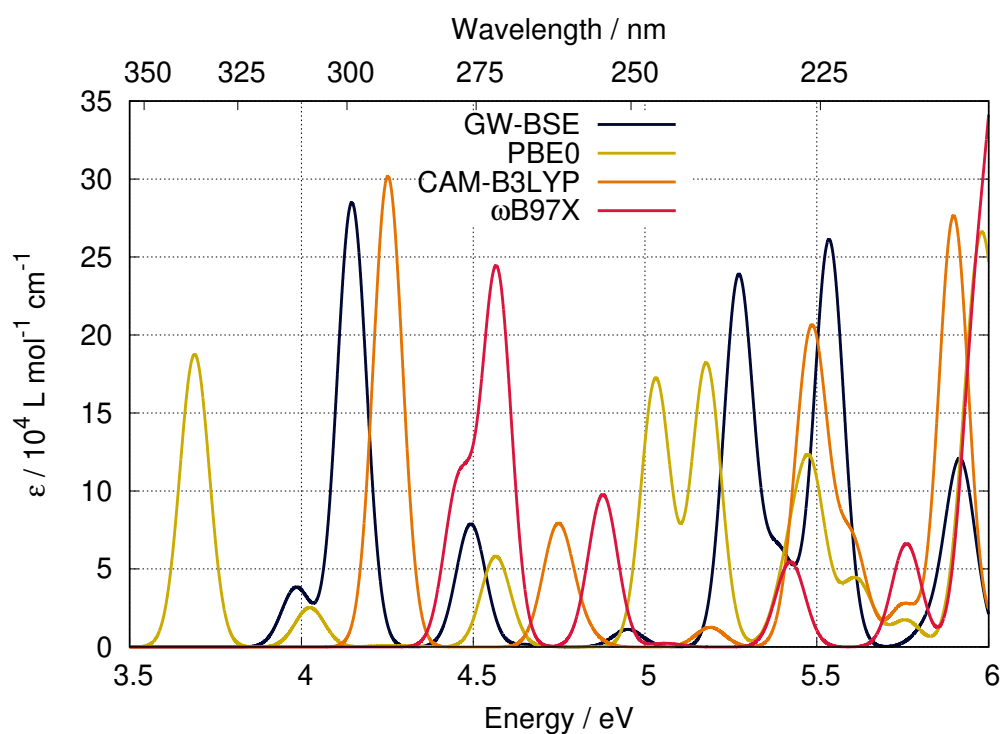


Figure 5: Absorption of CBP rotamer  $R_1$  (FWHM 0.1 eV) calculated with different methods:  $GW$ -BSE in dark blue, PBE0 in yellow, CAM-B3LYP in orange, and  $\omega$ B97X in red.

Some resemblance between the PBE0 and BSE spectra can also be found for the 3rd to 5th bands, between 4.50, and 5.50 eV, despite of the red shift in the PBE0 plot. However, the spectra from the range separated functionals CAM-B3LYP and  $\omega$ B97X are blue-shifted, and quite different from PBE0 and BSE. These discrepancies could be related to differences in their formulation: CAM-B3LYP has 19% exact exchange and 81% Becke 1988 (B88) exchange at short range, while for long range it has 65% exact and 35% B88 exchange.<sup>[96]</sup> On the other hand,  $\omega$ B97X has nearly 16% exact exchange at short range and 100% exact exchange at long range.<sup>[97]</sup> Inclusion of exact exchange using these range-separation schemes allows for a better description of CT-type excitations using TD-DFT, when compared to semi local functionals.<sup>[57]</sup> Aside from the exact exchange portion, the main difference between these functionals arises from the way they define the range of their short- and long-range parts: CAM-B3LYP allows to include both types of exchange over the whole range, while  $\omega$ B97X allows exchange mixing only in the short-range region. In the case of CBP, it seems that for B88 exchange has a positive effect on the overall result.

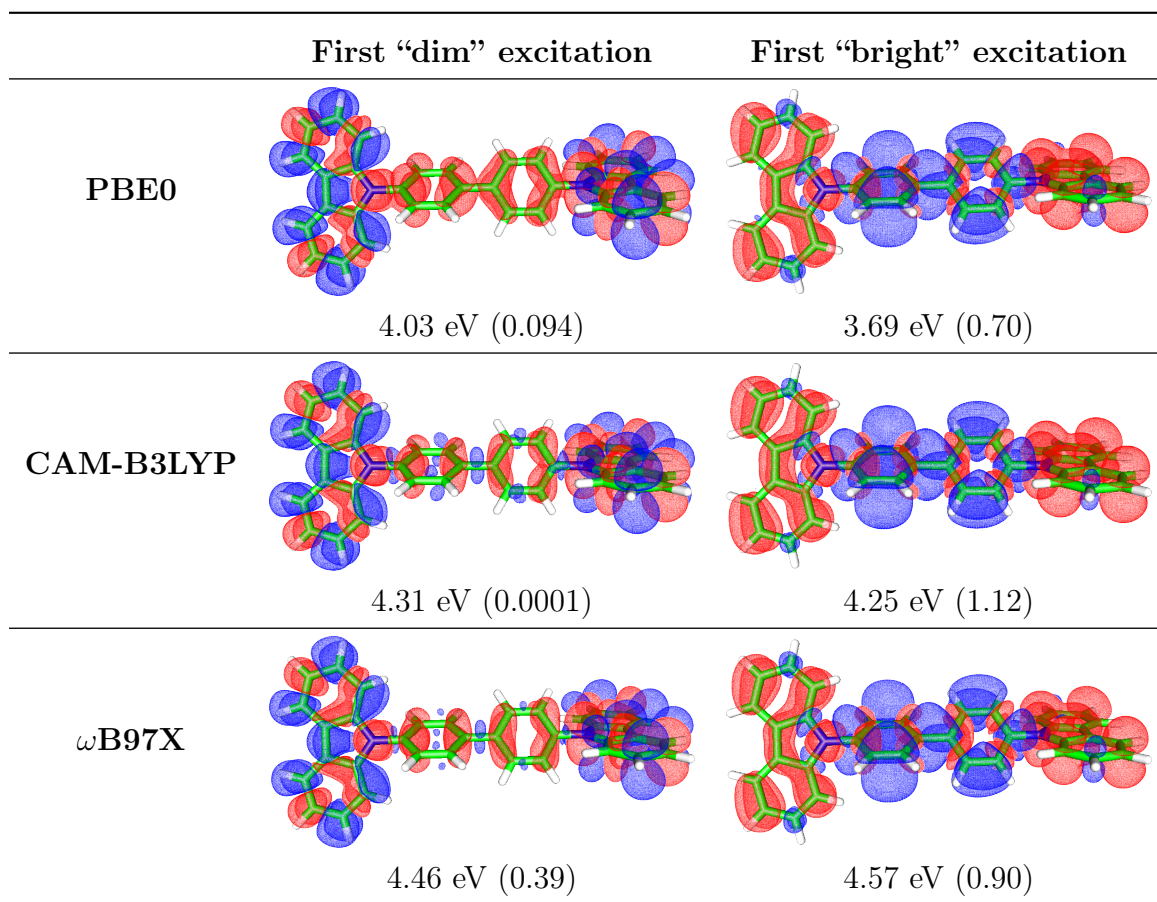


Figure 6: Comparison of transition-density plots (isosurface value of  $2 \times 10^{-4} a_0^{-3}$ ) of the first “dim” (left), and “bright” (right) singlet vertical excitations computed at the TD-DFT level. Corresponding excitation energies and oscillator strengths (in parenthesis) are given for each plot. Density loss is indicated by a red contour, while increase in density is given by the blue contour.

To look further into the nature of the first two absorption bands, the transition densities of states  $S_1$  and  $S_3$  of rotamer  $R_1$  were plotted. The  $S_0 \rightarrow S_2$  transition is symmetry forbidden, *cf.* Tab.5, thus it is not considered. The contour plots are depicted in Fig. 6, where the rows indicate the density functional used in the TD-DFT calculation. The columns use the labels “dim”, to refer to the first non-dark singlet transition which is typically less intense, and “bright”, to refer to the first relatively intense transition. In the rows corresponding to PBE0 and CAM-B3LYP, it can be seen that the “bright” excitations occur at lower energies than the “dim” ones. The difference in case of PBE0 close to 0.3 eV, while for CAM-B3LYP it is smaller than 0.1 eV which can also be noticed in the spectrum in Fig. 5. Both functionals yield the picture of a CT-type state for the “bright” transition, and a more localized character

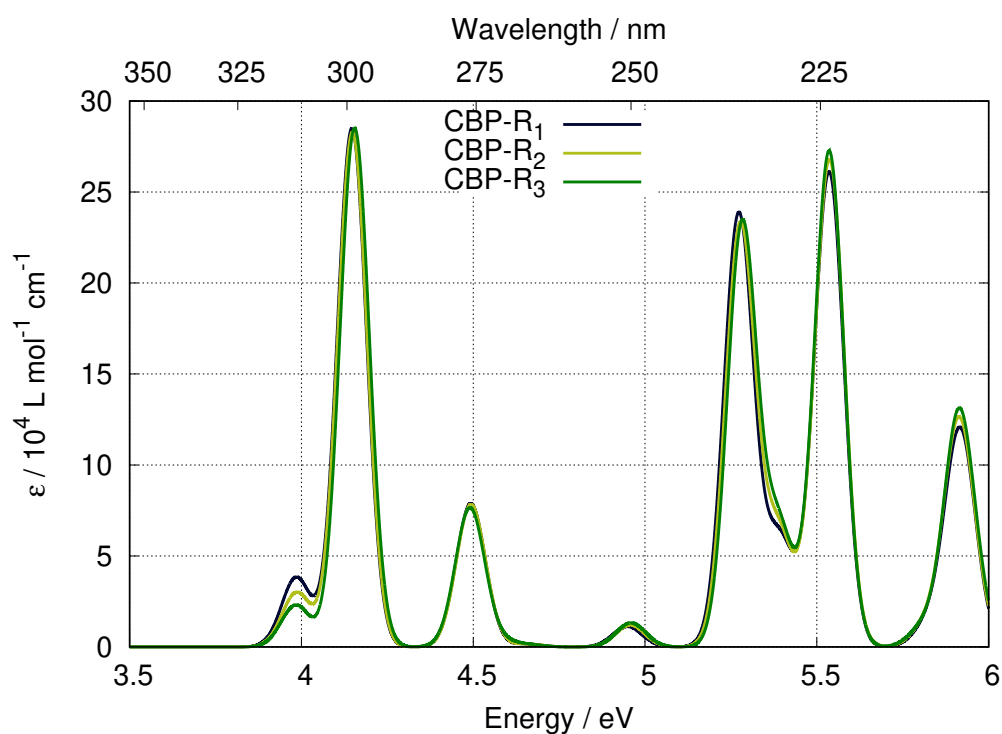


Figure 7: Absorption spectra (FWHM 0.1 eV) of the CBP rotamers calculated with the BSE approach. First excitation energies and oscillator strengths, in parenthesis, are  $R_1$  3.99 eV (0.14),  $R_2$  3.98 eV (0.06), and  $R_3$  3.99 eV (0.09). Second absorption bands occur at  $R_1$  4.15 eV (1.06),  $R_2$  4.15 eV (1.05), and  $R_3$  4.26 eV (1.06).

for the “dim” excitation. In comparison,  $\omega$ B97X yields a “dim” transition at a lower excitation energy, while the “bright” CT-type excitation is located about 0.10 eV higher. Though the ordering is in agreement with the BSE results, the intensities, and energy shifts differ significantly from the references.<sup>[4,91]</sup>

Based on the relative good agreement with the experimental reference, and the general performance of the BSE method regarding CT-excitations,<sup>[29–31]</sup> we limit ourselves to the *GW*-BSE method to calculate singlet excited states of the CBP molecule.

### 3.3.2 Absorption spectra of stable rotamers

Here the *GW*-BSE approach is used to investigate the three stable rotamers  $R_1$ ,  $R_2$ , and  $R_3$ . The vertical absorption energies and spectra are computed according to Sec. 3.1.3. The absorption spectra are displayed in Fig. 7, where almost identical plots can be seen for the three minima geometries. The structural parameters in Tab. 1

show that the largest structural variation occurs for the CBZ-CBZ torsion angle (Dihedral 1-4). In the case of  $R_1$ , the carbazoles are close to being perpendicular ( $-72^\circ$ ), while in  $R_2$  and  $R_3$  they are close to  $35^\circ$ . This suggests that differences in the relative orientation of CBZ-CBZ dihedral yield no significant change in the absorption spectra of local minima geometries. On the other hand, the biphenyl moiety is highly conserved in all minima, with differences of less than  $1^\circ$ . The CBZ-Ph torsion angles are also similar in all rotamers, at about  $\pm 55^\circ$ . Since there are small differences in the Ph-Ph, and CBZ-Ph, dihedrals, the influence of these angles on the absorption cannot be identified from the local minima geometries. The effects of rotational conformation on absorption and emission is further investigated in chapter 4.

### 3.3.3 The charge-transfer state in CBP

To delve into the CT-character in CBP excitations,<sup>[33]</sup> the BSE transition densities were computed for the three ground-state rotamers  $R_1$ ,  $R_2$ , and  $R_3$ . Again, the “dim”, and “bright” labels are used to refer to the first low ( $S_1$  or  $S_2$  states), and high intensity transitions. The corresponding density plots are shown in Fig. 8, where the red contour denotes a reduction of electron density, and the blue contour denotes an increase in electron density due to the electronic transition. In case of the “dim” singlet excitations, all rotamers clearly display a negative character in the biphenyl system, while having a mostly heterogeneous orbital distribution on the carbazole fragments. For this excitation, a CT-state is not completely defined due to the mixed transition orbitals of the CBZ moiety.

Tab. 5 shows the excitation energies, oscillator strengths, and irreducible representations of the first three singlet excitations of the CBP minima  $R_1$ ,  $R_2$ , and  $R_3$ . From the data in the table it can be observed that the rotamers have an  $S_2$  state that is quasi-degenerate to  $S_1$ , but only in case of  $R_2$  a mixing of  $S_1$  and  $S_2$  is allowed by symmetry. Thus, the transition density plots of the “dim” excitations of  $R_1$  and  $R_3$  involve one dark and one low-intensity state, while for  $R_2$  the plot is a linear combination of two low-intensity states. In comparison, the “bright” excitation corresponds only to the  $S_3$  state of each rotamer.

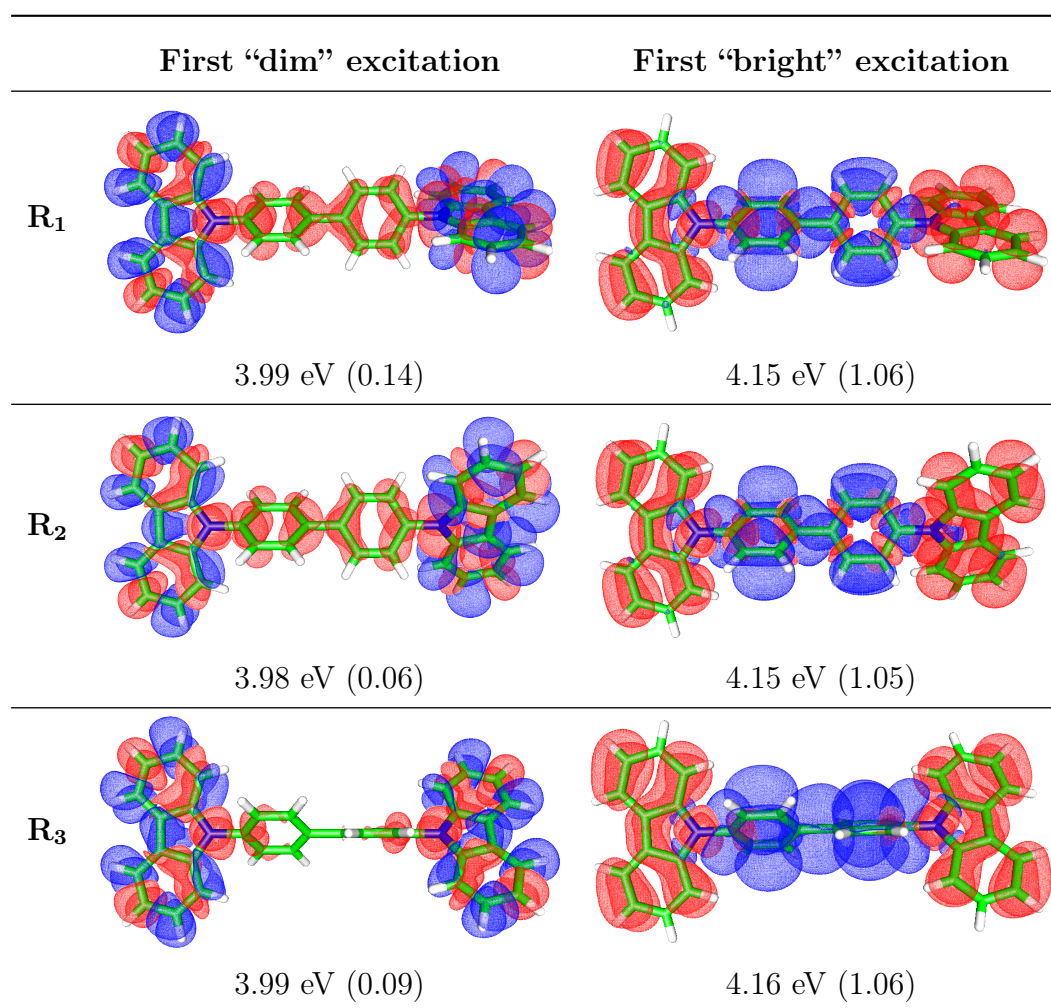


Figure 8: Transition-density plots (isosurface value of  $2 \times 10^{-4} a_0^{-3}$ ) for first “dim” (left column), and first “bright” (right column) singlet vertical absorptions at ground-state geometries, calculated with BSE. Corresponding excitation energies and oscillator strengths (in parenthesis) are given for each plot. Density loss is denoted by a red contour, while increase in density is denoted by a blue contour.

Analysis of the transition density plots of the  $S_3$  “bright” state, displayed on the right column of Fig. 8, shows a well defined charge-transfer character in which the transition occurs from the biphenyl group towards the carbazole moieties. The charge-transfer character is observed in all ground-state rotamers with small differences among them. Confirmation of a charge-transfer type excitation also helps to explain why DFT methods presented larger discrepancies than the  $GW$ -BSE method when compared to the experiments.

Table 5: First three BSE vertical singlet transitions,  $S_1$ ,  $S_2$ , and  $S_3$ , of CBP minima  $R_1$ ,  $R_2$ , and  $R_3$ .

Rotamer		$S_1$	$S_2$	$S_3$
$R_1$	Symmetry	$B_1$	A	$B_1$
	$\omega^a$	3.985	3.989	4.147
	$f^b$	0.142	0.000	1.056
$R_2$	Symmetry	A	A	A
	$\omega^a$	3.984	3.990	4.148
	$f^b$	0.064	0.047	1.049
$R_3$	Symmetry	$B_1$	A	$B_1$
	$\omega^a$	3.985	3.988	4.156
	$f^b$	0.085	0.000	1.057

<sup>a</sup> Excitation energy in eV.<sup>b</sup> Oscillator strength (length representation).

To address the CT-character of the absorption, the state-specific atomic charges of the ground-state geometries were analysed. The atomic charges were computed using a point charge fit to the electrostatic potential. These state-specific quantities require orbital-relaxed density matrices, not yet available for BSE methods. Thus, only the orbital-relaxed density matrices as obtained from TD-DFT calculations with the PBE0 functional are employed. The atomic charges, calculated for  $S_0$  and  $S_1$ , were added for each state to obtain the fragment charge of the carbazoles,  $q_{CBZ}$ , and biphenyl,  $q_{BPh}$ . The difference fragment charges,  $\Delta q$ , between CBP states were computed using  $q_{CBZ}$  and  $q_{BPh}$ .

The results of the fragment and difference atomic charges are displayed in Tab. 6. In the ground state the carbazoles have negative partial charges shown by a  $q_{CBZ}$  of  $-0.50 e$ , while BPh shows a positive character with  $q_{BPh}$  of  $+0.50 e$ . In the  $S_1$  state, the difference in fragment charge is significantly lower, with  $q_{CBZ}$  and  $q_{BPh}$  of  $-0.10$  and  $+0.10 e$  respectively. This means that upon excitation there is a shift of about  $0.40 e$  from the carbazole to the biphenyl fragment, supporting the CT-character of the excitation. It should be noted that the reason for using the  $S_0$ , and  $S_1$  states for the fragment charge analysis is that the charge fit is based on TD-DFT relaxed

Table 6: CBP fragment charges in  $e$  of biphenyl, BPh, and carbazole, CBZ, groups from orbital-relaxed ground,  $S_0$ , and excited-state,  $S_1$ , density matrices of the optimized ground-state geometries.  $\Delta q$  is the difference between fragment charges upon excitation, i.e. absorption.

Geometry		$S_0$	$S_1$	$\Delta q$
$R_1$	$q_{\text{BPh}}$	+0.49	+0.09	-0.40
	$q_{\text{CBZ}}$	-0.49	-0.09	+0.40
$R_2$	$q_{\text{BPh}}$	+0.49	+0.09	-0.40
	$q_{\text{CBZ}}$	-0.49	-0.09	+0.40
$R_3$	$q_{\text{BPh}}$	+0.50	+0.10	-0.41
	$q_{\text{CBZ}}$	-0.50	-0.10	+0.41

density matrices. Thus, by choosing  $S_1$  and not  $S_3$ , the CT-state predicted by TD-DFT calculations is correctly selected.

### 3.4 Relaxed excited-state geometries and fluorescence

The geometry of rotamers  $R_1$ ,  $R_2$ , and  $R_3$  were relaxed in their lowest allowed singlet excitation, *cf.* 3.1.3. The resulting excited-state structures were labeled  $E_1$ ,  $E_2$ , and  $E_3$ , following the convention established for the ground-state geometries. For example,  $E_1$  was obtained after geometry optimization in the excited state of  $R_1$ . The corresponding point groups, relative energies, adiabatic energy differences, AED, vertical emission energies, and structural parameters are collected in Tab. 7.

The table shows an energy difference between the excited state rotamers of less than 2 kJ/mol. In this case however,  $E_3$  is the more stable excited-state rotamer, having also the lowest AED of 3.40 eV. The AED of the other two rotamers are about 0.03 eV higher than  $E_3$ . All vertical transition energies are within 0.01 eV. In the ground state the dihedral angle of the biphenyl group is approximately  $36^\circ$ , but becomes significantly more flat, at less than  $10^\circ$ , upon excitation to the  $S_1$  state; *cf.* Tab. 1. Changing to an almost-in-plane orientation promotes conjugation of the pi-system, which could improve excited-state stabilization by allowing delocalization over more atoms. This is also supported by a contraction in the biphenyl bond after excitation,

which decreases from 1.47 to 1.43 Å. Upon excitation, the CBZ-Ph dihedral angles change about  $\pm 1^\circ$  relative to the ground-state geometries, while the corresponding bond distance remains practically unchanged, at 1.41 Å.

Table 7: Geometric and energetic data corresponding to  $E_1$ ,  $E_2$ , and  $E_3$ . Relative energies,  $E_{\text{rel}}$ , in kJ/mol, of singlet excited-state optimized geometries relative to  $E_3$ . Adiabatic energy differences, AED, and vertical emission energies,  $\omega$ , in eV. Oscillator strengths in parenthesis. Symmetries of excitations are  $B_1$ , A, and B for  $E_1$ ,  $E_2$ , and  $E_3$ , respectively.

	$E_1$	$E_2$	$E_3$
<b>Symmetry</b>	$D_2$	$C_2$	$D_2$
<b>Singlet</b>			
$E_{\text{rel}}$	+0.04	+1.87	0
AED	3.43	3.42	3.40
$\omega$	3.19	3.18	3.19
	(0.79)	(0.76)	(0.75)
<b>Dih. ang.<sup>a</sup></b>			
1-2	-55.5	-55.6	+55.9
2-3	+5.2	+6.8	+8.0
3-4	-55.5	+56.2	+55.9
1-4	+74.2	+7.7	-59.9
<b>Bond dist.<sup>b</sup> [Å]</b>			
$r$ 1-2	1.41	1.41	1.41
$r$ 2-3	1.43	1.43	1.43
<b>CBZ ang.<sup>c</sup></b>			
1-2	180.0	180.0	180.0
3-4	180.0	180.0	180.0

<sup>a</sup> Dihedral angles.

<sup>b</sup> Bond distances.

<sup>c</sup> Carbazole angle.

The relaxed geometries are included in Fig. 9, where the values for vertical emission energies from TD-DFT (PBE0), and the BSE method are also collected. As observed in the ground-state case, there are small variations in emission energies and oscillator

strengths, within the same method, due to very similar structures. The BSE emission energies are in closer agreement with experimental measurements, which show a peak at about 3.45 eV.<sup>[91]</sup> TD-DFT emission is underestimated by about 0.40 eV with respect to BSE. A comparison of the emission and absorption energies, *cf.* Tab. 5, reveals that emission is red-shifted by approximately 0.40 eV with respect to lowest absorption energy. The conservation of CBZ-Ph structural parameters in the relaxed ground- and excited-state geometries suggests that the red shift of the emission energy is related to the contraction of the Ph-Ph bond and the in-plane torsion of the phenyl groups.

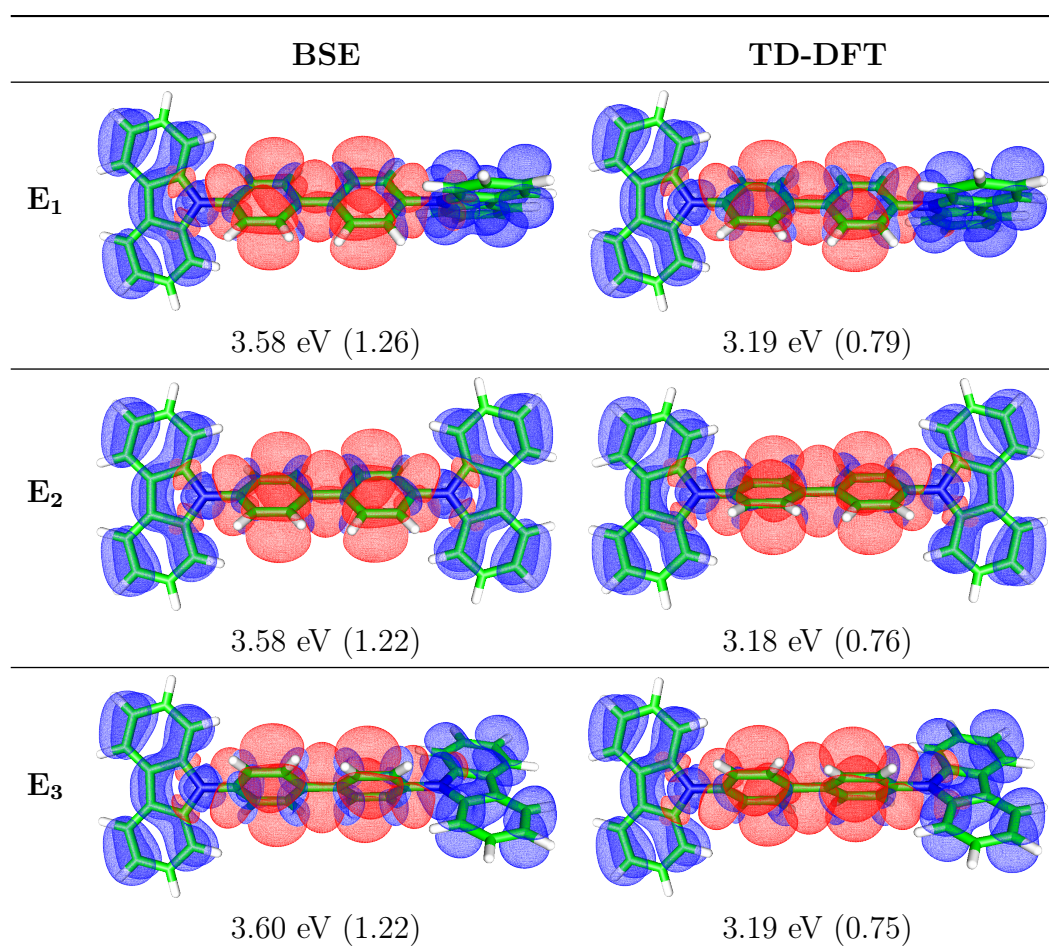


Figure 9: Transition-density plots (isosurface value of  $2 \times 10^{-4} a_0^{-3}$ ) of CBP rotamers  $E_1$ ,  $E_2$ , and  $E_3$  for fluorescence, i.e. de-excitation, at the excited-state geometry *cf.* Tab. 7, for the first singlet state, calculated with BSE, and TD-DFT (PBE0). Density loss is denoted by a red contour, while increase in density is denoted by a blue contour. Oscillator strengths shown in parenthesis.

Table 8: CBP fragment charges in  $e$  of biphenyl (BPh) and carbazole (CBZ) groups from orbital-relaxed ground,  $S_0$ , and excited-state,  $S_1$ , density matrices of the relaxed excited-state geometries.  $\Delta q'$  is the difference between fragment charges upon de-excitation, i.e. emission.

Geometry		$S_1$	$S_0$	$\Delta q'$
$E_1$	$q_{\text{BPh}}$	+0.12	+0.50	+0.38
	$q_{\text{CBZ}}$	-0.12	-0.50	-0.38
$E_2$	$q_{\text{BPh}}$	+0.11	+0.50	+0.39
	$q_{\text{CBZ}}$	-0.11	-0.50	-0.39
$E_3$	$q_{\text{BPh}}$	+0.10	+0.50	+0.40
	$q_{\text{CBZ}}$	-0.10	-0.50	-0.40

### 3.4.1 Emission and charge-transfer states

Vertical transition density plots of  $E_1$ ,  $E_2$ , and  $E_3$ , as well as emission energies and oscillator strengths computed at the  $GW$ -BSE and TD-DFT levels of theory are displayed in Fig. 9. Both sets of plots show that emission also has a charge-transfer character, where the transition occurs now from the biphenyl region towards the carbazoles. The qualitative similarity between these plots is a good indicator of sufficiently accurate excited-state geometries from TD-DFT optimizations, and that there seems to be no problem for the description of the CT emission, in contrast with the vertical absorption.

In analogy to the absorption, *cf.* Sec. 3.3.3, the CT-character of emission was investigated using state-specific atomic charges. In this case, the orbital-relaxed density matrices were obtained from TD-DFT calculations of the relaxed excited-state geometries  $E_1$ ,  $E_2$ , and  $E_3$ . The results are collected in Tab. 8. The difference in atomic charges,  $\Delta q'$ , also point to a significant CT character of the emission, in which 0.4 electrons are moved from the biphenyl towards the carbazole moieties. This is consistent with the total change in biphenyl and carbazole charges upon absorption, shown in Tab. 6, where nearly 0.4  $e$  are displaced from the carbazole to the biphenyl fragments when CBP is excited.

Optimization of different torsional CBP conformers led to three close-lying local minima geometries which have very similar dihedral angles for the carbazole and

phenyl moieties. This suggests that minima rotamers share a highly-conserved set of geometrical parameters. One important consequence is that electronic properties, like ionization energies or vertical absorption, have almost no variations among local minima. Investigation of vertical singlet transitions due to absorption showed that the lowest CT-type excitation of CBP is not described correctly by TD-DFT, even when using the range-separated functionals CAM-B3LYP or  $\omega$ B97X. In particular, PBE0 and CAM-B3LYP yield an incorrect state ordering, while  $\omega$ B97X introduces a substantial blue shift. These problems are not present in the *GW*-BSE approach, making it a suitable method to study singlet excitations in CBP. Interestingly, problems to describe the CT-state seem to be missing in the emission from the relaxed excited-state geometries, where the TD-DFT and *GW*-BSE descriptions match. A study based only on gas-phase optimized CBP geometries cannot fully assess the connection between conformation and electronic properties of CBP. Hence, an ensemble-like approach is proposed in the next chapter, based on a CBP molecule with free-rotating carbazole and phenyl groups.

## 4 Effects of rotational conformation of CBP on excited-state properties

In the case of CBP, a broad variety of rotational conformers can be attributed to two structural motifs: the torsion angles between the phenyl rings, Ph<sub>1</sub> and Ph<sub>2</sub>, in the biphenyl moiety, and the orientation of the carbazole moieties relative to their phenyl rings. These are depicted in Fig. 10.

To have a better understanding of the effects of torsional conformation on the electronic properties of CBP, this chapter <sup>1</sup> focuses on the changes in absorption and emission spectra in the free-rotating, non-interacting CBP molecule. Although confinement within the bulk would only allow some conformations, the picture offered by the free-rotating CBP serves as a first step to understand the influence of purely geometrical changes.

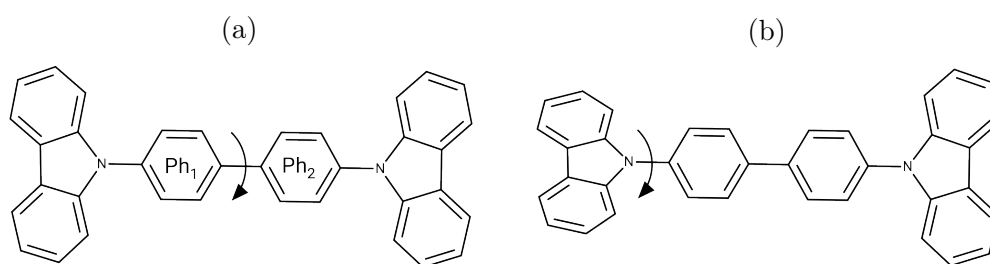


Figure 10: Principal torsion angles of CBP. Rotation is indicated for the (a) phenyl-phenyl, and (b) carbazole-phenyl dihedrals.

<sup>1</sup>Partially adapted from R. Cortés-Mejía, S. Höfener and W. Klopper, *Mol. Phys.* **2021**, *119*, e1876936.

## 4.1 Computational details

### 4.1.1 Rotation scan of CBP and electronic structure calculations

The influence of torsional conformation on the absorption spectrum of CBP was investigated using a sample of conformers that could give a significant overview of the conformational space. Using as reference the geometry of the ground-state global minimum,  $R_1$ , *cf.* Sec. 3.2, the sample was generated by incrementally rotating the crabazole and phenyl groups in  $15^\circ$  steps from 0 to  $345^\circ$ . The rotated angles are depicted in Fig. 10. Given the structure of CBP, there are several cases where rotations lead to identical geometries due to symmetry. Thus, the nuclear repulsion energies of all rotational conformers were calculated and used as criterion to select unique geometries, e.g. structures with repeating values of nuclear repulsion energies were discarded. From a total of 13.8 k structures from the scan, 1596 were identified as unique. These structures were used for the electronic structure calculations detailed below, all of which were carried out with the TURBOMOLE program package.<sup>[73,74]</sup>

The unique rotamers were subjected to single point calculations at the DFT level with the PBE0 functional,<sup>[77,78]</sup> and a medium multiple-grid of size 3 (m3 grid in TURBOMOLE).<sup>[75]</sup> The def2-SVPD basis,<sup>[98]</sup> and the RI approximation<sup>[80,81]</sup> with the def2-SVPD auxiliary basis<sup>[82]</sup> were used. Convergence criteria of the single-point calculations were set to  $10^{-7}$   $E_h$  for the energy, and  $10^{-7}$  for the electron density.

Singlet vertical excitation energies of all unique rotamers were computed employing the *GW* approximation and the Bethe-Salpeter equation as implemented in TURBOMOLE.<sup>[61,90]</sup> For these, energies of the HOMO and LUMO were corrected using the RI-CD-ev*GW* variant.<sup>[84]</sup> Absorption energies were computed for 25 excitations to approximate experimental spectral windows of 200-500 nm.<sup>[4,91]</sup> Response equations were converged to an Euclidean residual norm of less than  $10^{-5}$ .

To investigate the influence of rotation on emission, a different set of rotamers was employed, which was based on singlet excited-state geometries. The the lowest excited-state geometry  $E_3$ , *cf.* Sec. 3.4, was used as starting point for the rotation scan described above. All reference- and excited-state calculations of the unique rotamers generated from  $E_3$  were carried out as detailed above.

### 4.1.2 Boltzmann averaging to simulate temperature-dependent spectra

The average CBP absorption spectrum was obtained by weighting the individual oscillator strengths, taking into account the number of structures with equal nuclear repulsion energies (structure degeneracies) and a temperature-dependent Boltzmann factor:

$$\tilde{f}_{r,i}(T) = Q^{-1} \cdot f_{r,i} \cdot g_r \cdot \exp\left(-\frac{E_r - E_{\text{ref}}}{kT}\right), \quad (81)$$

where  $E_r$  is the ground-state DFT energy of rotamer  $r$  and  $E_{\text{ref}}$  is the ground-state DFT energy of the global minimum rotamer  $R_1$ , both in  $E_{\text{h}}$ .  $k$  is the Boltzmann constant,  $k = 3.167 \cdot 10^{-6} E_{\text{ref}}/K$ , the temperature  $T$ , in Kelvin,  $f_{r,i}$  is the oscillator strength of the  $i$ -th electronic state of rotamer  $r$ ,  $g_r$  denotes the degeneracy of the  $r$ -th rotamer,  $\tilde{f}_{r,i}$  is the weighted oscillator strength, and  $Q$  is the partition sum:

$$Q = \sum_r g_r \cdot \exp\left(-\frac{E_r - E_{\text{ref}}}{kT}\right). \quad (82)$$

The weighted oscillator strengths  $\tilde{f}_{r,i}$  are used to simulate the Gaussian spectra  $\varepsilon_r^i(\nu)$  of each excitation  $i$  of every  $r$  rotamer,

$$\varepsilon_r^i(\nu, T) \propto \tilde{f}_{r,i}(T) \cdot \exp(-(\nu - \nu_i)^2), \quad (83)$$

which are combined to a spectrum for one rotamer  $r$ :

$$\varepsilon_r(\nu, T) = \sum_i \varepsilon_r^i(\nu, T). \quad (84)$$

The averaged spectrum  $\langle \varepsilon(\nu, T) \rangle$  for a given temperature  $T$  is finally constructed from all rotamers:

$$\langle \varepsilon(\nu, T) \rangle = \sum_r \varepsilon_r(\nu, T). \quad (85)$$

## 4.2 Fragment charge analysis

As discussed in Sec. 3.3.3, the fragment charge distribution and its changes upon absorption and emission can be employed to assess the charge-transfer character of an excitation. Thus, the changes in fragment charges due to torsion of the dihedral angles of CBP are investigated in the following. One thing to consider is that for

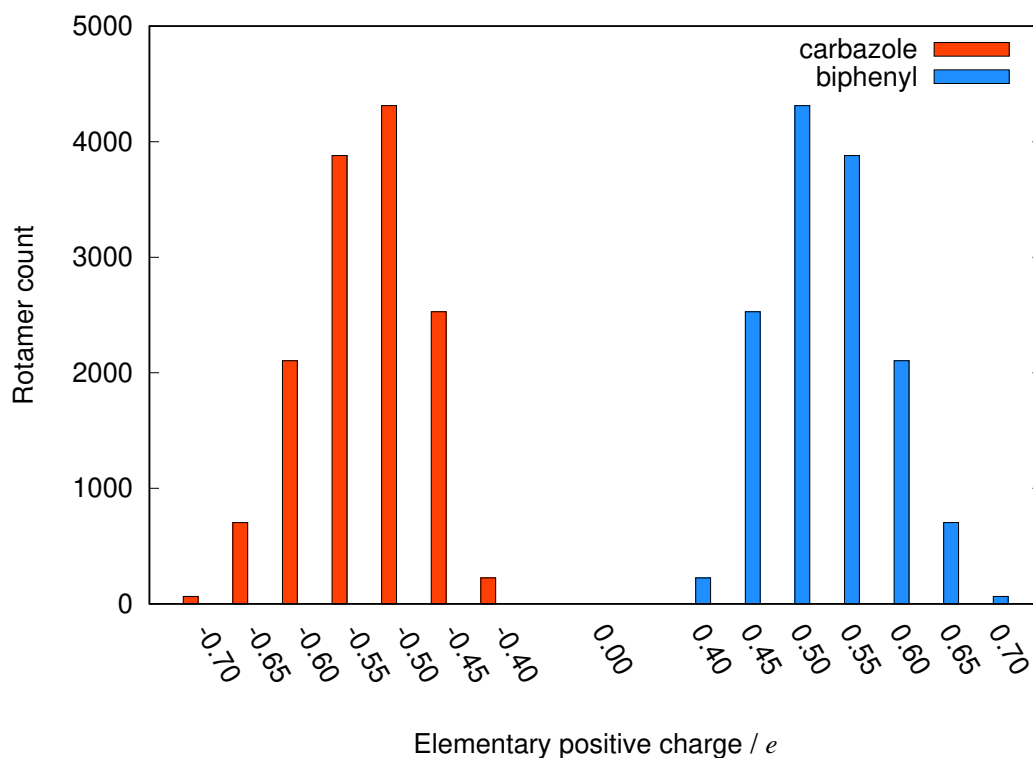


Figure 11: Carbazole (red), and biphenyl (blue) subsystem charge histogram. Charges are grouped in  $0.05 e$  intervals. Box height indicates rotamer count for the corresponding charge interval.

this section, only ground-state fragment charges of the  $S_0$  state are computed for the biphenyl (BPh), and carbazole (CBZ) fragments of the rotamers in the collection.

Fig. 11 shows a histogram of fragment charges. The horizontal axis corresponds to charge intervals with a step size of  $0.05 e$ , electrons, in the interval from  $-0.70$  to  $+0.70 e$ . The vertical axis indicates the total rotamer count, taking into account the degenerate structures. Carbazole and phenyl fragment charges are summed from the corresponding ground-state atomic charges.

The plot reveals that, throughout the 13 824 CBP rotamers, the BPh moiety always maintains a partial positive charge, while the CBZ remains negative. The interval with the highest rotamer count ranges from  $\pm 0.55$  to  $\pm 0.50 e$ , in agreement with the fragment charges of the ground-state reference structure where the carbazole and biphenyl charges are  $-0.50 e$  and  $+0.50 e$ , respectively; *cf.* Tab. 6.

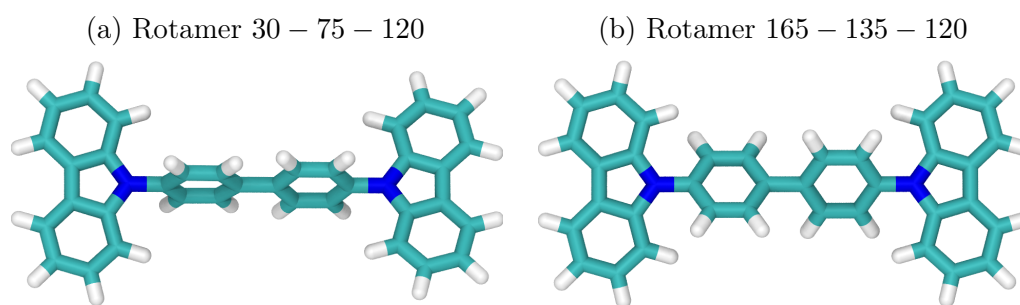


Figure 12: Geometries of rotamers with largest and smallest fragment charges. (a) CBZ and BPh charges of  $-0.66 e$  and  $+0.66 e$ , respectively. (b) CBZ and BPh charges of  $-0.37 e$  and  $+0.37 e$ .

Fig. 12 shows a comparison of the geometries of the rotamers with the largest fragment charge differences. The highest fragment charge separation has a value of  $-0.66 e$  for the CBZ and  $+0.66 e$  for the BPh, which correspond to rotamer 30–75–120 (left). The phenyl–carbazole and phenyl–phenyl torsion angles are  $96^\circ$  and  $8.6^\circ$ , respectively. In contrast, rotamer 165–135–120 (right) shows the lowest fragment charges of  $-0.37 e$  and  $+0.37 e$  for the carbazole and biphenyl fragments. Here, the phenyl–carbazole and phenyl–phenyl dihedral angles are  $38^\circ$  and  $66^\circ$ , respectively. This suggests that fragment charge is predominantly dependent on the phenyl-carbazole torsion angles, and that the charge separation increases as the planes of these groups become more orthogonal.

Through torsion of the dihedral angles of the carbazole and biphenyl moieties a change in charge separation up to  $\pm 0.2 e$  can be expected. The overall positive or negative character of the moiety is maintained.

### 4.3 Temperature dependence of absorption spectra

The vertical transition energies obtained for the collection of rotamers were used to model average spectra at temperatures of 0, 100, 200, 300, 400, and 500 K. The corresponding weighted spectra are shown in Fig. 13, where the vertical axis corresponds to molar absorption coefficients,  $\epsilon$ , in units of  $\text{L mol}^{-1} \text{mol}^{-1}$ . For reference purposes, Fig. 13 also includes the absorption lines of the lowest energy structure, labelled  $R_1$ .

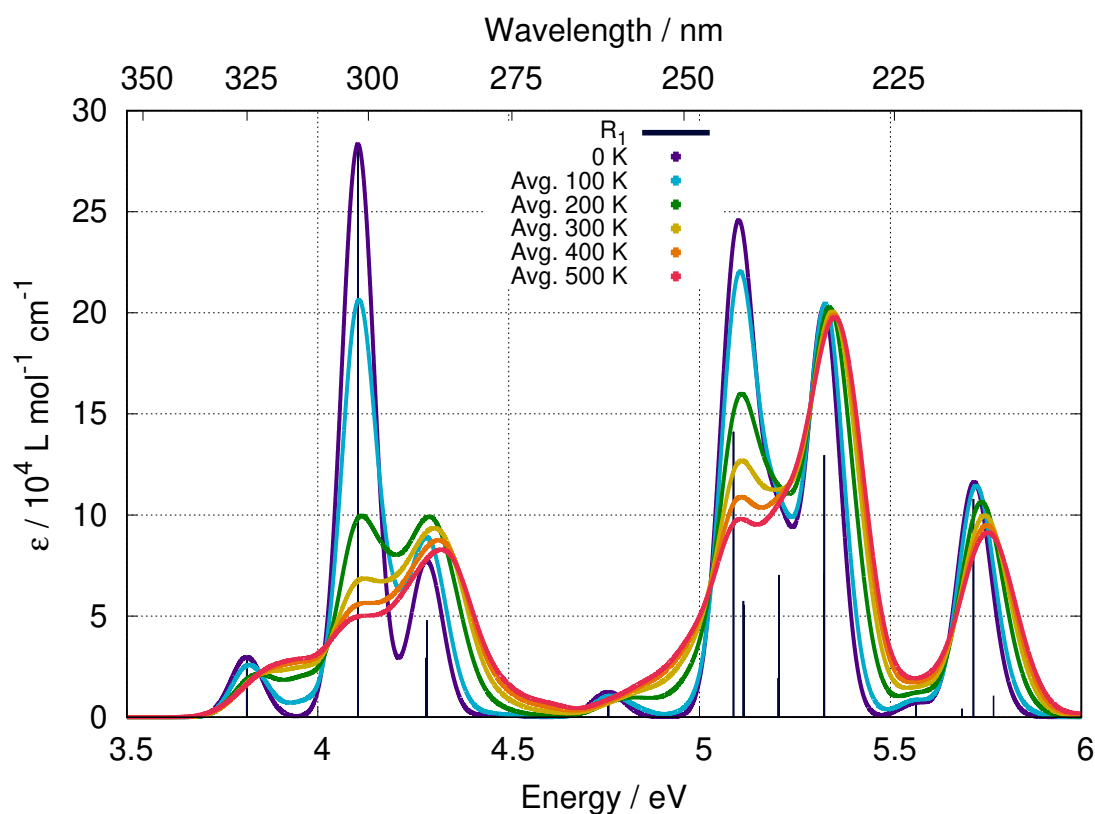


Figure 13: Boltzmann-average weighted CBP absorption spectra (FWHM 0.1 eV) at temperatures 0, 100, 200, 300, 400, and 500 K. The black vertical lines correspond to the absorption lines of the lowest energy rotamer  $R_1$ . The first excitation occurs at 3.81 eV.

A significant change in the absorption spectra can be observed as the temperature used for the Boltzmann weighting factor, given by Eq. (81), is raised. This is caused by the increased contribution of higher-energy rotamers. For example, at 0K only the lowest-energy rotamer will have a non-zero weight, thus the spectrum will match the reference absorption lines exactly. At 100 K, the weight of most rotamers is close to zero, so the dominant contribution to the spectrum comes from the global minimum geometry.

Absorption spectra beyond temperatures of 200 K change considerably in the energy window between 3.70 eV and 5.20 eV, with an overall slight blue shift. With increasing temperature, the first excitation, at 3.81 eV, becomes smeared together with the signal at 4.10 eV. The latter is substantially attenuated with increasing temperature. The 5.1 eV excitation shows a similar behaviour, where higher temperatures result in a peak widening. In contrast, signals located close to 4.3 eV, 5.3 eV, and 5.7 eV undergo

Table 9: Temperature-weighted statistical analysis of the 4.1, and 5.7 eV peaks in the Boltzmann-weighted absorption spectra of CBP, *cf.* Fig. 13.

<b>T / K</b>	<b>Near 4.1 eV peak</b>				<b>Near 5.7 eV peak</b>			
	$\nu^a$		$f^b$		$\nu^a$		$f^b$	
	$\mu^c$	$\text{Var}^d$	$\mu^c$	$\text{Var}^d$	$\mu^c$	$\text{Var}^d$	$\mu^c$	$\text{Var}^d$
<b>0</b>	4.11	0	1.05	0	5.72	0	0.40	0
<b>100</b>	4.13	<0.01	1.00	0.01	5.72	<0.01	0.42	<0.01
<b>200</b>	4.18	0.01	0.86	0.07	5.74	<0.01	0.46	0.01
<b>300</b>	4.20	0.02	0.76	0.11	5.75	<0.01	0.47	0.01
<b>400</b>	4.22	0.02	0.71	0.13	5.75	<0.01	0.48	0.02
<b>500</b>	4.22	0.02	0.67	0.14	5.75	<0.01	0.49	0.02

<sup>a</sup> Excitation energy in eV.<sup>b</sup> Oscillator strength, length gauge.<sup>c</sup> Mean value.<sup>d</sup> Variance.

significantly smaller changes due to raising temperature. In the following section, selected bands are analysed to assess the changes in intensities and energy shifts due to increase of temperature in the Boltzmann factor.

#### 4.3.1 Statistical analysis: ground-state rotamers

The differences in energy shifts and intensities indicate that not all excitations are equally sensitive to changes in the torsion angles of CBP. To investigate these variations, the distribution of energies and oscillator strengths of the signals at 4.10 eV and 5.70 eV were analysed. The temperature-weighted data distribution of these peaks is shown in Tab. 9. The mean values of excitation energy and oscillator strength are shown for each temperature, together with the corresponding variance.

Tab. 9 shows that, in case of the 4.10 eV signal, there is a significant increase in the variance of the oscillator with temperature. This translates into an overall decrease of the mean oscillator strength, with a factor near 3.7, for a temperature increase from 100 K to 500 K. With rising temperature the number of contributing geometries also grows, however, the band becomes significantly less intense. This suggests that there are few torsional conformations associated with strong transition moments, while the

vast majority of rotamers yield weaker transitions, pointing to a strong dependence of the CT band on the conformation of CBP. Hence, an increase in the temperature of the ensemble picture will result in a drastic intensity decrease of the band. In contrast, the 5.7 eV band shows comparatively small changes in excitation energies and oscillator strengths throughout the temperature range, pointing to an excitation with almost no dependence on the torsional conformation.

Changes to the 4.1 eV signal can be visualized in the distribution histograms shown in Fig. 14 and Fig. 15. The graphs contained in Fig. 14 correspond to a "temperature-independent" case, meaning that all 13.8 k rotamers have the same weight and the count of molecules is shown in the vertical axis. The top (blue) plot shows the distribution of excitation energies, while the plot on the bottom (red) shows the oscillator strengths, in length gauge. The distribution of excitation energies shows that a good amount of rotamers are expected to have a blue shift for their third, "bright", root with respect to the minimum, which does not show in the mean data between 4.11–4.22 eV, *cf.* Tab. 9. Similarly, the red histogram shows it should be a rather weak excitation since the majority of rotamers are below the mean at any given temperature, which is in the 0.67–1.05 interval.

The picture changes in a temperature dependent scenario, where the 13.8 k molecules have been weighted for the different temperatures with the Boltzmann distribution, shown in Fig. 15. In this figure, the vertical axes display the weight of the molecules in the distributions. The top plot corresponds to temperature weighted excitation energies, while the bottom plot shows oscillator strengths. With increasing temperature, rotamers with blue-shifted excitation energies become more relevant, but their contribution is not significant enough to induce a big shift. Thus, the excitation energy has a 4.22 eV mean value at 500 K. In case of the bottom pane of Fig. 15, not only the oscillator strengths become noticeably spread with increasing temperature, but the rotamers with higher weights are also those that have a relatively weak excitation. This results in the 4.10 eV vanishing peak.

A similar set of histograms for the 5.70 eV signal is presented in Fig. 16 and Fig. 17. The distributions in Fig. 16 correspond to the temperature independent case. Here, the excitation energies are relatively well grouped, with most rotamers between 5.70 and 5.90 eV. For oscillator strengths, the values with most rotamer counts are around 0.40.

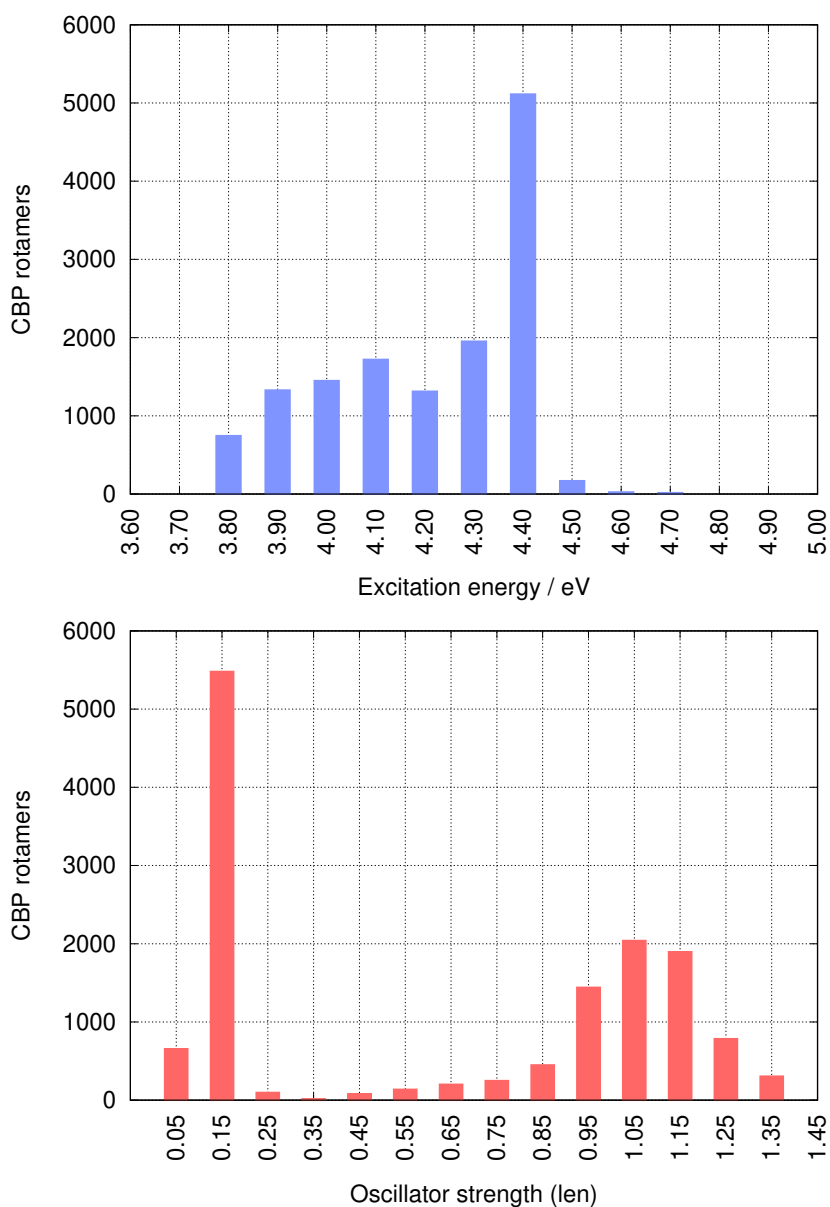


Figure 14: Temperature independent distribution histograms of excitation energies (top) and oscillator strengths (bottom) of the third root, near 4.10 eV, of the 13.8 k molecules generated from CBP rotation in  $15^\circ$  steps. Vertical axes correspond to CBP molecule count. All rotamers have the same weight.

The Boltzmann-weighted picture in Fig. 17 shows a comparatively tighter distribution of both excitation energies and oscillator strengths. This results in the 5.7 eV signal, which is highly conserved through the temperature range.

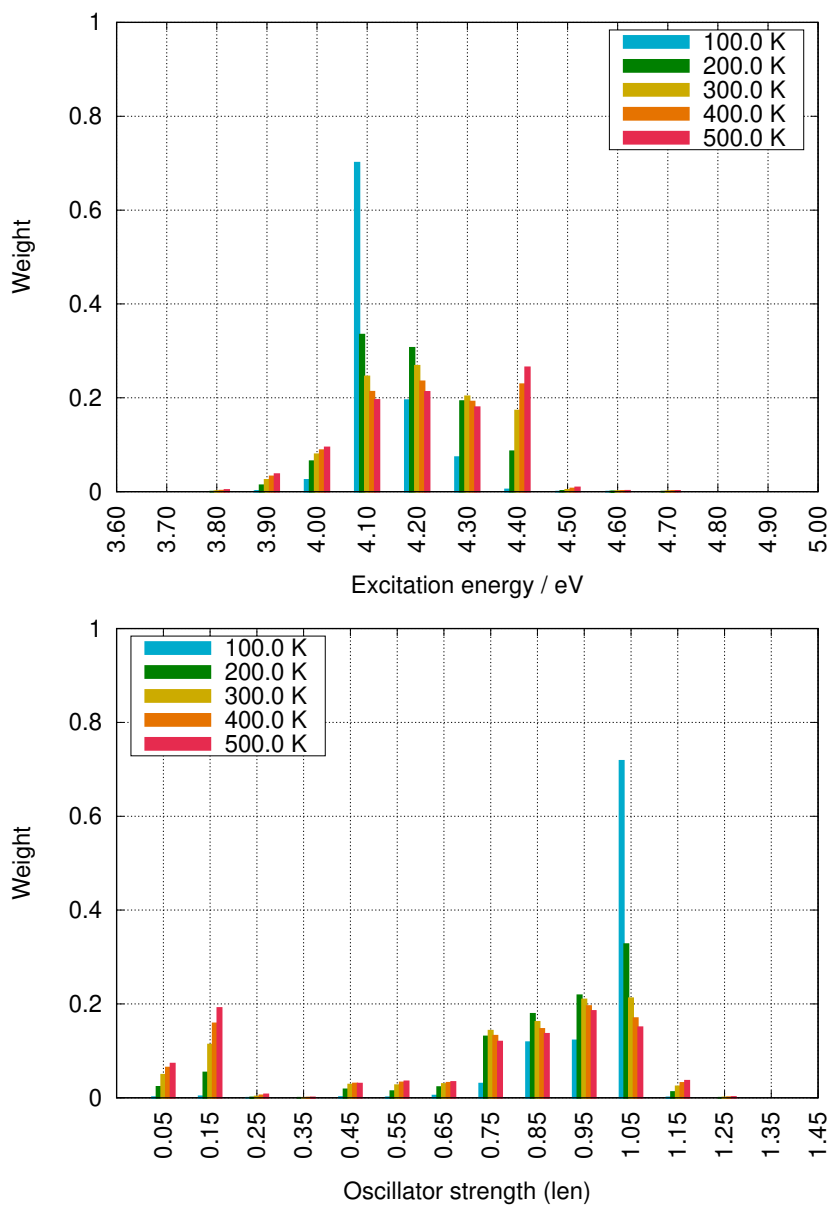


Figure 15: Distribution of excitation energies (top) and oscillator strengths (bottom) of the third root, near 4.10 eV, of the 13.8 k molecules generated from CBP rotation, weighted for different temperatures using the Boltzmann distribution based on the ground-state energy differences.

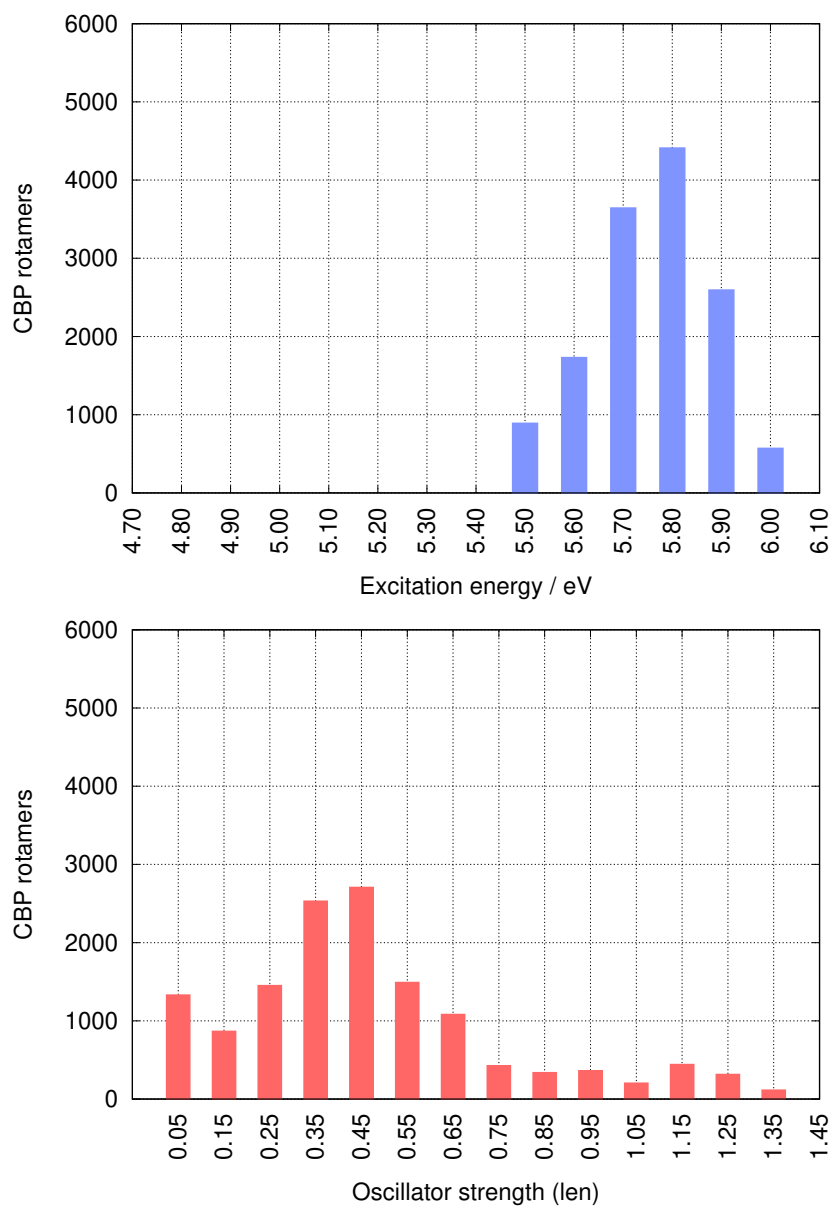


Figure 16: Temperature-independent distribution of excitation energies (top) and oscillator strengths (bottom) of the band at about 5.70 eV of the 13.8 k molecules generated from CBP rotation.

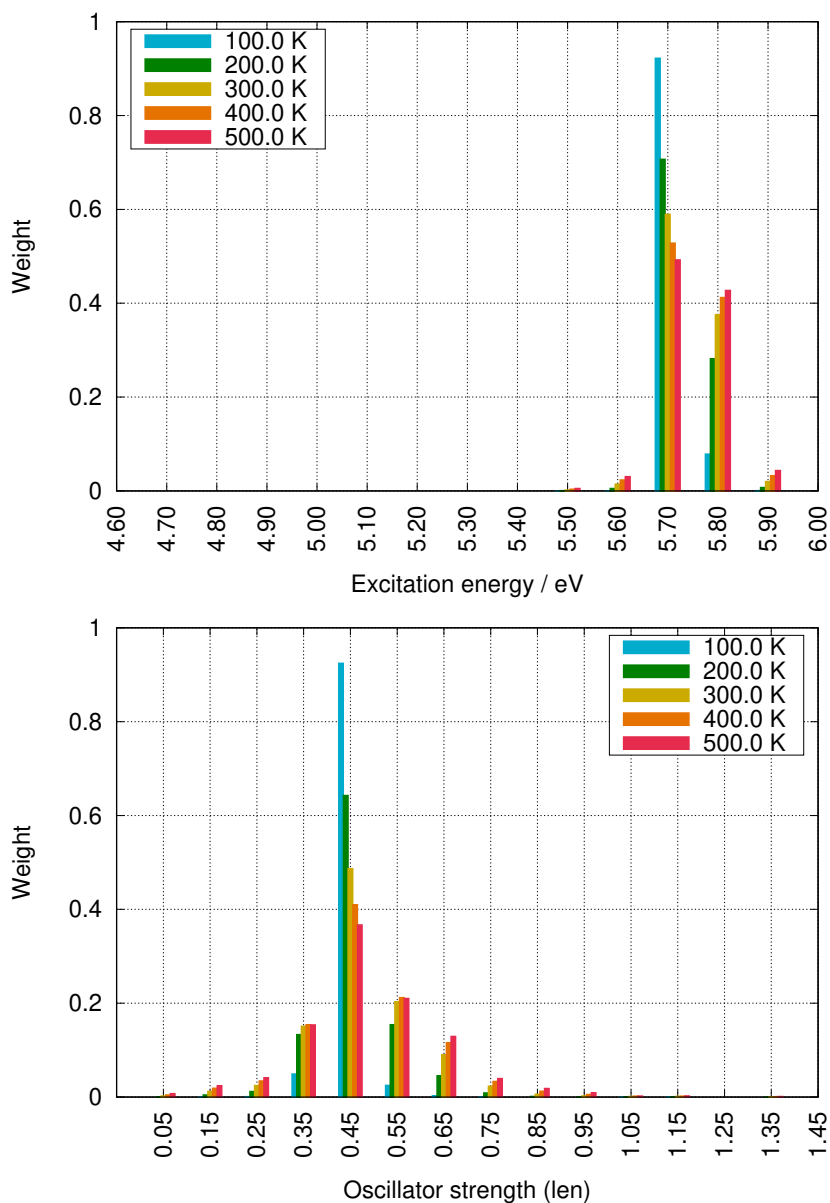


Figure 17: Distribution of excitation energies (top) and oscillator strengths (bottom) of the 5.70 eV peak of the 13.8 k molecules from CBP rotation scan, weighted for different temperatures using a Boltzmann distribution, *cf.* Sec.4.1.2.

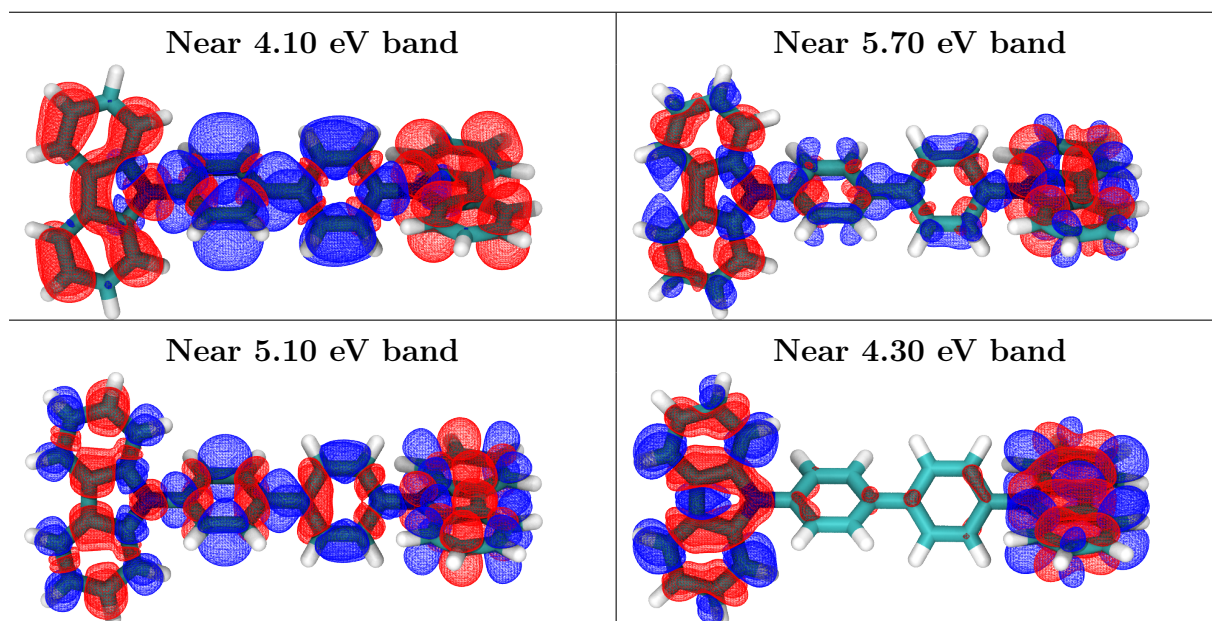


Figure 18: Transition-density plots (isosurface value of  $2 \times 10^{-4} a_0^{-3}$ ) of the absorption bands at 4.10, 5.70, 4.30, and 5.10 eV of  $R_1$ . As shown by Fig. 13, the 4.10 eV, and 5.10 signals decrease drastically as temperature grows. Conversely, the 5.70, and 4.30 eV signals remain mostly unchanged at higher temperatures. Density loss is denoted by a red contour, while increase in density is denoted by a blue contour.

#### 4.3.2 Transition densities of vanishing and non-vanishing bands

To look into the influence of rotational conformation on vanishing and non-vanishing bands, the transition densities of the corresponding excitations are shown in Fig. 18. The top left frame depicts a CT-type excitation for the band near 4.10 eV. On the top right pane, the transition density plot corresponding to the 5.70 eV peak reveals an excitation local character. CT excitations in CBP will be more strongly influenced by the torsional conformation of the molecule, as the relative orientation of the fragments affects the pi-system, where the electron-hole pair is delocalized. For the excitation at 5.70 eV, the orientation of the carbazole and phenyl moieties has virtually no effect on these interactions.

A similar comparison was done for two other vanishing and non-vanishing bands, at 5.10 and 4.30 eV, respectively. The corresponding transition density plots are displayed in the bottom row of Fig. 18. The 5.10 eV band seems to involve also a CT-type excitation, but this character is much weaker in comparison with the 4.10 eV signal.

This could also explain why the decrease in intensity of the 5.10 eV band with higher temperature less pronounced than for the 4.10 eV peak. In contrast, the 4.30 eV peak corresponds to a local excitation involving mainly the carbazole groups, hence it undergoes no major changes with raising temperature.

#### 4.4 Effects of rotational conformation and temperature on emission of CBP

The influence of temperature upon fluorescence of CBP was also investigated. The lowest vertical transition was simulated at different temperatures based on excited-state rotamer geometries. In this case, the rotamer with relative torsion angles of 15, 15, and 30° was found to be lowest in energy, thus it was chosen as reference for the Boltzmann weighting.

The temperature-weighted emission bands are shown in Fig. 19. The emission of the reference excited-state rotamer is included as a black vertical line located at 3.49 eV. The increasing temperature induces a slight blue shift on the emission of CBP, together with a decrease in intensity. This is most noticeable for the 500 K average band, which has a maximum intensity of almost half of the 0K emission. The maxima of the average spectra at 0, 100, 200, 300 400, and 500 K are located at 3.42, 3.45, 3.47, 3.48, 3.49, and 3.49 eV, respectively. Similar to the emission of the minima in the relaxed excited-state geometries, *cf.* Sec. 3.4, the Boltzmann-averaged emission also yields a red shift of approximately 0.40 eV, with respect to the lowest absorption energy. The distribution of the emission bands is analysed in the following.

The statistical data of the energies and oscillator strengths of the emission at the different temperatures is displayed in Tab. 10. The temperature-independent and dependent distribution histograms are shown in Fig. 20 and Fig. 21. Overall, an average blue shift of up to 0.10 eV occurs for the 500 K emission, relative to the 0K spectrum. The distribution of energy data is relatively close. For the oscillator strengths, there is an average decrease of 0.15, relative to the 0 K fluorescence spectrum, which is observed at 500 K. The oscillator strengths have also a relatively small variance.

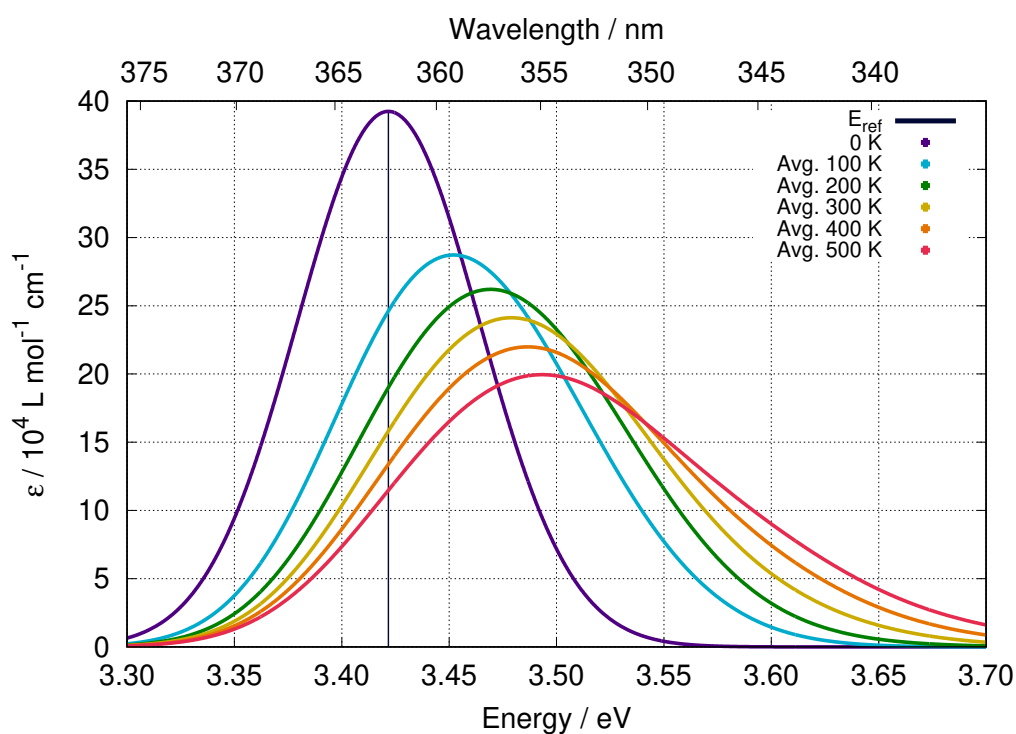


Figure 19: Boltzmann-averaged emission of CBP from the  $S_1$  state within a 0-500 K temperature range. The dark vertical line corresponds to the emission of the rotamer with the lowest total excited-state energy ("15-15-30"). Maxima of the averaged spectra are located at 3.42, 3.45, 3.47, 3.48, 3.49 and 3.49 eV for 0, 100, 200, 300, 400, and 500 K, respectively.

The temperature-independent distribution of the energy, shown on the top pane of Fig. 20, shows a blue shift of emission energies when the dihedrals of CBP are rotated. The oscillator strengths in the temperature-independent scenario (bottom) are spread through a very wide range, where there is a very noticeable amount of rotamers with rather weak emission. When the structures from the torsion scan are weighted using the Boltzmann factor, the distributions from Fig. 21 are obtained. In the temperature-dependent scenario, the distributions of transition energies (top) and oscillator strengths are considerably less scattered, with the highest weights centred around 3.50 eV and 1.40, respectively. Overall, emission seems less sensitive to changes in the rotational conformation of the CBP molecule.

The Boltzmann fit based on ground-state energy differences shows that the ensemble picture has a strong influence on CT-type excitations, while more local excitations are not as sensitive to the ensemble scenario. A similar approach to study the effects of temperature on the emission of CBP shows a much weaker effect of the ensemble

Table 10: Temperature-weighted statistical analysis of the Boltzmann-weighted emission spectra of CBP, *cf.* Fig. 13.

<b>T / K</b>	<b>Emission</b>			
	$\nu^a$		$f^b$	
	$\mu^c$	Var <sup>d</sup>	$\mu^c$	Var <sup>d</sup>
<b>0</b>	3.42	0	1.47	0
<b>100</b>	3.46	<0.01	1.40	<0.01
<b>200</b>	3.48	<0.01	1.38	<0.01
<b>300</b>	3.49	<0.01	1.36	<0.01
<b>400</b>	3.51	<0.01	1.35	0.01
<b>500</b>	3.52	<0.01	1.32	0.03

<sup>a</sup> Excitation energy in eV.<sup>b</sup> Oscillator strength, length gauge.<sup>c</sup> Mean value.<sup>d</sup> Variance.

approach, with a blue shift of up to 0.10 eV relative to the 0K fluorescence. The results in this chapter contribute to understand the relationship between the structure of CBP and its spectral behaviour. However, an improved picture of CBP in the condensed phase needs to account for the interactions of a given molecule with its surroundings. Thus, in the next chapter the excited-state properties of CBP dimers in different environments are investigated.

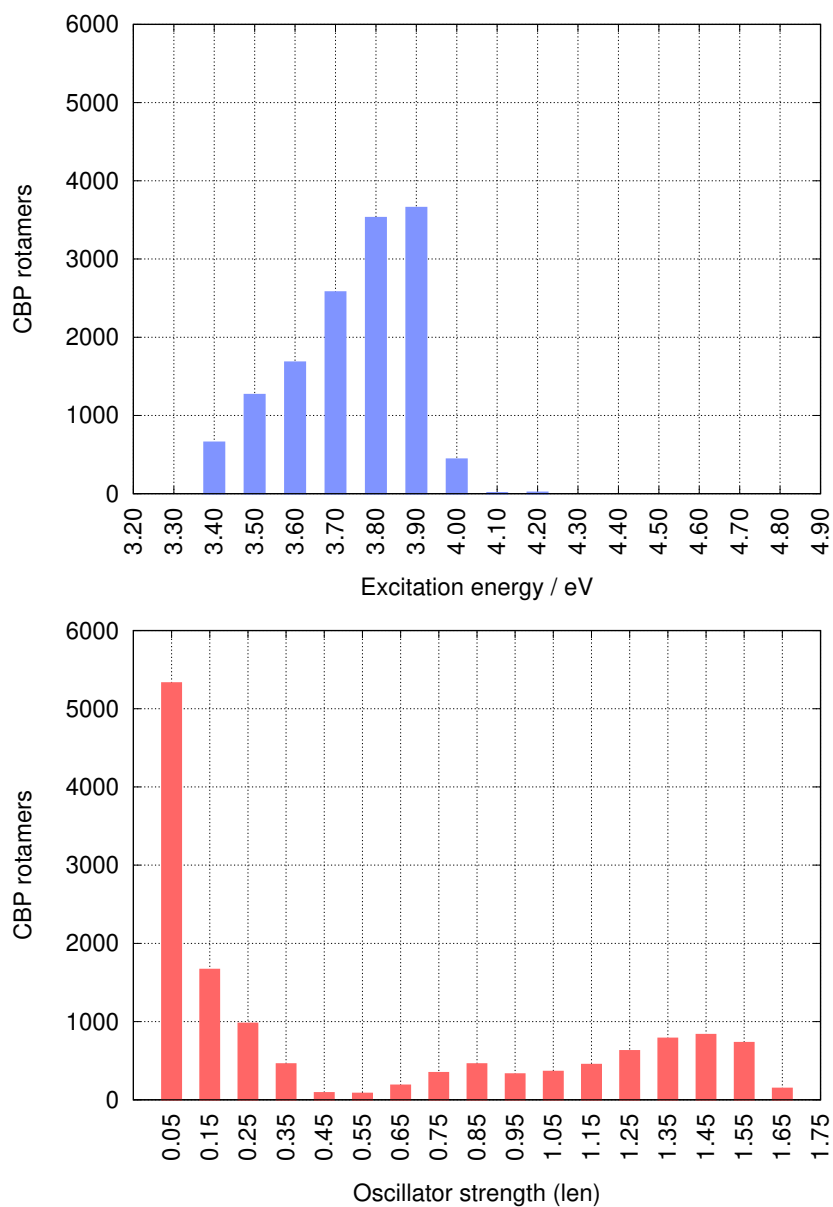


Figure 20: Temperature-independent distribution of the  $S_1$  emission. Top pane corresponds to emission energy. Bottom pane shows data distribution of the oscillator strengths. The vertical axis indicates the number of rotamers in a given excitation energy interval, shown in the horizontal axis.

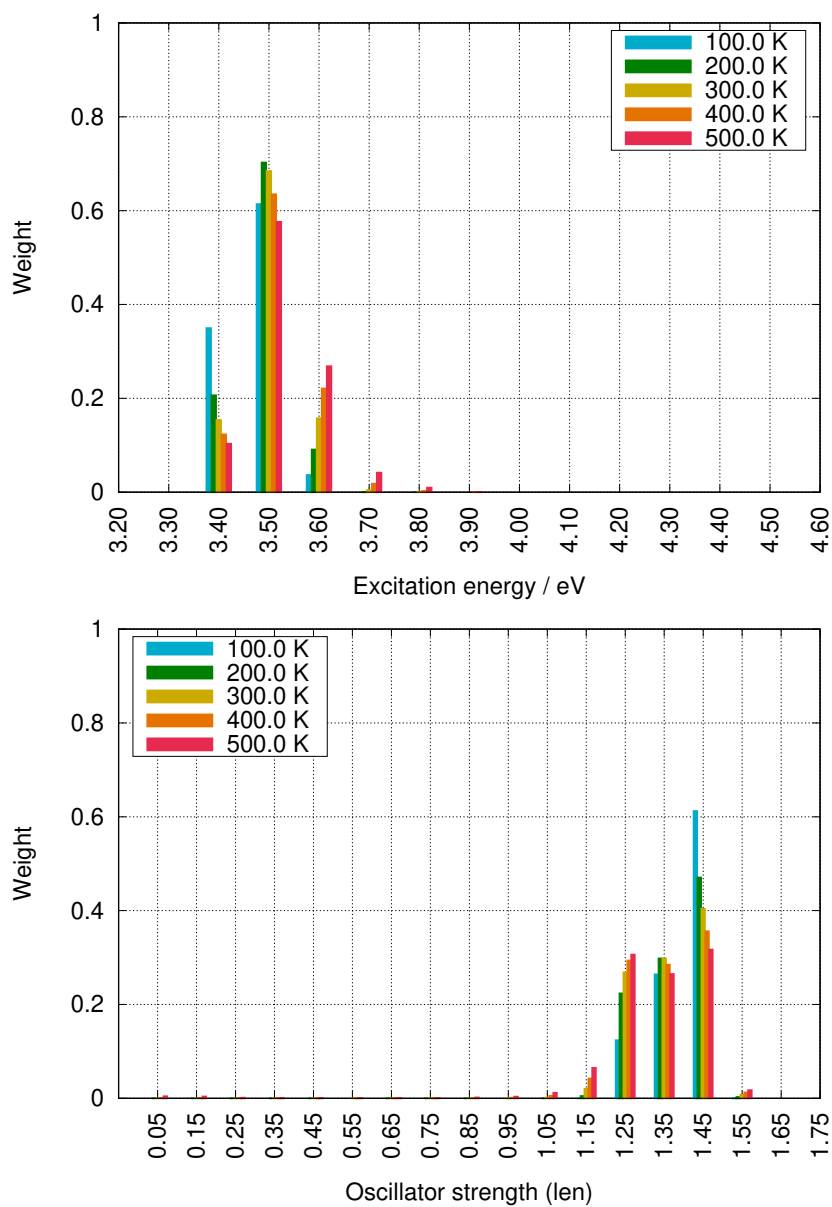


Figure 21: Distribution of vertical transition energies (top) and oscillator strengths (bottom) of the  $S_1$  state of the 13.8 k molecules from CBP rotation scan.

# 5 CBP dimers: excitonic coupling in different environments

In this chapter the excited state properties of CBP dimers in different environments are explored. First, dimers obtained from gas-phase geometry optimizations are used to compare different quantum-chemical methods for calculating excitation energies and excitonic couplings. Second, a set of dimers is extracted from a CBP slab and employed to assess the influence of geometries on the accuracy of excitonic couplings. Finally, dimers are studied within molecular clusters to account for electronic polarization of the environment on excitation energies and couplings. Dimer excitation and couplings are properties that determine exciton transport within the material, hence their importance for multiscale models of devices that employ CBP as part of their architecture.

## 5.1 Computational details

Three sets of CBP dimers are used in the investigation presented here. The first set consists of dimers based on the global minimum structure  $R_1$  (Section 3.2), obtained using gas-phase geometry optimizations. The other two dimer sets were sampled from a CBP slab which contains 5000 molecules. The slab was modelled by Samaneh Inanlou and Deniz Özdemir from the groups of Marcus Elstner and Wolfgang Wenzel.<sup>[21]</sup> The disordered thin-film morphology was generated through simulation of physical vapour deposition, based on a Monte-Carlo, MC, protocol in which molecules are added one after the other to a simulation box where the  $xy$ -plane represents the substrate. Addition of each molecule is followed by a series of simulated annealing cycles, where only molecular translations and rotations of the Ph-Ph and CBZ-Ph dihedral angles, *cf.* Fig. 10, are allowed. The thin-film generated by the deposition protocol was equilibrated through an MD simulation of 2 ns at 300 K and 1 bar. One set of dimers was obtained from the slab, based on a relatively high excitonic coupling, between 50 and 70 meV (slab mean is  $\sim 30$ meV). This coupling was computed in Reference [21] using atomic

transition charges of nearest-neighbour CBP molecules from TD-LC-DFT calculations. The second group of CBP dimer samples were extracted together with their closest 13 molecules, resulting in small molecular clusters of 15 CBPs in total. Dimers were selected by identifying all molecular pairs within a radius of 10 Å, which were then randomly selected. These were inspected to ensure dimers were at least 20 Å from the edges of the simulated CBP slab. This was done to guarantee the complete embedding of the dimers within the clusters.

All calculations presented in this section were performed using the TURBOMOLE program suite.<sup>[73,74]</sup> The details are described in the following.

### 5.1.1 Geometry optimizations

All geometry optimizations of the different dimers in this chapter were carried out at the DFT level,<sup>[75,76]</sup> using the PBE0 functional<sup>[77,78]</sup> with a modified grid<sup>[75]</sup> (grid m3) and the def-SVPD basis set.<sup>[98]</sup> The RI-*J* approximation<sup>[80,81]</sup> was employed with the corresponding auxiliary basis set.<sup>[82]</sup> The Multipole Accelerated RI-*J* (MARI-*J*) option was used to further speed up the calculations.<sup>[99]</sup> Additionally, the DFT-D4 dispersion correction by S. Grimme was also employed.<sup>[100,101]</sup> The derivatives of quadrature weights for correct derivatives of the DFT energy were enabled through the `weight derivatives` option. Geometry optimization thresholds were set to  $10^{-6}$  E<sub>h</sub> for the energy, and  $10^{-3}$  E<sub>h</sub> a<sub>0</sub><sup>-1</sup> for the maximum gradient residual norm. The SCF energy convergence was set to  $10^{-7}$  E<sub>h</sub>.

The geometries of the gas-phase dimers were allowed to fully relax, *i.e.* without constraints. All structures sampled from the CBP slab use MD geometries as a starting point for the optimizations. The sampled dimers were subjected to constrained geometry optimizations, where the nitrogen atoms were kept frozen. This was done to preserve the overall orientation of the monomers and their intermolecular distance. In case of the sampled clusters, a frozen-environment approach was employed. The complete molecular clusters were used in the optimizations, but only the central dimer was allowed to relax while the embedding molecules were kept frozen.

### 5.1.2 Excitation energies

Singlet vertical transition energies were computed for all dimer groups in the gas phase. Additionally, the dimers were split into the individual monomers for which also singlet vertical excitation energies were evaluated. In case of the cluster dimers, excitation energies of the embedded dimers were calculated taking into account the environmental effects due to the small cluster using the frozen density embedding approach. Details of the calculations with the different methods are given below.

A Hartree-Fock single-point calculation was performed as reference for the post-HF methods used to compute the excitation energies of all dimers and monomers. For this calculation the def2-SVPD basis set was used.<sup>[98]</sup> RI approximation was employed with the universal auxiliary basis set.<sup>[82,102,103]</sup> The seminumerical approximation for the HF-exchange (**senex**) was used in all ground- and excited-state calculations throughout this section.<sup>[104,105]</sup> The energy in the SCF iterations was converged to  $10^{-7} E_h$ , and the variations in the electron density to  $10^{-7}$ .

The CIS(D) method was used to compute the lowest 10 singlet excited states<sup>[106]</sup> of the CBP gas-phase dimers, and corresponding monomers, using the def2-SVPD orbital basis set.<sup>[98]</sup> The RI approximation was used with the def2-SVPD auxiliary basis set in all excited-state calculations described here.<sup>[107–109]</sup> The convergence threshold for the ground-state energy was set to  $10^{-7} E_h$ , and  $10^{-6}$  for the residuals of the cluster equations. For the calculation of excitation energies, 76 core orbitals were frozen for the dimers and 38 for the monomers. The convergence threshold for the norm of residual vectors was set to  $10^{-6}$ .

Up to 5 vertical excitations using the Laplace-transformed scale opposite-spin ADC(2) method, LT-SOS-ADC(2), were computed for the gas-phase dimers and monomers.<sup>[50,106,110]</sup> Similar to the CIS(D) calculations, the def2-SVPD basis set was employed with the corresponding auxiliary basis.<sup>[82,98,109]</sup> The number of frozen core orbitals and thresholds for convergence are the same as those used with CIS(D).

The pair natural orbital based version of ADC(2), PNO-ADC(2), was used to calculate up to 5 singlet vertical excitations of dimers and split monomers.<sup>[111,112]</sup> For these, the def2-SVPD basis set and auxiliary basis set were employed.<sup>[82,98,109]</sup> The full

algorithm was selected for the generation of coefficients corresponding to the orbital specific virtuals, OSVs.<sup>[111,113]</sup> The PNO truncation threshold was set to  $10^{-8}$ ,  $10^{-9}$  for the OSV truncation, and  $10^{-7}$  for the energy of the amplitude solver.

Reference single-point calculations of the ground-state geometries were performed at the DFT level<sup>[75,76]</sup> using the CAMB3LYP functional<sup>[96]</sup> with a medium sized grid (grid 4) and the def2-SVPD basis set.<sup>[98]</sup> SCF convergence thresholds were set equal to the HF reference calculations. Singlet vertical excitation energies were evaluated at the TD-DFT<sup>[85-87]</sup> level of theory, using the same functional and basis set. Excitation energies were converged to an Euclidean residual norm of at least  $10^{-5}$ . In all cases 25 excitations were calculated.

The singlet vertical excitations of all dimers and monomers were also calculated employing the *GW*-BSE approach as implemented in TURBOMOLE.<sup>[61,90]</sup> For these calculations, a PBE0/def2-SVPD reference was used, with a set-up similar to that of the DFT reference. HOMO and LUMO energies were corrected using the RI-CD-*evGW* variant.<sup>[84]</sup> The imaginary frequency integration points and Padé approximants was set to 128 (default). The number of excitations to be computed was set to 25.

The DFTB+ program suite<sup>[114]</sup> (v.19.1) was used to compute the lowest 25 excitation energies using the TD-LC-DFTB method. For these calculations, the `mio-0.8` parameter set was employed.<sup>[115]</sup> All calculation parameters were set to default values.

### 5.1.3 Frozen density embedding

The FDE<sup>[116,117]</sup> approach was used to compute up to 5 singlet excitation energies of the dimers within CBP molecular clusters. These calculations were carried out considering the dimer at the centre as active subsystem, and the remaining 13 surrounding molecules as the embedding subsystem. The def2-SVP orbital basis<sup>[79]</sup> and auxiliary basis sets were used for both subsystems. The densities of the subsystems were expanded using the monomolecular basis. To obtain the embedding potential, the PBE<sup>[77]</sup> exchange-correlation functional was used with a medium-sized atomic integration grid (size 3). The non-additive kinetic potential was approximated using the revAPBEk kinetic functional.<sup>[117,118]</sup> The freeze-and-thaw cycles were carried on until the electronic energies of all subsystems converged to at least  $10^{-7} E_h$ , and the densities

to  $10^{-7}$ . Afterwards, excitation energies were computed using the PNO-ADC(2) method following the set-up described above. For the excited-state calculations, the def2-SVP auxiliary basis set was employed.<sup>[82,103]</sup>

### 5.1.4 Excitonic coupling

Excitonic coupling refers to the interactions between individual electronically excited states.<sup>[119]</sup> Coupling of dimers can be studied using the supermolecular and monomer approaches. In the supermolecular picture, coupling of a dimer can be obtained from the excitation energy difference between two interacting states  $n$  and  $m$ . The monomer approach requires the local excitation energies  $\omega_a$  and  $\omega_b$  of monomers  $A$  and  $B$ , correspondingly, to construct a two-state model Hamiltonian:

$$\mathbf{H} = \begin{vmatrix} \omega_a & J \\ J & \omega_b \end{vmatrix}, \quad (86)$$

where  $J$  are the coupling elements. By diagonalizing the matrix given by Eq. (86) the excitation energies of the adiabatic dimer states  $\omega_n$  and  $\omega_m$  can be obtained. The energy difference between the dimer states is then given by

$$\Delta\omega_{nm} = 2\sqrt{\frac{1}{4}\Delta\omega_{ab}^2 + J_{nm,ab}^2}. \quad (87)$$

Equation (87) can be arranged to evaluate the semiempirical exciton coupling  $J$ <sup>[115]</sup>

$$J_{nm,ab} = \frac{1}{2}\sqrt{\Delta\omega_{nm}^2 - \Delta\omega_{ab}^2}. \quad (88)$$

When dimers are symmetric the local excited states on monomers  $A$  and  $B$  are equal, thus  $\Delta\omega_{ab} = 0$ . The coupling,  $J$ , is sometimes approximated through  $\Delta\omega_{nm}$  directly from the supermolecular calculation, even for cases where  $\Delta\omega_{ab} \neq 0$ ,

$$J_{nm} = \frac{1}{2}\Delta\omega_{nm}. \quad (89)$$

In cases where there mixing with other states is absent, Eq. (88) yields the exact coupling. If mixing is not significant, Eq. (88) still holds as a good approximation. However, for cases with considerable state mixing, the two-state model Hamiltonian

is a poor description in general, hence Eq. (88) will also yield a poor description, *e.g.*  $\Delta^2\omega_{ab} > \Delta^2\omega_{nm}$ .

## 5.2 Gas-phase CBP dimers

For this section, a set of five dimer structures was obtained from the gas-phase geometry optimization of dimers built using the geometry of the global minimum  $R_1$ . The converged dimers, labelled as anti-sandwich (AS), sandwich (S), T-shape (T) and X-shape (X), are shown in Fig. 22. Information regarding their structural parameters is given in Tab. 11. Torsion angles and bond distances were measured according to Section 3.2. Intramonomer bond distances, between fragments 1-2, 2-3, and 3-4, match those of the local minima monomers. In the dimers, intermonomer distances were measured between the closest atoms.

### 5.2.1 Optimized geometries

The monomers in system S have differences in torsion angles 1-2 and 3-4 of about  $+10^\circ$ , while for dihedral 2-3 is around  $+8^\circ$ , with respect to the global minimum,  $R_1$ . The stacked, symmetric conformation of this dimer translates to almost identical structural features in both monomers, which have the largest intermonomer distance in the set, of 3.72 Å. System S is the most stable, and also has the lowest binding energy,  $E_{\text{bind}}$ , of  $-193.6$  kJ/mol.

System AS has torsion angles Ph-Ph close to  $36^\circ$  for both monomers, in agreement with the local minima geometries. In each monomer of system AS, one of the CBZ-Ph torsion angles is in agreement with the minima, near  $\pm 55^\circ$ , while the other is slightly shifted by about  $\pm 10^\circ$ . This change could be caused by the intermolecular interaction of the carbazoles, which are about 3.57 Å apart. System AS is the least stable in this set of dimers, with a relative energy,  $E_{\text{rel}}$ , of 96.2 kJ/mol with respect to dimer S. This dimer also has the weakest  $E_{\text{bind}}$  of  $-97.4$  kJ/mol.

In system T, one monomer maintains the Ph-Ph and one CBZ-Ph torsion angles close to those of the gas-phase minima, while the carbazole approaching the other monomer seems to cause a  $+10^\circ$  change in the CBZ-Ph angle. The other monomer is distorted about  $+10^\circ$  both in CBZ-Ph and Ph-Ph angles. System T has the smallest

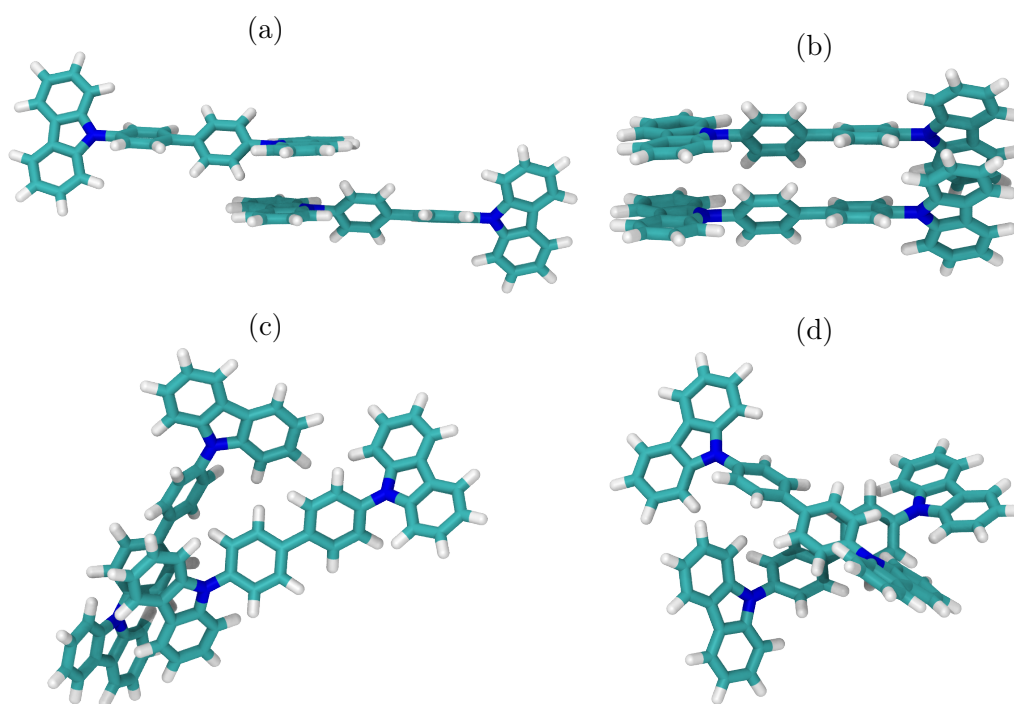


Figure 22: CBP dimers obtained from gas-phase geometry optimizations: a) Anti-Sandwich, AS, b) Sandwich, S, c) T-shape, T, and d) X-shape, X.

intermonomer separation, of nearly 3.19 Å. It is the second most stable dimer in the set, with  $E_{\text{rel}}$  of 63.8 kJ/mol, with respect to system S, and binding energy of  $-130.9$  kJ/mol.

System X has a  $+8^\circ$  rotation in one of the CBZ-Ph dihedrals, which correspond to the groups approximating the other monomer, separated by 3.58 Å. All other structural parameters are conserved from the monomer minima. System X has a  $E_{\text{bind}}$  of  $-106.13$  kJ/mol, and is the third in descending stability with  $E_{\text{rel}}$  of 87.3 kJ/mol, relative to system S .

The completely-stacked monomer arrangement in dimer S results in the most stable dimer, which also has the strongest binding energy. Inter monomer interaction between parallel, non-coplanar carbazoles, like in dimer AS, results in weaker binding energies and overall lower stability. Interaction between biphenyl moieties, like in dimer X, gives a similar result as CBZ-CBZ dimers in terms of stability.

Table 11: Structural parameters of monomers, I and II forming the optimized gas-phase dimers AS, S, T, and X. Dihedral angles, Dih., are given in degrees; distances,  $r$ , are given in Å, *c.f.* Sec. 3.2. Relative energies,  $E_{\text{rel}}$ , and binding energies,  $E_{\text{bind}}$ , in kJ/mol.

System		AS	S	T	X
<b>I</b>	Dih. 1-2	-53.7	-46.2	-44.3	-51.1
	Dih. 2-3	37.3	42.0	-47.2	33.5
	Dih. 3-4	-43.3	-44.8	-48.7	-53
	$r$ 1-2	1.41	1.41	1.41	1.41
	$r$ 2-3	1.47	1.47	1.47	1.47
<b>II</b>	Dih. 1-2	53.9	-44.8	-46.2	-48.7
	Dih. 2-3	36.4	42.0	33.0	33.0
	Dih. 3-4	67.9	-48.6	-54.1	-52.6
	$r$ 1-2	1.41	1.41	1.41	1.41
	$r$ 2-3	1.47	1.47	1.48	1.47
<b>Dimer</b>	$r$	3.57	3.72	3.19	3.58
	$E_{\text{rel}}$	96.21	0.00	62.77	87.30
	$E_{\text{bind}}$	-97.41	-193.62	-130.85	-106.13

### 5.2.2 Excitation energies

The singlet excitation energies of systems AS, S, T, and X were computed at the CIS(D), LT-SOS-ADC(2), PNO-ADC(2), *GW*-BSE, TD-DFT and TD-LC-DFTB levels, *cf.* Sec. 5.1. The five lowest excitation energies of these dimers, computed with each of the above methods, are given in Appendix A.1.1.

In Fig. 23, the PNO-ADC(2) excitation energies are plotted for dimers AS, S, and T. The lowest excitation energy of system S is at 3.79 eV. Systems AS and T are slightly blue shifted, at 3.89 and 3.92 eV. The  $S_2$  state of system T is almost degenerate, with a difference of less than 0.01 eV relative to  $S_1$ . For dimers AS and S the  $S_2$  state is 3.91, and 3.84 eV, respectively. The  $S_3$  state is very close to the  $S_2$  of dimer S, at 3.48 eV, whereas the third singlet state is higher for systems AS and T, at 4.08 and 3.98 eV, respectively. From  $S_3$  on, the trend between systems AS and T becomes inverted, and AS has higher excitation energies respect to system

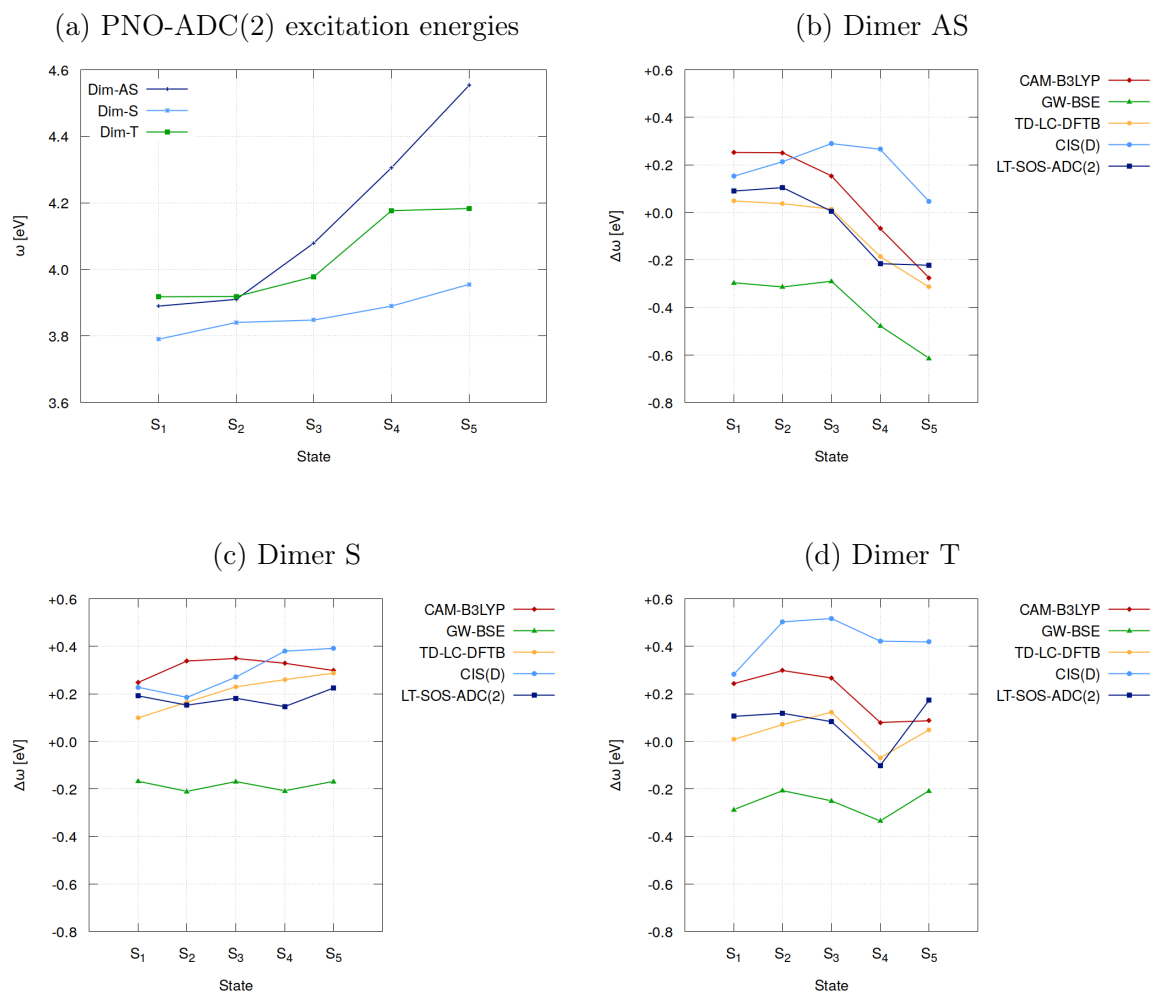


Figure 23: (a) PNO-ADC(2) excitation energies of the gas-phase dimers AS, S, and X. (b-d) Excitation energy difference,  $\Delta\omega$ , with respect to PNO-ADC(2).

T:  $S_4$  and  $S_5$  are nearly 0.15 and 0.50 eV higher, respectively.  $S_1$ ,  $S_2$ , and  $S_3$  of system S are about 0.10, 0.07, and 0.15 eV lower in energy than its counterparts. Dimers S and AS have a difference in  $S_4$  and  $S_5$ , close to 0.40 and 0.60 eV. With respect to dimer S,  $S_4$  and  $S_5$  of dimer T are 0.30 to 0.20 eV higher in energy. Excitation energies are overall lower for dimers with stronger binding energies, *i.e.* S and T.

Method accuracy was assessed by comparison of dimer excitation energies with respect to PNO-ADC(2). The energy differences of the TD-DFT, GW-BSE, TD-LC-DFTB, CIS(D), and LT-SOS-ADC(2) are shown in Fig. 23.

The TD-DFT energies (red) of system AS excitations up to  $S_3$  are about 0.20 eV higher than PNO-ADC(2),  $S_4$  is in relative good agreement, and  $S_5$  is lower by about 0.25 eV. For system S, energies are overestimated by at least 0.20 eV and up to 0.36 eV with respect to PNO-ADC(2). For dimer T, the first three states are overestimated by about 0.25 eV, and the  $S_4$  and  $S_5$  by about 0.10 eV relative to PNO-ADC(2).

Regarding the results from *GW*-BSE calculations (green), it can be seen that these are underestimated at least 0.20 eV for the set of dimers discussed in this section. The underestimation is slightly less pronounced for systems S and T, whereas for dimer AS it is at least 0.26 eV.

The TD-LC-DFTB results (yellow) are the closest to those from PNO-ADC(2), particularly in the two lowest states. In case of dimer AS,  $S_3$  is on par with the reference, but then  $S_4$  and  $S_5$  become significantly underestimated close to 0.20 and 0.24 eV. For dimer S, TD-LC-DFTB results are always greater than the reference:  $S_1$  is 0.10 eV higher, but the difference increases with the state. The  $S_1$  of dimer T is very similar to the reference;  $S_1$ ,  $S_2$ , and  $S_4$  are slightly overestimated, while  $S_3$  is 0.08 eV below PNO-ADC(2).

Next, CIS(D) (light blue) is overestimated in all cases at least about 0.20 eV. For dimer AS, the difference increases with the state in general; however  $S_5$  has the best agreement with PNO-ADC(2) among all compared methods. In case of system S, the  $S_2$  state is slightly lower than the first excitation, but all following states are higher than PNO-ADC(2) about 0.20-0.4 eV. As for system T, CIS(D) excitation energies increase up to 0.50 eV for  $S_3$ , followed by a decrease to about 0.40 eV for  $S_4$  and  $S_5$ , relative to the reference.

LT-SOS-ADC(2) energies (dark blue) of system AS are overestimated for the  $S_1$  and  $S_2$  states, about 0.10 eV, while  $S_4$  and  $S_5$  are about 0.20 eV below the reference.  $S_3$  is in good agreement with PNO-ADC(2). For the S system,  $S_1$  is 0.20 eV above PNO-ADC(2),  $S_2$  is almost the same as TD-LC-DFTB at 0.18 eV above the reference  $S_3$ ,  $S_4$  and,  $S_5$  are all within the 0.20 eV difference. The LT-SOS-ADC(2) excitation energies of system T show a slight overestimation of the  $S_1$  and  $S_2$  states of approximately 0.10 eV respect to the reference method;  $S_3$  is lowered about 0.02 eV respect to the first two states;  $S_4$  is at  $-0.90$  eV; and  $S_5$  is 0.20 eV higher than PNO-ADC(2).

Table 12: Excitonic couplings,  $J_{nm,ab}$  in eV, of the A, AS, T, and X dimers. Excitation energies are given in the Appendix (A.1.1).

Dimer	TD-DFT	<i>GW</i> -BSE	TD-LC-DFTB	CIS(D)	LT-SOS-ADC(2)	PNO-ADC(2)
<b>AS</b>	6	0*	3	0*	17	10
<b>S</b>	70	4	58	0*	5	25
<b>T</b>	0*	40	20	110	7	0*
<b>X</b>	17	0*	10	28	2	- <sup>a</sup>

\*  $\Delta\omega_{nm} < \Delta\omega_{ab}$  in Eq. (88).

<sup>a</sup> calculation did not converge.

Since the  $S_1$  and  $S_2$  are the states considered to calculate excitonic couplings according to Eq. 88, the method comparison indicates that the best alternative to PNO-ADC(2) is the TD-LC-DFTB method.

### 5.2.3 Excitonic couplings

Excitonic couplings,  $J_{nm,ab}$ , of dimers AS, S, T, and X were calculated using the two-state model, Eq. (88). The corresponding results are collected in Tab. 12. The table shows considerable differences between the methods, even in the qualitative ordering of the dimers. For example in TD-DFT, TD-LC-DFTB, and PNO-ADC(2), system S has the highest excitonic coupling in the series. The second in order of decreasing coupling is dimer X for TD-DFT, whereas for TD-LC-DFTB it is dimer T, and for PNO-ADC(2) corresponds to system AS. The dimers with the third strongest coupling are AS for TD-DFT, X for TD-LC-DFTB, and T for PNO-ADC(2). The weakest coupled are T for TD-DFT, and AS for TD-LC-DFTB. For *GW*-BSE, dimers in decreasing order of coupling are T, S, AS, and X. The dimer ordering from CIS(D) results, also in descending order of coupling, are T, X, AS, and S. The descending order for LT-SOS-ADC(2) corresponds to AS, T, S, and X. The big differences in the results from *GW*-BSE, CIS(D), and LT-SOS-ADC(2) methods could indicate that they are less adequate to describe excitonic coupling in these systems. There seems to be good agreement between TD-DFT and PNO-ADC(2) regarding excitonic coupling. Nonetheless, due to the good overall agreement with the PNO-ADC(2) reference,

TD-LC-DFTB can be considered a reasonable alternative to study excitonic coupling in CBP, especially if the use of fast computational methods is required.

### 5.3 Influence of dimer geometry

In the previous section, a framework of methods to compute excitonic couplings in CBP was established. Using PNO-ADC(2) as reference, the TD-LC-DFTB method showed the best agreement in dimer excitation energies. In this section, the importance of monomer geometries for accurate description of excitonic couplings is assessed. For this purpose, a set of five dimer geometries, extracted from a CBP slab, is studied without any additional environment molecules. The dimers from the slab recover structural effects that the unconstrained, fully-relaxed dimers do not.

The structural parameters of the relaxed DFT geometries, *cf.* Sec. 5.1.1, and unrelaxed MD structures are collected in Appendix A.3. Inspection of the geometries shows differences between the MD unrelaxed and relaxed DFT structures, with the latter being in better agreement with the bond distances and dihedral angles of the global minimum. In particular, the CBZ-Ph bond distances are generally underestimated in the unrelaxed MD geometries, with differences between 0.01-0.09 Å relative to the global minimum,  $R_1$ . Also, the Ph-Ph bond is overestimated in the MD geometries, with variations up to 0.08 Å with respect to  $R_1$ . In the unrelaxed MD geometries there is a noticeable bend on the CBZ angle, which is not observed in any of the local minima or gas-phase dimer structures. This distortion can be seen in Fig. 24, where the unrelaxed MD (a) and relaxed DFT (b) geometries of one of the monomers in dimer E are compared. Ideally, the red markers in the perpendicular perspective (upper) should be aligned, as observed in all fully-relaxed structures. However, in the unrelaxed MD geometry such angle differs by about 25° from the  $R_1$ , whereas the relaxed DFT geometry differs approximately 3°. The lower panel shows a close-up of the same angle, viewed from a parallel perspective relative to the plane of the document. Overall the CBZ angle has variations between 3 and 30°, relative to  $R_1$ . On the other hand, the relaxed DFT geometries have a carbazole distortion of 1-6°.

The relaxed DFT geometries were compared to the unrelaxed MD structures employing mean relative differences, MRD, of total energies with respect to  $R_1$ , *cf.* Sec. 3.2. The MRD was calculated by averaging the monomer total energies per dimer. The

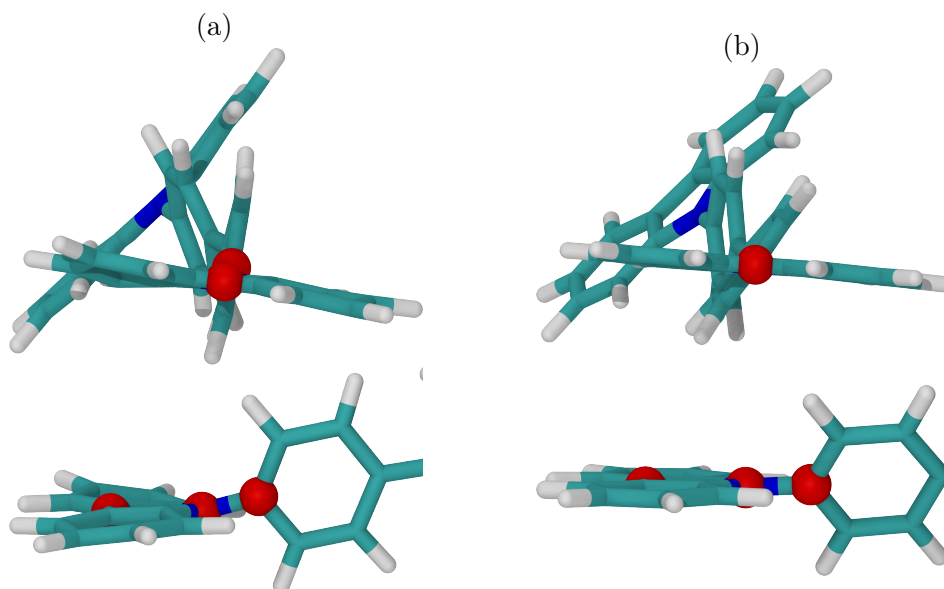


Figure 24: Distortion of the CBZ angle of monomer  $ii$  extracted from dimer E, measured at (a) unrelaxed MD and (b) relaxed DFT geometry. Structures are shown perpendicular (upper) and parallel (lower, close-up) to the plane of the document. The red markers correspond to the points used to measure the angle.

results are given in Fig. 25. The plot shows a difference of 200 kJ/mol between the geometries: the unrelaxed MD geometries average at about 220 kJ/mol while the relaxed DFT geometries average around 20 kJ/mol above the global minimum, *cf.* Tab. 1. The MRD discrepancy between unrelaxed MD and relaxed DFT geometries is a qualitative measure of the structural differences. In particular, the off-axis distortion of the carbazole group and the bond distance can have significant effects on the properties of the molecules. One example is the effect of the shortened Ph-Ph bond when CBP is relaxed in the lowest excited state, resulting in a red shift of the first excitation of about 0.4 eV (*cf.* Sec. 3.4.1 and 4.4). Thus, in the following the influence of dimer geometry on excitation energies and excitonic couplings is assessed.

### 5.3.1 Excitation energies

The five lowest PNO-ADC(2) singlet excitations of the relaxed DFT dimers are displayed in Fig. 26. The excitation energies are collected in Appendix A.1.3. The first excitation energies of D, E, F, G, and H are 3.64, 3.80, 3.68, 3.69, and 3.70 eV, respectively. For the first excitation it can be noticed that the energies of systems F, G, and H, at 3.68, 3.69, and 3.70 eV, respectively, are grouped with differences

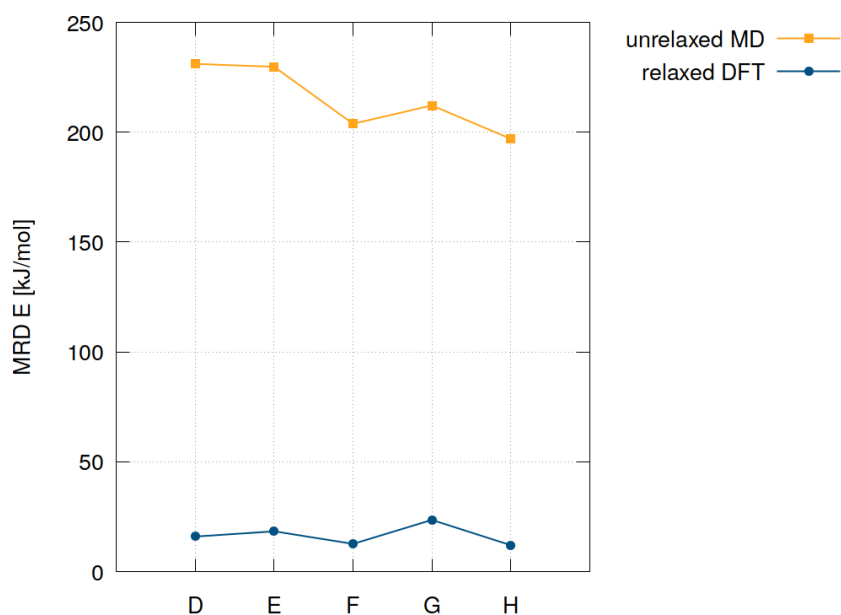


Figure 25: Mean relative differences, MRD, of total energies, of unrelaxed MD and relaxed DFT geometries, with respect to to the global minimum  $R_1$ . For each dimer, monomer values were averaged.

of less than 0.020 eV. Dimer D is slightly lower, at 3.64 eV, while dimer E has the highest  $S_1$ , at 3.79 eV. The difference between the  $S_1$  states could indicate that the influence of the confinement on the geometries can lead to shifts of at least 0.10 eV. Effects from bulk confinement can be further observed by comparing these results with the excitation energies of dimers AS, S, and T (*cf.* Fig. 23). Despite the different monomer arrangements, all  $S_1$  excitation energies are 0.10-0.20 eV higher than the F, G, and H dimers. This suggests that the shift cannot be attributed only to monomer arrangement, but rather structural effects that are not present in the fully relaxed geometries.

Starting from the  $S_2$  state, the differences in excitation energies become smaller:  $S_2$  is located around  $3.81 \pm 0.02$  eV,  $S_3$  at  $3.83 \pm 0.03$  eV,  $S_4$  at  $3.86 \pm 0.03$  eV, and  $S_5$  at  $3.88 \pm 0.02$  eV. For these states, there is also a marked difference with respect to the fully relaxed dimers, where the  $S_5$  is at least 0.10 eV, and up to 0.30 eV higher. Though investigation of the specific effects causing these shifts is beyond the scope of this thesis, the results highlight the importance of bulk confinement for the correct description of CBP dimer excitations.

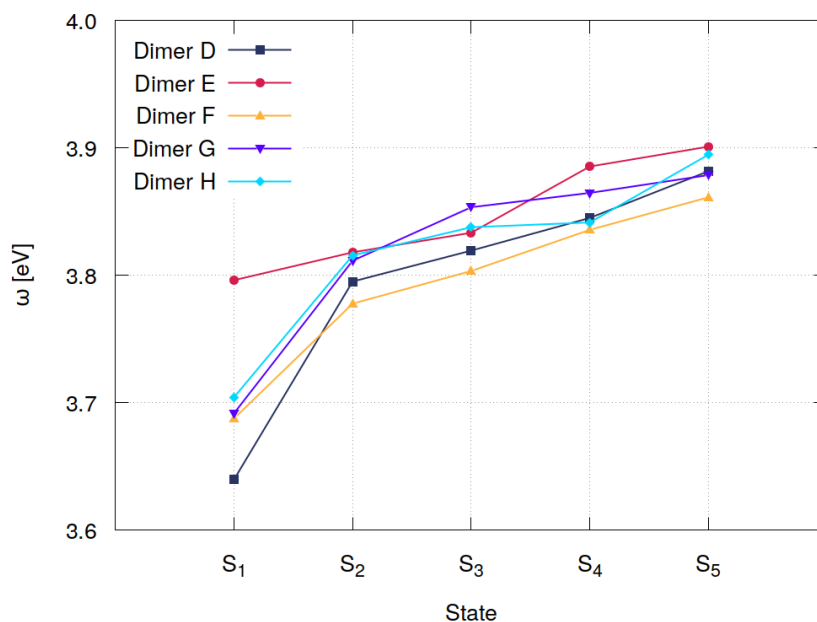


Figure 26: PNO-ADC(2) singlet excitation energies of the relaxed DFT geometries.

The PNO-ADC(2) data of the relaxed DFT geometries was employed to assess the influence of dimer structure on excitation energies. This was achieved by calculating the mean absolute deviation (MAD) of excitation energies of the unrelaxed MD geometries, at the TD-LC-DFTB and PNO-ADC(2) levels, and the TD-LC-DFTB excitations of the relaxed DFT dimers. The results are shown in Fig. 27, where the excitation energies from unrelaxed MD geometries are displayed as dashed lines, and the TD-LC-DFTB at relaxed DFT geometries correspond to the blue plot. It can be seen that a variation of up to 0.11 eV in the PNO-ADC(2) results can occur by using the unrelaxed MD geometries. The largest difference is observed for the S<sub>1</sub> and S<sub>2</sub> states. This can lead to larger errors when using the two-state model Hamiltonian to compute the excitonic couplings, especially if the simplified model, Eq. (89), is used. The TD-LC-DFTB results from unrelaxed MD geometries have a similar problem for the lowest state, which gets reduced in S<sub>2</sub> to about 0.07 eV. However, the differences with respect to the reference increase drastically for the higher states up to almost 0.18 eV. In case of the excitations of the relaxed DFT geometries at the TD-LC-DFTB level, the S<sub>1</sub> and S<sub>2</sub> states have the smallest MAD, near 0.06, and 0.07 eV, correspondingly. For the S<sub>3</sub> state, and up to the S<sub>5</sub>, the MAD increases up to 0.26 eV. Still, the smaller deviation in the lowest two states suggests that the TD-LC-DFTB method, in combination with relaxed DFT geometries, could be a good option to compute excitonic couplings within the two-state approximation.

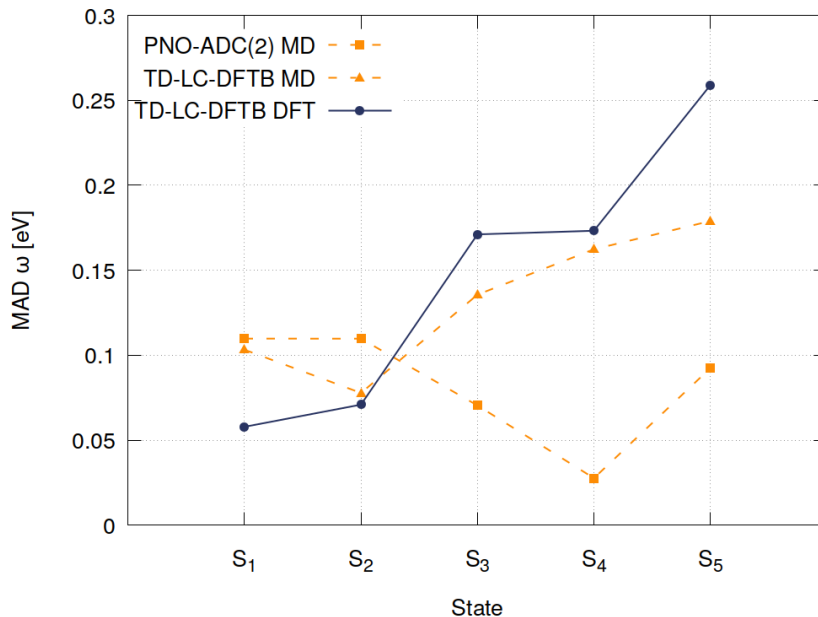


Figure 27: Mean absolute deviation (MAD) of excitation energies,  $\omega$ , with respect to the PNO-ADC(2) results of the relaxed DFT geometries.

### 5.3.2 Excitonic couplings

In this section, the influence of the geometries on excitonic couplings is assessed. The couplings were computed from the PNO-ADC(2) and TD-LC-DFTB excitations, using the two-state model, Eq. (88), and the simplified version for symmetric dimers, Eq. (89). The results are collected in Tab. 13. Within each method, the geometry is indicated for the unrelaxed MD and relaxed DFT geometries, for which the couplings  $J_{nm}$  and  $J_{nm,ab}$  were computed.

A comparison of  $J_{nm}$  can be used as a measure for the accuracy of the simplified two-state model. For example, the differences in  $J_{nm}$  and  $J_{nm,ab}$  for the same geometry and method would indicate that some dimers are not symmetrical, thus the influence local excitations of monomers  $A$  and  $B$  need to be considered for an accurate description of excitonic couplings. If  $J_{nm}$  results from the same method are compared across geometries, it works as an estimate of the effects due to structural relaxation. For example, relaxing dimers D, F, and H, leads to an increase in the coupling, whereas for dimer E the opposite effect is observed. For equal geometries, comparison of  $J_{nm}$  across methods gives an overall measure of the accuracy of the simplified two-state model. In case of unrelaxed MD geometries, TD-LC-DFTB yields couplings up to 75

Table 13: Excitonic couplings, in meV, computed for the unrelaxed MD, and relaxed DFT geometries of dimers D-H. Excitation energies are given in Appendix A.1.2 and A.1.3.

Dimer	TD-LC-DFTB				PNO-ADC(2)			
	MD		DFT		MD		DFT	
	$J_{nm}$	$J_{nm,ab}$	$J_{nm}$	$J_{nm,ab}$	$J_{nm}$	$J_{nm,ab}$	$J_{nm}$	$J_{nm,ab}$
<b>D</b>	50	0*	64	59	19	19	78	75
<b>E</b>	115	52	38	31	42	32	11	0*
<b>F</b>	58	52	76	63	29	9	45	45
<b>G</b>	48	48	57	49	76	75	60	56
<b>H</b>	76	31	50	48	1	0*	56	55

\*  $\Delta\omega_{nm} < \Delta\omega_{ab}$  in Eq. (88).

meV higher than the PNO-ADC(2), observed for dimers E and H. For relaxed DFT geometries, the largest difference is about 30 meV, for dimer F.

We decided to employ  $J_{nm,ab}$  as a qualitative measure of the accuracy of the geometries. In particular, comparison across methods shows that unrelaxed MD geometries have poor agreement, where differences can be as high as 43 meV, but not less than 20 meV. In contrast, the TD-LC-DFTB and PNO-ADC(2) couplings from relaxed DFT geometries have an overall improved agreement, with differences between 30 and 7 meV. Thus, if accurate excitonic couplings are sought, the  $J_{nm,ab}$  approach should be used with excitation energies computed for relaxed DFT geometries. It is worth noting that couplings of the relaxed D-H dimers are at least 20 meV higher than those of the AS, S, and T dimers, *cf.* Tab. 12, stressing the importance of confinement for accurate dimer structures.

In the following, a comparison of the excitonic couplings,  $J_{nm,ab}$ , calculated for the unrelaxed MD and relaxed DFT geometries using the TD-LC-DFTB, PNO-ADC(2), *GW*-BSE, and TD-DFT methods is presented. The differences,  $\Delta J_{nm,ab}$ , from unrelaxed MD and relaxed DFT geometries, relative to PNO-ADC(2) at DFT geometries, are shown in Fig. 28. *GW*-BSE and TD-DFT couplings are included in Appendix A.2.1.

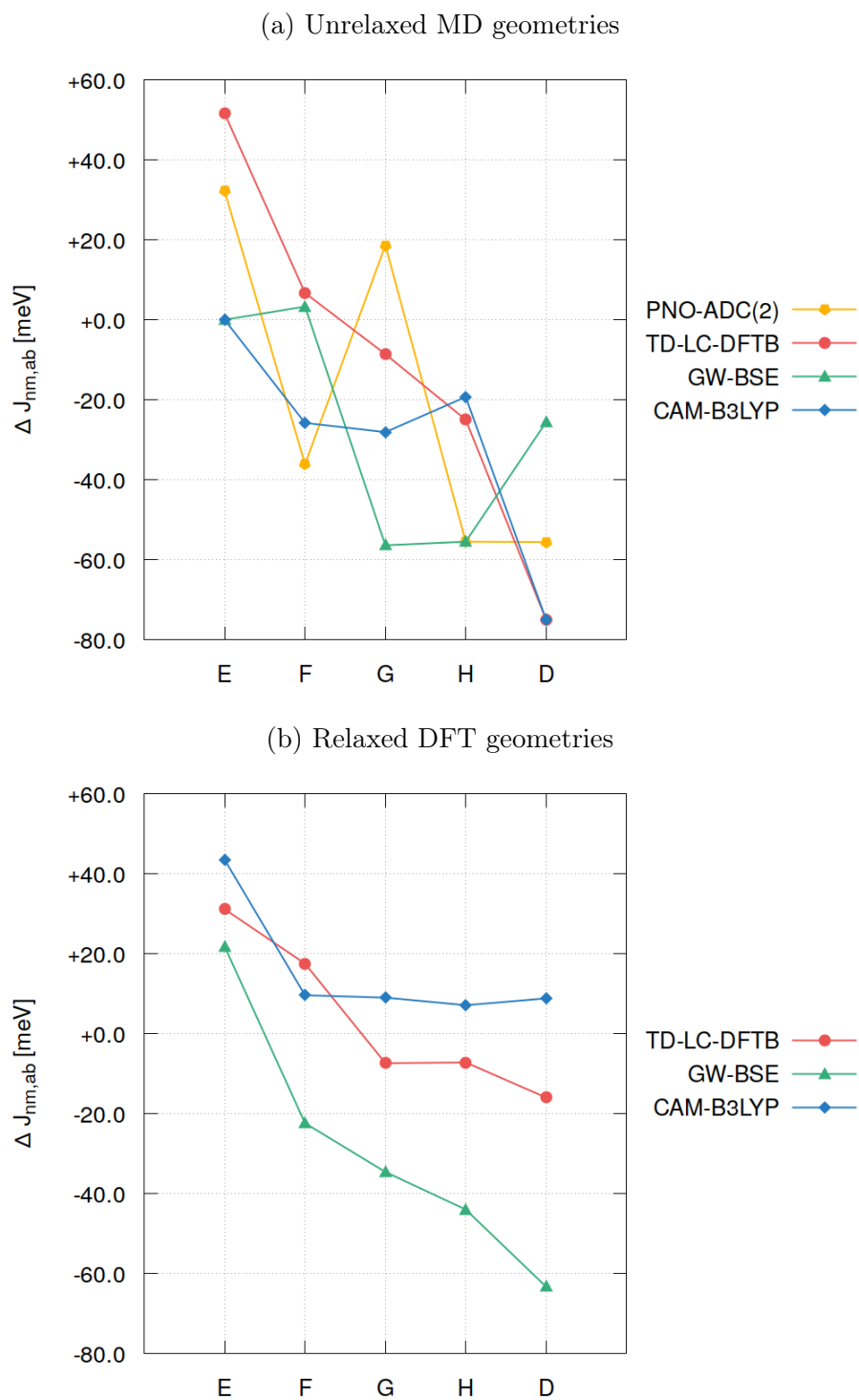


Figure 28: Difference in excitonic couplings,  $\Delta J_{nm,ab}$ , with respect to the PNO-ADC(2) results of relaxed DFT geometries. Dimers were arranged in decreasing order of  $\Delta J_{nm,ab}$ , according to the TD-LC-DFTB results at relaxed DFT geometries.

First, the unrelaxed MD geometries, in Fig. 28a, are discussed. The  $\Delta J_{nm,ab}$  of PNO-ADC(2) (yellow) shows large a variation for all systems with respect to the relaxed geometry, ranging from +30 to  $-55$  meV. In this case, no MD dimer is within  $\pm 20$  meV from the reference. This difference also suggests a high sensitivity of the method to the geometries. The  $\Delta J_{nm,ab}$  plot from TD-LC-DFTB (red) show that dimers F and H vary less than  $\pm 10$  meV from the PNO-ADC(2) couplings with DFT geometries. Dimer H is at  $-20$  meV, while E and F have a  $\Delta J_{nm,ab}$  of +50 and  $-75$  meV. Regarding the *GW*-BSE results (green) the excitonic coupling of dimer E vanishes, since  $\Delta\omega_{ab}^2 > \Delta\omega_{nm}^2$  in Eq. (88), hence the match with the reference. Dimer F is also a close match, within 3 meV. Dimers G and H differ around  $-55$  meV, while coupling of dimer D is underestimated about 20 meV. The TD-DFT results with the CAM-B3LYP functional (blue) also yield a vanishing excitonic coupling for systems D and E, while F, G, and H are around 20 meV lower with respect to the PNO-ADC(2) couplings at relaxed DFT geometries. System D is almost 80 meV lower, which is the largest  $\Delta J_{nm,ab}$  from the TD-DFT method with respect to the reference.

Regarding the  $\Delta J_{nm,ab}$  results from TD-LC-DFTB at relaxed DFT geometries in Fig. 28b, there is an improvement for systems E, at +30 meV, G and H, around  $-8$  meV and D at  $-18$  meV. Dimer F is shifted up to +20 meV after structure relaxation, which is about 15 meV higher than the relaxed MD geometry. After optimization, the  $\Delta J_{nm,ab}$  results from *GW*-BSE calculations remain underestimated for dimers F, G, H, and D, at  $-20$ ,  $-38$ ,  $-41$ , and  $-62$  meV. Dimer D is about +20 meV higher than the PNO-ADC(2) reference. The TD-DFT coupling differences of all dimers have a positive shift due to geometry optimization, with  $\Delta J_{nm,ab}$  of dimers E-H at +42, +12, +11, +10, and +12 meV. The excitonic couplings from the relaxed DFT geometries are about 40 meV higher than those at unrelaxed MD structures, without considering D and E which have a vanishing  $J_{nm,ab}$ , due to  $\Delta\omega_{ab}^2 > \Delta\omega_{nm}^2$ . Overall, relaxation of the geometries reduces the differences in excitonic couplings between PNO-ADC(2) and TD-LC-DFTB, also improving TD-DFT results to a good extent.

The results obtained in this section indicate that, if excited-state properties are sought for a given dimer from the bulk, geometries from MD simulations need to be re-optimized using more accurate methods. This is because there are some structural features that are crucial for excited-state properties, which are not accurately described by MD. In particular, the distance of the Ph-Ph bond can induce a shift of approximately 0.4 eV between the absorption and emission as discussed in Sec. 3.4.1

and 4.4. Geometry re-optimization is further encouraged by the relative energies, with respect to  $R_1$ , of unrelaxed MD and relaxed DFT monomers. These results suggest that the latter are substantially more stable, thus better suited for high accuracy methods. However, optimization until full relaxation of the geometries should not be pursued. Otherwise, important effects from the bulk confinement would be lost, leading to inaccurate description of properties. We found that a mixed approach would be adequate, where dimers are sourced from a simulated slab, while DFT constrained re-optimizations are performed to “fine-tune” the geometries.

With sufficiently accurate geometries, we consider the two-state model,  $J_{nm,ab}$ , as the best approximation to compute excitonic couplings since it includes contributions from local excitations on monomers in addition to the two interacting states in the dimer supermolecule. Though high accuracy methods are advised to compute excitonic couplings of CBP dimers, good agreement of TD-LC-DFTB with PNO-ADC(2) make it a reasonable option with lower computational scaling.

### 5.4 Electronic polarization due to explicit environment

Having assessed the importance of confinement from the bulk on dimer geometries, the influence of explicit environment molecules on the excited-state properties of CBP dimers is studied. For this purpose a set of molecular clusters, sampled from a CBP slab, are used to explore the effects of polarization due to embedding on excitonic couplings. In accordance with the previous section, the dimers at the centre of the clusters were optimized, *cf.* Sec. 5.1.1.

As a first step, the cluster size was investigated to identify the required number of surrounding molecules. The clusters employed were generated by selecting molecules within different radii around a reference CBP at the centre. The clusters ranged from 5 to 25 CBP molecules in total, from which either the central monomer or dimer was selected as active subsystems. The FDE approach was used to compute the lowest five singlet excitation energies of the central monomer, or dimer, at the LT-SOS-ADC(2)-in-DFT level. For comparison, the monomer and dimer were also treated in absence of environment molecules. The results are shown in Fig. 29a and 29b, where excitation energies are plotted against system size.

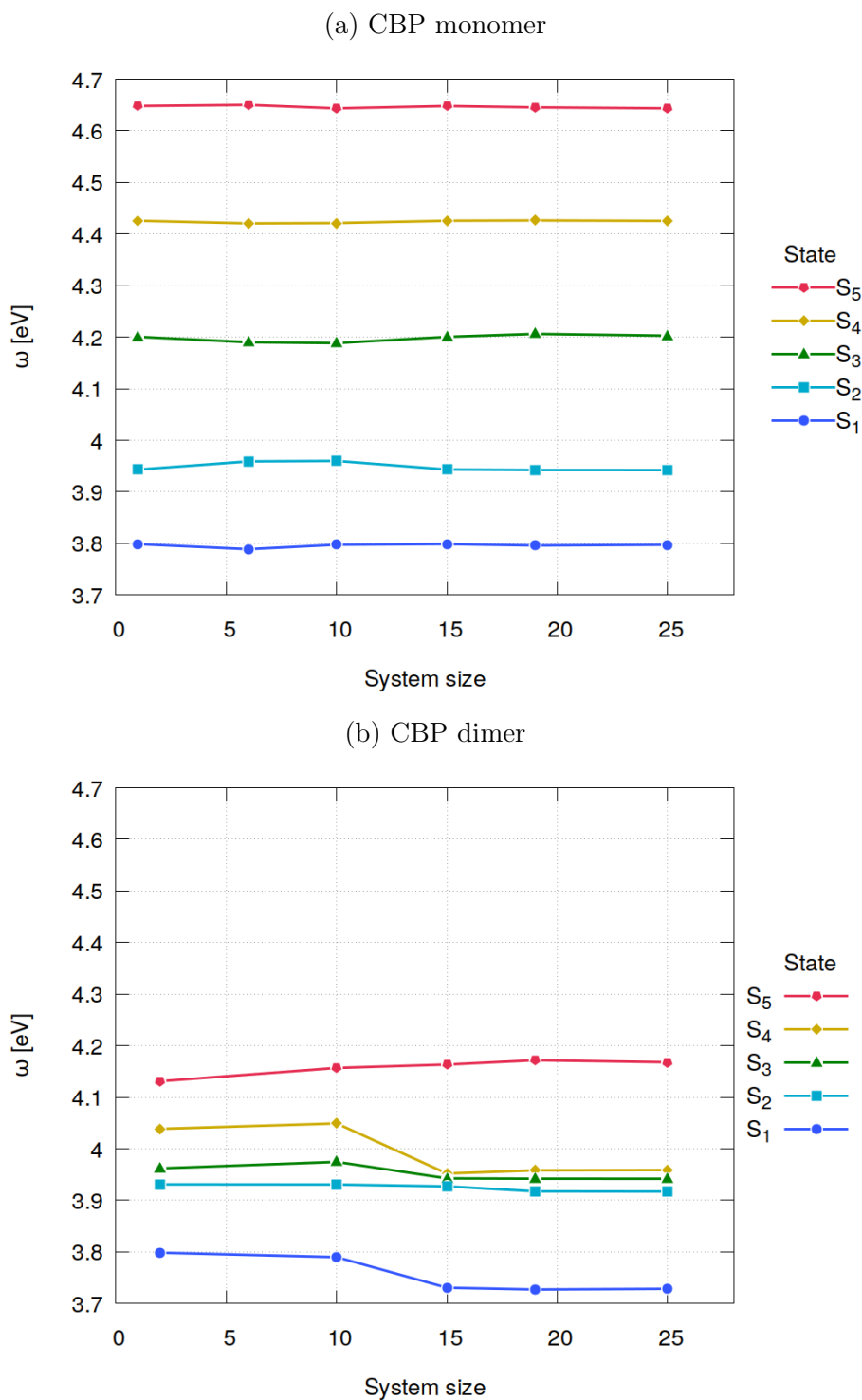


Figure 29: LT-SOS-ADC(2)-in-DFT excitation energies, in eV, with respect to increasing number of molecules around a CBP (a) monomer and (b) dimer. The monomer was surrounded by 5, 9, 14, 18, and 24 molecules; the dimer by 8, 13, 17, and 23 CBPs.

The graph of the monomer active centre, in the upper panel of Fig. 29, shows no significant changes in excitation energies due to polarization of the environment regardless of the system size. The  $S_1$  to  $S_5$  states remain relatively constant at about 3.80, 3.95, 4.20, 4.41, and 4.65 eV, with variations of less than 0.02 eV. In contrast, the plot corresponding to the dimer active subsystem, in the lower panel of Fig. 29, shows a red shift, of about 0.10 eV, in dimer excited state  $S_1$  of cluster sizes of 15 molecules or larger. The  $S_2$  state remains practically unchanged, whereas  $S_3$  is red shifted about 0.05 eV. The other major shift occurs for the  $S_4$  excitation, which is red shifted around 0.10 eV. No further significant shifts are observed up to clusters containing 25 CBP molecules. This suggests that at least 15 molecules are needed to recover polarization effects from the environment around a CBP dimer, possibly forming a “first solvation shell”. Considering these results, and the scaling of the method with system size, the following section is limited to the study of CBP clusters containing 15 molecules in total.

### 5.4.1 Relaxed embedded dimers

Once the minimum size of the embedding system was established, several CBP clusters were extracted from the slab, *cf.* Sec. 5.1. The dimers at the centre were optimized following the procedure described in Section 5.1.1. However, only 3 cluster geometries reached convergence within the allocated time frame.

The clusters A, B, and C, with relaxed DFT dimer geometries at their centre, are displayed in Fig. 30. In general, geometry relaxation allowed the Ph-Ph bond to contract between 0.01 and 0.07 Å, while the CBZ-Ph bonds are increased between 0.03 and 0.08 Å. Relevant bond lengths of the unrelaxed MD and relaxed DFT geometries are included in Appendix A.3. In the following “dimer” will refer only to the molecules highlighted in Fig. 30, *i.e.* without environment CBPs.

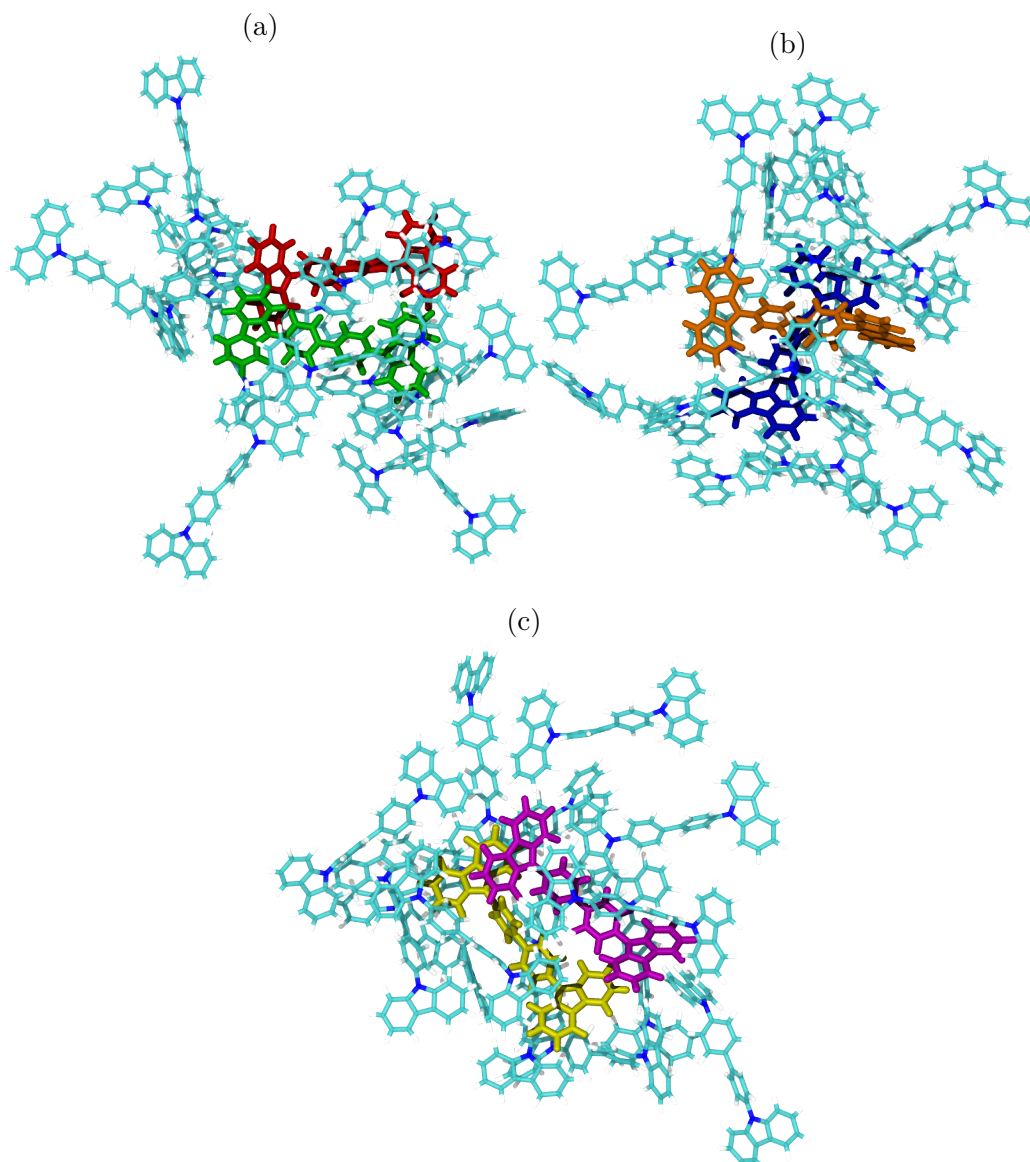


Figure 30: Molecular clusters sampled from a CBP slab. Highlighted dimers at the centre correspond to relaxed DFT geometries. All clusters contain 15 molecules in total.

### 5.4.2 Excitonic couplings and embedding

To assess the effects of polarization due to explicit environment, the excitonic couplings,  $J_{nm,ab}$ , of clusters and dimers were computed. Couplings of clusters A, B, and C were calculated from PNO-ADC(2)-in-DFT excitation energies (*cf.* Sec. 5.1.3). Couplings of dimers were also computed at the TD-LC-DFTB and PNO-ADC(2) levels. The results are displayed in Fig. 31.

The plot corresponding to the excitonic couplings, Fig. 31a, shows that the PNO-ADC(2)  $J_{nm,ab}$  of dimers A, B, and C are about 17, 15, and 15 meV, respectively. On the other hand, TD-LC-DFT couplings are at 28, 39, and 34 meV. As shown in the previous section, the difference of about 10-20 meV falls within the expected variation between these methods when relaxed DFT geometries are employed. The larger differences of in the TD-LC-DFTB couplings of dimers B and C with respect to the PNO-ADC(2) could be caused by unsolved structural issues due optimization within a frozen environment.

Since there were no density embedding schemes for TD-LC-DFTB available to us, only the ADC(2) results were used to assess the polarization effects from the environment. The difference in excitonic coupling,  $\Delta J_{nm,ab}$ , due to embedding is shown in Fig. 31. The graph reveals that inclusion of the environment can lead to positive and negative shifts in excitonic coupling, with respect to the isolated dimer. This suggests that couplings are not only affected by the monomer arrangements due to confinement, but is also influenced by the structure of the surrounding molecules. Therefore, embedding schemes should be considered to recover effects from the structure of the environment relevant for the accurate description of excitonic couplings in CBP. As an outlook, the amount of sampled clusters could substantially be increased to investigate the polarization effects on excitonic couplings averaged over a large number of embedded dimers.

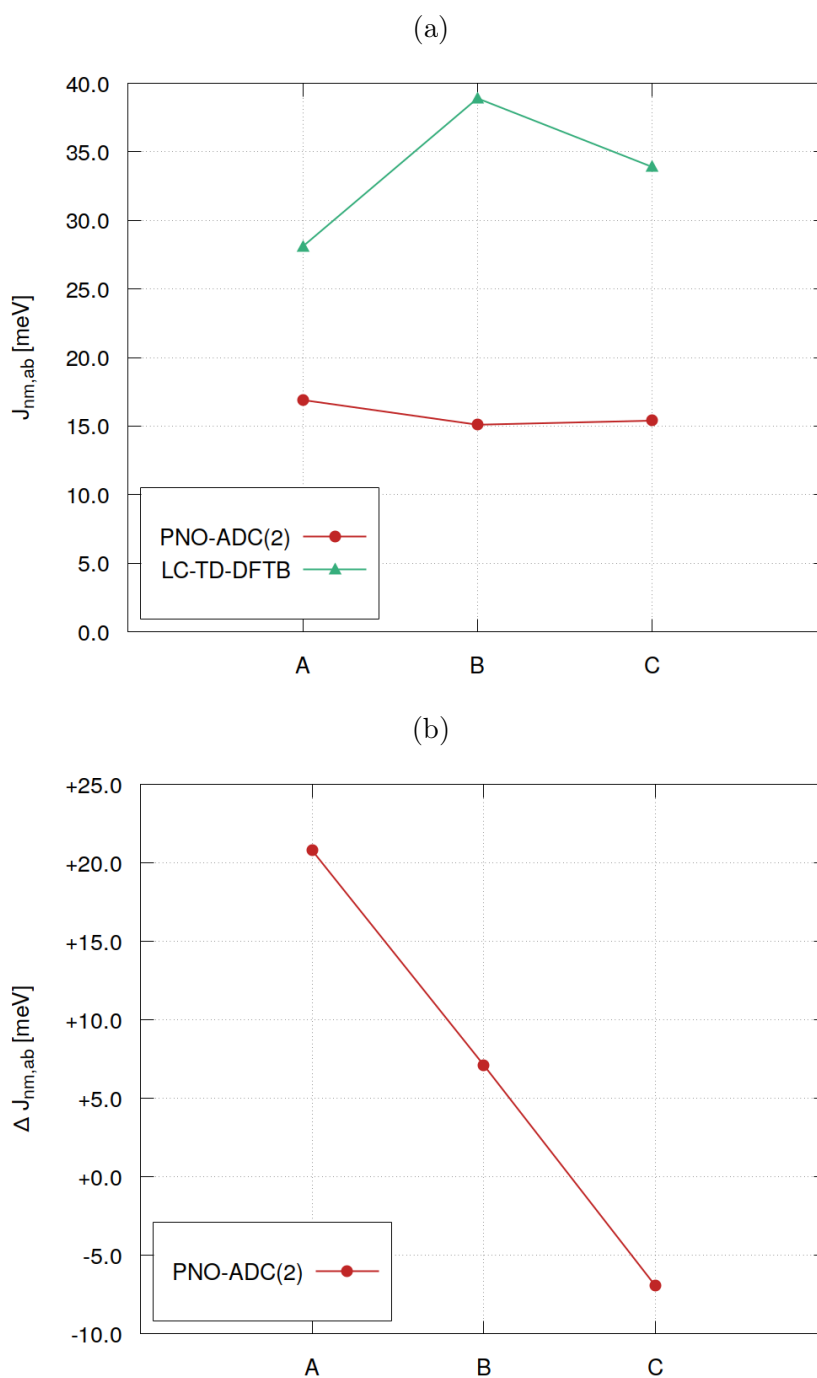


Figure 31: (a) Excitonic couplings of dimers A-C. (b) Shift in coupling,  $\Delta J_{nm,ab}$ , induced by the environment.



## 6 Summary and conclusion

In this thesis, the electronic properties of 4-4'-bis(carbazol-9-yl)biphenyl, CBP, are investigated using efficient and accurate quantum chemical methods. The aim of the present work is to identify key aspects for the accurate description of excited-state properties of CBP, and to help establish a balanced framework of methods to compute them. The research is divided in three parts: the characterization of ground- and excited-state properties of CBP as single molecule in the gas-phase, the assessment of structural effects on excited-state properties in an ensemble picture, and the study of the environmental influence on excited states.

In the ground-state, single-molecule picture, differences in the relative orientation of phenyl and carbazole moieties of minima structures seem to have no significant effect on electronic properties like ionization energies or singlet excitation energies. A comparative study of vertical absorption spectra from TD-DFT and *GW*-BSE calculations confirmed the presence of a charge-transfer type excitation, which is inaccurately described by TD-DFT. In contrast, the *GW*-BSE approach showed correct ordering of excitations, in particular the CT state at about 4.15 eV. Hence the Bethe-Salpeter equation based on the *GW* approximation was the method of choice for excited-state properties of single CBP molecules. The properties of the lowest excited-state structure of CBP were also investigated. It was found that the phenyl-phenyl bond is contracted by almost 0.05 Å upon excitation, which seems to be connected with the observed red shift in the lowest excitation, of about 0.40 eV. Thus, while the relative orientation of torsion angles in local minima has little influence, the bond distance of the biphenyl group has a strong effect on the excitation energy.

The influence of torsional conformation of CBP on absorption and emission spectra was investigated using an ensemble approach based on excited-state calculations of about 1.6 k molecules. The structures, generated from a dihedral angle scan, simulate ground- and excited-state geometries of a CBP molecule with free rotating torsion

angles. The Boltzmann averaged absorption spectra showed that charge–transfer type excitations are considerably affected by changes in the dihedrals. The statistical analysis indicates that the reduction of the CT peaks with increasing temperature is caused by a large spread of oscillator strengths rather than on shifts of the excitation energies. In comparison, it was found that increasing the temperature has a significantly weaker effect in the averaged emission spectra. The data from the free rotating ground- and excited-state geometries shows that there is a strong influence due to changes in the Ph-Ph bond, leading also to an emission red shift of about 0.40 eV.

The effects of different environments on the excited-state properties of CBP dimers were also explored. The investigation of fully-relaxed dimers was used to benchmark methods for dimer excitation energies and excitonic couplings, where PNO-ADC(2) was employed as reference. It was shown that, for excitonic couplings calculated using the two-state model, the best alternative to PNO-ADC(2) is the TD-LC-DFTB method. The study of dimers sampled from an MD-equilibrated slab demonstrated the importance of accurate geometries to compute excitonic couplings. Sampled dimers from simulated thin film structures have geometries that reflect confinement from neighboring molecules within the bulk. However, these structures still need to be refined to correct bond distances, and general distortions to bond angles. The use of relaxed geometries can reduce errors in excitonic couplings by up to 30 meV. Effects on excitonic coupling of polarization due to environment were investigated using dimers embedded within CBP molecular clusters. The positive and negative shifts in excitonic coupling of dimers with similar structures suggest that the structure of the environment is also important for the correct description of said couplings.

One of the main drawbacks in this study stems from the reduced number of clusters used in the investigation of couplings in embedded dimers. The sample size used is not meaningful for a correct picture of the configuration space, which is necessary if the bulk effects of polarization are to be investigated. Thus, one outlook is to increase the amount of extracted clusters to investigate averaging of excited-state properties within the bulk. Furthermore, the study of species that are in a charged-excited state, as a first step towards the investigation of degradation mechanisms caused by the interaction of excitons and polarons, remains the subject of future work.

---

In conclusion, the results presented in this thesis show that accurate description of excited states of CBP requires to go beyond the gas-phase, single-molecule approaches to account for key aspects with strong influence on the properties of the material, like structural variation, confinement from the bulk, and interaction of molecules with their surroundings.



# **A Appendix**

## Supplementary Data for Chapter Five



## A.1 Singlet excitation energies of CBP dimers

### A.1.1 Excitation energies of gas-phase dimers

Table 14: Vertical excitation energies,  $S_n$  ( $n=1, 2, 3, 4, 5$ ), of the five lowest singlet states of the gas-phase optimized CBP systems AS, S, T, and X. Energies were calculated using the CIS(D) method. Values correspond to gas-phase dimers and gas-phase monomers, monomer<sub>I</sub> and monomer<sub>II</sub>. All energy values are given in eV.

	CIS(D)				
	$S_1$	$S_2$	$S_3$	$S_4$	$S_5$
AS monomer <sub>I</sub>	4.293	4.639	4.695	4.698	4.838
AS monomer <sub>II</sub>	4.403	4.460	4.668	4.787	4.865
AS dimer	4.042	4.124	4.369	4.571	4.600
S monomer <sub>I</sub>	4.233	4.475	4.639	4.788	5.069
S monomer <sub>II</sub>	4.177	4.344	4.640	4.936	5.113
S dimer	4.018	4.026	4.119	4.269	4.347
T monomer <sub>I</sub>	4.173	4.519	4.692	4.756	5.103
T monomer <sub>II</sub>	4.187	4.451	4.653	4.913	4.968
T dimer	4.201	4.422	4.495	4.599	4.602
X monomer <sub>I</sub>	4.141	4.145	4.634	5.106	5.113
X monomer <sub>II</sub>	4.216	4.269	4.654	4.968	5.051
X dimer	4.188	4.244	4.445	4.473	4.553

Table 15: Vertical excitation energies,  $S_n$  ( $n=1, 2, 3, 4, 5$ ), of the five lowest singlet states of the gas-phase optimized CBP systems AS, S, T, and X. Energies were calculated using the LT-SOS-ADC(2) method. Values correspond to gas-phase dimers and gas-phase monomers, monomer<sub>I</sub> and monomer<sub>II</sub>. All energy values are given in eV. Oscillator strengths of dimers in parenthesis.

	<b>LT-SOS-ADC(2)</b>				
	$S_1$	$S_2$	$S_3$	$S_4$	$S_5$
AS monomer <sub>I</sub>	4.088	4.095	4.391	4.512	4.598
AS monomer <sub>II</sub>	4.086	4.095	4.415	4.517	4.594
AS dimer	3.980(0)	4.015(177)	4.084(97)	4.090(69)	4.331(1882)
S monomer <sub>I</sub>	4.091	4.101	4.421	4.542	4.574
S monomer <sub>II</sub>	4.093	4.101	4.422	4.547	4.573
S dimer	3.982(0)	3.993(0)	4.030(199)	4.036(30)	4.180(1)
T monomer <sub>I</sub>	4.085	4.099	4.483	4.556	4.574
T monomer <sub>II</sub>	4.088	4.098	4.388	4.491	4.612
T dimer	4.024(41)	4.037(111)	4.061(34)	4.075(81)	4.356(433)
X monomer <sub>I</sub>	4.084	4.090	4.374	4.493	4.610
X monomer <sub>II</sub>	4.084	4.093	4.093	4.510	4.614
X dimer	4.047(75)	4.051(76)	4.088(95)	4.096(70)	4.294(503)

Table 16: Vertical excitation energies,  $S_n$  ( $n=1, 2, 3, 4, 5$ ), of the five lowest singlet states of the gas-phase optimized CBP systems AS, S, T, and X. Energies were calculated using the PNO-ADC(2) method. Values correspond to gas-phase dimers and gas-phase monomers, monomer<sub>I</sub> and monomer<sub>II</sub>. All energy values are given in eV.

	PNO-ADC(2)				
	S <sub>1</sub>	S <sub>2</sub>	S <sub>3</sub>	S <sub>4</sub>	S <sub>5</sub>
AS monomer <sub>I</sub>	3.969	3.987	4.042	4.731	4.738
AS monomer <sub>II</sub>	3.976	3.976	4.058	4.503	4.744
AS dimer	3.890	3.910	4.080	4.306	4.553
S monomer <sub>I</sub>	3.977	3.985	4.079	4.763	4.767
S monomer <sub>II</sub>	3.979	3.980	4.084	4.484	4.491
S dimer	3.791	3.841	3.848	3.890	3.955
T monomer <sub>I</sub>	3.972	3.982	4.136	4.498	4.746
T monomer <sub>II</sub>	3.980	3.989	4.028	4.421	4.743
T dimer	3.918	3.919	3.978	4.177	4.183
X monomer <sub>I</sub>	3.971	3.975	4.011	4.458	4.522
X monomer <sub>II</sub>	3.975	3.977	4.017	4.333	4.751
X dimer					

Table 17: Vertical excitation energies,  $S_n$  ( $n=1, 2, 3, 4, 5$ ), of the five lowest singlet states of the gas-phase optimized CBP systems AS, S, T, and X. Energies were calculated using the *GW*-BSE method. Values correspond to gas-phase dimers and gas-phase monomers, monomer<sub>I</sub> and monomer<sub>II</sub>. All energy values are given in eV. Oscillator strengths in parentheses, expressed as multiples of  $10^{-3}$ .

	<i>GW</i> -BSE				
	$S_1$	$S_2$	$S_3$	$S_4$	$S_5$
AS monomer <sub>I</sub>	3.746(80)	3.758(47)	4.020(1113)	4.212(134)	4.225(150)
AS monomer <sub>II</sub>	3.753(73)	3.769(49)	4.039(1111)	4.219(136)	4.234(149)
AS dimer	3.594(84)	3.597(37)	3.790(1)	3.829(243)	3.940(2091)
S monomer <sub>I</sub>	3.747(117)	3.754(21)	4.046(1148)	4.220(100)	4.223(179)
S monomer <sub>II</sub>	3.748(129)	3.754(8)	4.048(1146)	4.219(109)	4.224(170)
S dimer	3.623(0)	3.631(1)	3.679(145)	3.683(7)	3.787(1)
T monomer <sub>I</sub>	3.760(85)	3.772(41)	4.108(1102)	4.228(101)	4.234(186)
T monomer <sub>II</sub>	3.755(80)	3.767(45)	4.008(1094)	4.219(126)	4.225(161)
T dimer	3.632(58)	3.712(64)	3.728(26)	3.842(68)	3.976(524)
X monomer <sub>I</sub>	3.748(93)	3.756(33)	3.996(1095)	4.217(105)	4.220(178)
X monomer <sub>II</sub>	3.755(119)	3.759(0)	4.011(1079)	4.217(132)	4.225(153)
X dimer	3.639(76)	3.641(40)	3.679(52)	3.682(39)	3.915(421)

Table 18: Vertical excitation energies,  $S_n$  ( $n=1, 2, 3, 4, 5$ ), of the five lowest singlet states of the gas-phase optimized CBP systems AS, S, T, and X. Energies were calculated using the CAM-B3LYP density functional. Values correspond to gas-phase dimers and gas-phase monomers, monomer<sub>I</sub> and monomer<sub>II</sub>. All energy values are given in eV. Oscillator strengths in parentheses, expressed as multiples of  $10^{-3}$ .

	CAM-B3LYP				
	$S_1$	$S_2$	$S_3$	$S_4$	$S_5$
AS monomer <sub>I</sub>	4.185(1183)	4.279(7)	4.285(0)	4.604(0)	4.670(15)
AS monomer <sub>II</sub>	4.199(1173)	4.279(4)	4.286(4)	4.612(1)	4.676(19)
AS dimer	4.142(112)	4.161(2231)	4.233(46)	4.238(55)	4.279(2)
S monomer <sub>I</sub>	4.211(1174)	4.280(0)	4.299(69)	4.658(0)	4.701(12)
S monomer <sub>II</sub>	4.213(1170)	4.282(2)	4.300(68)	4.657(0)	4.703(14)
S dimer	4.038(1)	4.179(24)	4.197(0)	4.219(1795)	4.253(7)
T monomer <sub>I</sub>	4.245(797)	4.277(9)	4.322(395)	4.681(3)	4.711(13)
T monomer <sub>II</sub>	4.168(1152)	4.281(7)	4.287(3)	4.577(0)	4.647(14)
T dimer	4.161(448)	4.217(509)	4.245(9)	4.257(230)	4.270(15)
X monomer <sub>I</sub>	4.161(1157)	4.278(4)	4.280(6)	4.572(1)	4.647(14)
X monomer <sub>II</sub>	4.174(1137)	4.279(2)	4.283(7)	4.571(1)	4.664(20)
X dimer	4.127(570)	4.164(1123)	4.247(15)	4.252(21)	4.287(25)

Table 19: Vertical excitation energies,  $S_n$  ( $n=1, 2, 3, 4, 5$ ), of the five lowest singlet states of the gas-phase optimized CBP systems AS, S, T, and X. Energies were calculated using LC-TD-DFTB. Values correspond to gas-phase dimers and gas-phase monomers, monomer<sub>I</sub> and monomer<sub>II</sub>. All energy values are given in eV. Oscillator strengths in parentheses, expressed as multiples of  $10^{-3}$ .

<b>LC-TD-DFTB</b>					
	$S_1$	$S_2$	$S_3$	$S_4$	$S_5$
AS monomer <sub>I</sub>	3.950(1039)	4.116(1)	4.248(104)	4.473(4)	4.482(16)
AS monomer <sub>II</sub>	3.956(1033)	4.118(1)	4.250(109)	4.475(5)	4.483(15)
AS dimer	3.938(1692)	3.947(419)	4.093(6)	4.120(2)	4.239(209)
S monomer <sub>I</sub>	3.965(1058)	4.119(0)	4.274(166)	4.486(16)	4.489(17)
S monomer <sub>II</sub>	3.966(1056)	4.120(0)	4.275(167)	4.488(13)	4.488(21)
S dimer	3.889(3)	4.006(1703)	4.078(11)	4.150(0)	4.243(0)
T monomer <sub>I</sub>	3.991(954)	4.118(4)	4.293(237)	4.481(13)	4.483(22)
T monomer <sub>II</sub>	3.943(1055)	4.118(1)	4.239(74)	4.444(2)	4.483(18)
T dimer	3.926(364)	3.990(1257)	4.101(27)	4.108(12)	4.232(75)
X monomer <sub>I</sub>	3.940(1062)	4.117(1)	4.239(76)	4.447(1)	4.483(18)
X monomer <sub>II</sub>	3.949(1037)	4.119(1)	4.241(78)	4.444(0)	4.484(18)
X dimer	3.924(646)	3.946(1138)	4.098(3)	4.126(3)	4.227(14)

## A.1.2 Excitation energies of sampled dimers: unrelaxed MD geometries

Table 20: Vertical excitation energies,  $S_n$  ( $n=1, 2, 3, 4, 5$ ), of the five lowest singlet states of CBP sampled systems D, E, F, G, and H. Energies were calculated for the unrelaxed MD geometries using the PNO-ADC(2) method. Values correspond to dimers and monomers, monomer<sub>I</sub> and monomer<sub>II</sub>. All energy values are given in eV.

	PNO-ADC(2)				
	$S_1$	$S_2$	$S_3$	$S_4$	$S_5$
D monomer <sub>I</sub>	3.744	3.856	3.879	4.173	4.228
D monomer <sub>II</sub>	3.748	3.815	3.911	4.075	4.210
D dimer	3.674	3.713	3.759	3.800	3.817
E monomer <sub>I</sub>	3.762	3.815	3.934	4.272	4.707
E monomer <sub>II</sub>	3.894	4.023	4.027	4.134	4.585
E dimer	3.675	3.759	3.866	3.891	4.021
F monomer <sub>I</sub>	3.909	3.977	3.982	4.196	4.826
F monomer <sub>II</sub>	3.830	3.885	4.020	4.204	4.666
F dimer	3.708	3.765	3.769	3.818	3.877
G monomer <sub>I</sub>	3.732	3.885	3.966	4.230	4.750
G monomer <sub>II</sub>	3.705	3.782	4.013	4.100	4.161
G dimer	3.468	3.621	3.732	3.881	3.881
H monomer <sub>I</sub>	3.743	3.771	3.974	4.253	4.615
H monomer <sub>II</sub>	3.825	3.864	3.961	4.158	4.734
H dimer	3.655	3.658	3.732	3.776	4.050

Table 21: Vertical excitation energies,  $S_n$  ( $n=1, 2, 3, 4, 5$ ), of the five lowest singlet states of CBP sampled systems D, E, F, G, and H. Energies were calculated for the unrelaxed MD geometries using the  $GW$ -BSE method. Values correspond to dimers and monomers, monomer $_I$  and monomer $_{II}$ . All energy values are given in eV. Oscillator strengths in parentheses, expressed as multiples of  $10^{-3}$ .

	$GW$ -BSE				
	$S_1$	$S_2$	$S_3$	$S_4$	$S_5$
D monomer $_I$	3.550(25)	3.646(39)	3.893(750)	4.106(179)	4.106(76)
D monomer $_{II}$	3.567(28)	3.633(8)	3.705(1199)	3.934(14)	4.132(82)
D dimer	3.413(21)	3.513(32)	3.573(23)	3.628(112)	3.644(139)
E monomer $_I$	3.669(60)	3.701(88)	3.768(796)	4.153(51)	4.196(10)
E monomer $_{II}$	3.811(24)	3.845(43)	4.082(63)	4.270(6)	4.296(110)
E dimer	3.632(70)	3.636(24)	3.667(46)	3.741(404)	3.822(102)
F monomer $_I$	3.697(28)	3.774(22)	3.996(873)	4.159(78)	4.232(97)
F monomer $_{II}$	3.644(25)	3.730(46)	4.042(800)	4.230(33)	4.251(82)
F dimer	3.556(11)	3.666(6)	3.712(25)	3.718(8)	3.815(112)
G monomer $_I$	3.639(58)	3.696(97)	3.764(766)	4.106(50)	4.193(87)
G monomer $_{II}$	3.548(81)	3.642(1012)	3.723(180)	3.896(21)	4.057(102)
G dimer	3.509(88)	3.524(6)	3.525(133)	3.613(625)	3.656(178)
H monomer $_I$	3.527(39)	3.724(1)	3.752(1132)	4.059(172)	4.099(6)
H monomer $_{II}$	3.599(7)	3.665(1)	3.814(1068)	4.017(61)	4.163(63)
H dimer	3.494(9)	3.564(26)	3.613(158)	3.623(30)	3.663(41)

Table 22: Vertical excitation energies,  $S_n$  ( $n=1, 2, 3, 4, 5$ ), of the five lowest singlet states of CBP sampled systems D, E, F, G, and H. Energies were calculated for the unrelaxed MD geometries at the TD-DFT level, using the CAM-B3LYP functional. Values correspond to dimers and monomers, monomer<sub>I</sub> and monomer<sub>II</sub>. All energy values are given in eV. Oscillator strengths in parentheses, expressed as multiples of  $10^{-3}$ .

<b>CAM-B3LYP</b>					
	$S_1$	$S_2$	$S_3$	$S_4$	$S_5$
D monomer <sub>I</sub>	4.057(426)	4.086(422)	4.162(13)	4.432(59)	4.482(47)
D monomer <sub>II</sub>	3.907(1095)	4.118(39)	4.216(60)	4.320(13)	4.460(1)
D dimer	3.883(328)	3.990(1166)	4.086(89)	4.112(53)	4.151(1)
E monomer <sub>I</sub>	3.892(844)	4.113(35)	4.240(36)	4.336(11)	4.501(37)
E monomer <sub>II</sub>	4.167(379)	4.238(230)	4.322(15)	4.387(7)	4.682(88)
E dimer	3.863(526)	4.084(58)	4.182(182)	4.207(58)	4.235(341)
F monomer <sub>I</sub>	4.155(681)	4.200(188)	4.323(67)	4.469(2)	4.504(15)
F monomer <sub>II</sub>	4.129(42)	4.159(316)	4.179(497)	4.419(3)	4.637(4)
F dimer	4.006(80)	4.052(34)	4.112(52)	4.139(420)	4.166(639)
G monomer <sub>I</sub>	3.904(766)	4.179(42)	4.241(127)	4.401(84)	4.482(5)
G monomer <sub>II</sub>	3.831(1135)	4.072(47)	4.273(54)	4.345(24)	4.413(1)
G dimer	3.738(71)	3.831(1422)	4.048(32)	4.179(14)	4.224(251)
H monomer <sub>I</sub>	3.916(998)	4.073(78)	4.267(37)	4.355(16)	4.485(10)
H monomer <sub>II</sub>	3.996(871)	4.119(166)	4.242(61)	4.392(28)	4.527(57)
H dimer	3.849(187)	3.957(12227)	4.023(87)	4.107(219)	4.199(54)

Table 23: Vertical excitation energies,  $S_n$  ( $n=1, 2, 3, 4, 5$ ), of the five lowest singlet states of CBP sampled systems D, E, F, G, and H. Energies were calculated for the unrelaxed MD geometries at the LC-TD-DFTB level. Values correspond to dimers and monomers, monomer<sub>I</sub> and monomer<sub>II</sub>. All energy values are given in eV. Oscillator strengths in parentheses, expressed as multiples of  $10^{-3}$ .

<b>LC-TD-DFTB</b>					
	$S_1$	$S_2$	$S_3$	$S_4$	$S_5$
D monomer <sub>I</sub>	3.887(709)	3.972(3)	4.033(58)	4.195(15)	4.411(120)
D monomer <sub>II</sub>	3.780(1109)	4.014(43)	4.140(14)	4.281(6)	4.371(26)
D dimer	3.760(440)	3.859(1136)	3.977(26)	4.018(40)	4.025(17)
E monomer <sub>I</sub>	3.689(792)	4.042(27)	4.078(4)	4.141(35)	4.452(5)
E monomer <sub>II</sub>	3.895(577)	4.048(0)	4.097(10)	4.204(39)	4.419(6)
E dimer	3.678(513)	3.909(714)	4.017(9)	4.053(13)	4.081(36)
F monomer <sub>I</sub>	3.958(748)	4.089(19)	4.171(10)	4.183(19)	4.275(85)
F monomer <sub>II</sub>	3.907(623)	4.023(34)	4.100(129)	4.200(20)	4.349(17)
F dimer	3.832(114)	3.947(978)	4.023(68)	4.050(7)	4.075(13)
G monomer <sub>I</sub>	3.664(795)	4.013(83)	4.148(28)	4.200(33)	4.388(18)
G monomer <sub>II</sub>	3.651(1149)	3.934(16)	4.093(20)	4.191(13)	4.271(17)
G dimer	3.571(116)	3.667(1547)	3.922(25)	3.981(102)	4.098(7)
H monomer <sub>I</sub>	3.706(1029)	3.929(16)	4.087(7)	4.213(0)	4.371(75)
H monomer <sub>II</sub>	3.845(953)	4.028(124)	4.154(13)	4.191(13)	4.358(76)
H dimer	3.665(405)	3.816(1285)	3.924(20)	4.029(79)	4.066(10)

## A.1.3 Excitation energies of sampled dimers: relaxed DFT geometries

Table 24: Vertical excitation energies,  $S_n$  ( $n=1, 2, 3, 4, 5$ ), of the five lowest singlet states of CBP sampled systems D, E, F, G, and H. Energies were calculated for the relaxed DFT geometries using the PNO-ADC(2) method. Values correspond to dimers and monomers, monomer<sub>I</sub> and monomer<sub>II</sub>. All energy values are given in eV.

	PNO-ADC(2)				
	$S_1$	$S_2$	$S_3$	$S_4$	$S_5$
D monomer <sub>I</sub>	3.834	3.913	3.927	4.249	4.673
D monomer <sub>II</sub>	3.872	3.914	3.925	4.657	4.665
D-dim	3.640	3.795	3.819	3.845	3.882
E monomer <sub>I</sub>	3.879	3.905	3.950	4.671	4.673
E monomer <sub>II</sub>	3.910	3.920	3.981	4.675	4.672
E-dim	3.796	3.818	3.833	3.885	3.901
F monomer <sub>I</sub>	3.913	3.926	4.072	4.485	4.470
F monomer <sub>II</sub>	3.898	3.911	3.951	4.350	4.668
F-dim	3.688	3.778	3.803	3.836	3.861
G monomer <sub>I</sub>	3.857	3.897	3.938	4.656	4.664
G monomer <sub>II</sub>	3.908	3.931	3.983	4.661	4.669
G-dim	3.692	3.811	3.853	3.865	3.879
H monomer <sub>I</sub>	3.902	3.913	3.938	4.308	4.186
H monomer <sub>II</sub>	3.909	3.921	3.945	4.659	4.670
H-dim	3.704	3.816	3.838	3.841	3.895

Table 25: Vertical excitation energies,  $S_n$  ( $n=1, 2, 3, 4, 5$ ), of the five lowest singlet states of CBP sampled systems D, E, F, G, and H. Energies were calculated for the relaxed DFT geometries using the *GW*-BSE method. Values correspond to dimers and monomers, monomer<sub>I</sub> and monomer<sub>II</sub>. All energy values are given in eV. Oscillator strengths in parentheses, expressed as multiples of  $10^{-3}$ .

	<i>GW</i> -BSE				
	$S_1$	$S_2$	$S_3$	$S_4$	$S_5$
D monomer <sub>I</sub>	3.642(207)	3.655(28)	3.810(1150)	4.089(18)	4.107(207)
D monomer <sub>II</sub>	3.676(135)	3.683(18)	3.875(1070)	4.125(14)	4.132(272)
D-dim	3.594(5)	3.620(173)	3.653(143)	3.681(122)	3.699(3)
E monomer <sub>I</sub>	3.650(193)	3.658(3)	3.878(1191)	4.109(113)	4.111(174)
E monomer <sub>II</sub>	3.691(73)	3.708(59)	3.968(1048)	4.138(130)	4.159(159)
E-dim	3.537(62)	3.581(79)	3.633(64)	3.659(27)	3.799(156)
F monomer <sub>I</sub>	3.732(87)	3.737(14)	4.086(957)	4.180(100)	4.189(194)
F monomer <sub>II</sub>	3.685(127)	3.690(4)	3.930(1069)	4.140(23)	4.145(2620)
F-dim	3.599(3)	3.645(4)	3.680(175)	3.685(6)	3.738(347)
G monomer <sub>I</sub>	3.643(159)	3.654(35)	3.862(1067)	4.104(85)	4.113(194)
G monomer <sub>II</sub>	3.697(74)	3.721(66)	3.966(1073)	4.141(125)	4.165(170)
G-dim	3.578(54)	3.623(60)	3.648(45)	3.703(200)	3.781(215)
H monomer <sub>I</sub>	3.698(93)	3.711(47)	3.916(1020)	4.143(145)	4.161(119)
H monomer <sub>II</sub>	3.689(86)	3.699(42)	3.923(1074)	4.140(132)	4.148(150)
H-dim	3.625(43)	3.649(54)	3.680(3)	3.729(185)	3.749(77)

Table 26: Vertical excitation energies,  $S_n$  ( $n=1, 2, 3, 4, 5$ ), of the five lowest singlet states of CBP sampled systems D, E, F, G, and H. Energies were calculated for the relaxed DFT geometries at the TD-DFT level, using the CAM-B3LYP functional. Values correspond to dimers and monomers, monomer<sub>I</sub> and monomer<sub>II</sub>. All energy values are given in eV. Oscillator strengths in parentheses, expressed as multiples of  $10^{-3}$ .

<b>CAM-B3LYP</b>					
	$S_1$	$S_2$	$S_3$	$S_4$	$S_5$
D monomer <sub>I</sub>	3.995(1285)	4.216(3)	4.222(9)	4.496(5)	4.550(4)
D monomer <sub>II</sub>	4.046(1146)	4.220(16)	4.226(8)	4.496(0)	4.545(2)
D-dim	3.879(369)	4.054(1614)	4.167(1)	4.193(8)	4.203(14)
E monomer <sub>I</sub>	4.065(1342)	4.210(1)	4.225(6)	4.559(6)	4.606(4)
E monomer <sub>II</sub>	4.127(1111)	4.225(17)	4.231(4)	4.549(4)	4.606(2)
E-dim	4.015(411)	4.122(1502)	4.152(48)	4.175(35)	4.186(1)
F monomer <sub>I</sub>	4.216(511)	4.234(78)	4.259(432)	4.576(0)	4.653(193)
F monomer <sub>II</sub>	4.103(1148)	4.217(2)	4.227(7)	4.541(3)	4.585(4)
F-dim	3.968(467)	4.125(34)	4.169(226)	4.201(10)	4.222(73)
G monomer <sub>I</sub>	4.043(1213)	4.201(14)	4.214(1)	4.535(4)	4.570(19)
G monomer <sub>II</sub>	4.123(1148)	4.230(14)	4.240(5)	4.542(2)	4.605(10)
G-dim	3.950(451)	4.104(1279)	4.173(41)	4.191(15)	4.206(52)
H monomer <sub>I</sub>	4.069(1067)	4.225(11)	4.239(20)	4.446(1)	4.547(12)
H monomer <sub>II</sub>	4.093(1140)	4.224(9)	4.227(7)	4.527(2)	4.586(10)
H-dim	3.962(177)	4.090(1513)	4.165(100)	4.193(5)	4.213(30)

Table 27: Vertical excitation energies,  $S_n$  ( $n=1, 2, 3, 4, 5$ ), of the five lowest singlet states of CBP sampled systems D, E, F, G, and H. Energies were calculated for the relaxed DFT geometries at the LC-TD-DFTB level. Values correspond to dimers and monomers, monomer<sub>I</sub> and monomer<sub>II</sub>. All energy values are given in eV. Oscillator strengths in parentheses, expressed as multiples of  $10^{-3}$ .

	<b>LC-TD-DFTB</b>				
	$S_1$	$S_2$	$S_3$	$S_4$	$S_5$
D monomer <sub>I</sub>	3.797(1174)	4.025(4)	4.150(67)	4.379(41)	4.380(3)
D monomer <sub>II</sub>	3.847(1074)	4.037(0)	4.154(58)	4.352(1)	4.387(13)
D-dim	3.731(220)	3.859(1691)	4.003(3)	4.048(0)	4.139(8)
E monomer <sub>I</sub>	3.843(1173)	4.024(1)	4.180(153)	4.376(22)	4.377(22)
E monomer <sub>II</sub>	3.888(976)	4.040(9)	4.174(116)	4.382(23)	4.383(8)
E-dim	3.813(345)	3.890(1397)	4.009(36)	4.025(0)	4.158(33)
F monomer <sub>I</sub>	3.963(754)	4.052(5)	4.223(232)	4.392(8)	4.393(28)
F monomer <sub>II</sub>	3.877(1023)	4.040(5)	4.170(104)	4.388(24)	4.391(11)
F-dim	3.811(363)	3.963(1081)	4.010(2)	4.067(4)	4.158(4)
G monomer <sub>I</sub>	3.829(1052)	4.018(23)	4.164(119)	4.363(22)	4.379(20)
G monomer <sub>II</sub>	3.885(999)	4.044(10)	4.174(110)	4.377(11)	4.384(33)
G-dim	3.776(344)	3.889(1279)	4.005(20)	4.038(46)	4.159(55)
H monomer <sub>I</sub>	3.854(989)	4.038(2)	4.143(35)	4.286(7)	4.390(21)
H monomer <sub>II</sub>	3.882(1024)	4.039(1)	4.171(103)	4.363(2)	4.389(20)
H-dim	3.785(83)	3.885(1609)	4.008(11)	4.053(1)	4.138(1)

## A.1.4 Excitation energies of molecular clusters

Table 28: Vertical excitation energies,  $S_n$  ( $n=1, 2, 3, 4, 5$ ), of the five lowest singlet states of the sampled clusters A, B, and C. Excitations of clusters were computed with the FDE approach at the CIS(D)-in-DFT level. Energies of dimers and monomers, monomer<sub>I</sub> and monomer<sub>II</sub>, were obtained using the CIS(D) method. All energies are given in eV.

		CIS(D)				
		$S_1$	$S_2$	$S_3$	$S_4$	$S_5$
<b>A</b>	monomer <sub>I</sub>	4.099	4.107	4.630	5.024	5.035
	monomer <sub>II</sub>	4.099	4.103	4.632	5.031	5.042
	dimer	4.070	4.079	4.094	4.154	4.539
	cluster	4.042	4.086	4.126	4.342	4.562
<b>B</b>	monomer <sub>I</sub>	4.116	4.125	4.620	5.012	5.012
	monomer <sub>II</sub>	4.128	4.140	4.949	5.002	5.056
	dimer	4.079	4.114	4.121	4.129	4.438
	cluster	4.107	4.117	4.122	4.408	4.458
<b>C</b>	monomer <sub>I</sub>	4.084	4.105	4.418	5.045	5.049
	monomer <sub>II</sub>	4.083	4.118	4.680	5.039	5.047
	dimer	4.098	4.118	4.156	4.335	4.345
	cluster	4.073	4.139	4.357	4.370	4.530

Table 29: Vertical excitation energies,  $S_n$  ( $n=1, 2, 3, 4, 5$ ), of the five lowest singlet states of the sampled clusters A, B, and C. Excitations of the molecular clusters were computed with the FDE approach at the LT-SOS-ADC(2)-in-DFT level. Energies of dimers and monomers, monomer<sub>I</sub> and monomer<sub>II</sub>, were obtained using the LT-SOS-ADC(2) method. All energies are given in eV.

		<b>LT-SOS-ADC(2)</b>				
		$S_1$	$S_2$	$S_3$	$S_4$	$S_5$
<b>A</b>	monomer <sub>I</sub>	4.004	4.019	4.368	4.464	4.507
	monomer <sub>II</sub>	4.013	4.025	4.374	4.457	4.509
	dimer	3.971	3.994	4.001	4.014	4.297
	cluster	3.941	3.985	3.998	4.001	4.319
<b>B</b>	monomer <sub>I</sub>	4.018	4.027	4.292	4.362	4.570
	monomer <sub>II</sub>	4.007	4.011	4.540	4.566	4.602
	dimer	3.987	4.005	4.016	4.025	4.203
	cluster	3.984	3.987	4.005	4.017	4.265
<b>C</b>	monomer <sub>I</sub>	4.006	4.028	4.186	4.306	4.597
	monomer <sub>II</sub>	4.014	4.044	4.383	4.475	4.536
	dimer	3.964	4.000	4.019	4.031	4.118
	cluster	3.943	3.982	4.007	4.038	4.145

Table 30: Vertical excitation energies,  $S_n$  ( $n=1, 2, 3, 4, 5$ ), of the five lowest singlet states of the sampled clusters A, B, and C. Excitations of the molecular clusters were computed with the FDE approach at the PNO-ADC(2)-in-DFT level. Energies of dimers and monomers, monomer<sub>I</sub> and monomer<sub>II</sub>, were obtained using the PNO-ADC(2) method. All energies are given in eV.

		PNO-ADC(2)				
		$S_1$	$S_2$	$S_3$	$S_4$	$S_5$
<b>A</b>	monomer <sub>I</sub>	3.911	3.915	4.005	4.421	4.461
	monomer <sub>II</sub>	3.917	3.926	4.034	4.473	4.473
	dimer	3.846	3.880	3.916	3.925	3.987
	cluster	3.989	4.063	4.088	4.092	4.291
<b>B</b>	monomer <sub>I</sub>	3.903	3.942	3.943	4.639	4.646
	monomer <sub>II</sub>	3.902	3.913	4.414	4.656	4.666
	dimer	3.865	3.895	3.909	3.942	3.954
	cluster	4.043	4.088	4.093	4.118	4.836
<b>C</b>	monomer <sub>I</sub>	3.824	3.923	3.933	4.659	4.660
	monomer <sub>II</sub>	3.910	3.936	4.018	4.336	4.656
	dimer	3.757	3.848	3.891	3.912	3.919
	cluster	3.928	4.015	4.021	4.083	4.113

Table 31: Vertical excitation energies,  $S_n$  ( $n=1, 2, 3, 4, 5$ ), of the five lowest singlet states of the dimers from sampled clusters A, B, and C. Energies of dimers and monomers, monomer<sub>I</sub> and monomer<sub>II</sub>, were obtained using the PBE0/*GW*-BSE method. All energies are given in eV. Oscillator strengths in parentheses, expressed as multiples of  $10^{-3}$ .

		<i>GW</i> -BSE				
		$S_1$	$S_2$	$S_3$	$S_4$	$S_5$
<b>A</b>	monomer <sub>I</sub>	3.694(112)	3.704(25)	3.991(1036)	4.149(72)	4.151(208)
	monomer <sub>II</sub>	3.698(93)	3.709(43)	4.002(1091)	4.133(142)	4.151(149)
	dimer	3.652(70)	3.673(54)	3.730(44)	3.769(69)	3.897(205)
<b>B</b>	monomer <sub>I</sub>	3.713(81)	3.740(69)	3.942(951)	4.143(149)	4.173(134)
	monomer <sub>II</sub>	3.831(93)	3.835(5)	4.290(77)	4.296(209)	4.427(294)
	dimer	3.599(49)	3.614(62)	3.619(34)	3.696(70)	3.871(572)
<b>C</b>	monomer <sub>I</sub>	3.652(239)	3.665(20)	3.802(1040)	4.087(8)	4.101(263)
	monomer <sub>II</sub>	3.714(69)	3.731(46)	4.008(1018)	4.155(64)	4.159(220)
	dimer	3.592(58)	3.603(69)	3.647(10)	3.666(167)	3.736(272)

Table 32: Vertical excitation energies,  $S_n$  ( $n=1, 2, 3, 4, 5$ ), of the five lowest singlet states of the dimers from sampled clusters A, B, and C. Energies of dimers and monomers, monomer<sub>I</sub> and monomer<sub>II</sub>, were obtained using the CAM-B3LYP functional. All energies are given in eV. Oscillator strengths in parentheses, expressed as multiples of  $10^{-3}$ .

CAM-B3LYP						
		$S_1$	$S_2$	$S_3$	$S_4$	$S_5$
<b>A</b>	monomer <sub>I</sub>	4.147(1072)	4.222(25)	4.235(43)	4.563(3)	4.640(27)
	monomer <sub>II</sub>	4.157(1089)	4.231(44)	4.245(51)	4.572(1)	4.642(91)
	dimer	4.097(133)	4.161(1319)	4.209(260)	4.220(133)	4.226(47)
<b>B</b>	monomer <sub>I</sub>	4.082(1016)	4.237(3)	4.254(23)	4.404(2)	4.573(17)
	monomer <sub>II</sub>	4.207(128)	4.215(23)	4.587(703)	4.644(80)	4.655(236)
	dimer	4.035(723)	4.197(96)	4.209(46)	4.245(21)	4.256(33)
<b>C</b>	monomer <sub>I</sub>	3.983(1233)	4.224(7)	4.234(13)	4.500(0)	4.530(13)
	monomer <sub>II</sub>	4.170(1078)	4.228(12)	4.256(3)	4.563(3)	4.642(48)
	dimer	3.941(624)	4.127(1357)	4.183(16)	4.220(5)	4.236(16)

Table 33: Vertical excitation energies,  $S_n$  ( $n=1, 2, 3, 4, 5$ ), of the five lowest singlet states of the dimers from sampled clusters A, B, and C. Energies of dimers and monomers, monomer<sub>I</sub> and monomer<sub>II</sub>, were obtained using LC-TD-DFT. All energies are given in eV. Oscillator strengths in parentheses, expressed as multiples of  $10^{-3}$ .

		<b>LC-TD-DFTB</b>				
		$S_1$	$S_2$	$S_3$	$S_4$	$S_5$
<b>A</b>	monomer <sub>I</sub>	3.893(935)	4.033(8)	4.180(150)	4.373(24)	4.381(13)
	monomer <sub>II</sub>	3.887(973)	4.036(7)	4.180(149)	4.368(22)	4.379(24)
	dimer	3.851(51)	3.907(1605)	4.026(33)	4.039(4)	4.168(8)
<b>B</b>	monomer <sub>I</sub>	3.859(906)	4.043(13)	4.134(12)	4.218(41)	4.375(26)
	monomer <sub>II</sub>	4.004(395)	4.036(4)	4.379(19)	4.381(22)	4.466(559)
	dimer	3.841(748)	4.005(379)	4.026(5)	4.046(7)	4.131(0)
<b>C</b>	monomer <sub>I</sub>	3.795(1144)	4.030(18)	4.145(52)	4.368(36)	4.374(9)
	monomer <sub>II</sub>	3.917(914)	4.056(21)	4.184(128)	4.379(25)	4.394(1)
	dimer	3.765(530)	3.905(1314)	4.018(13)	4.059(16)	4.139(22)

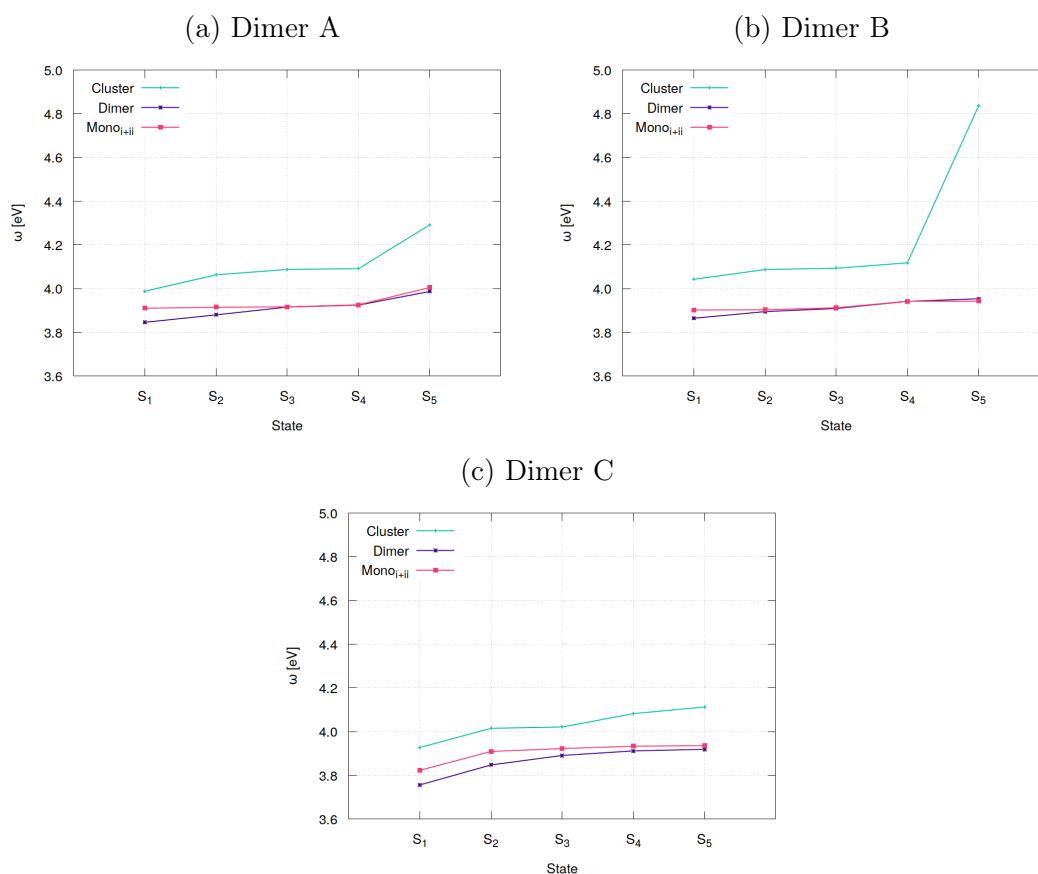


Figure 32: PNO-ADC(2) singlet vertical excitation energies of dimers A, B, and C. Plots in green refer to the embedded dimer computed at the PNO-ADC(2) level within the FDE framework. Dimer plots, in blue, refer to the dimer in absence of surrounding molecules. Mono<sub>i+ii</sub>, in pink, correspond to the combined and re-ordered excitation energies of the monomers, computed individually in the gas-phase.



## A.2 Excitonic couplings of CBP dimers

### A.2.1 Excitonic couplings of sampled dimers: comparison of MD and DFT geometries

Table 34: Excitonic couplings, in meV, computed for the unrelaxed MD, and relaxed DFT geometries of dimers D-H. Excitation energies are given in Appendix A.1.2 and A.1.3.

Dimer	<i>GW</i> -BSE				CAM-B3LYP			
	MD		DFT		MD		DFT	
	$J_{nm}$	$J_{nm,ab}$	$J_{nm}$	$J_{nm,ab}$	$J_{nm}$	$J_{nm,ab}$	$J_{nm}$	$J_{nm,ab}$
<b>D</b>	50	49	13	12	54	*	88	83
<b>E</b>	2	*	22	22	110	*	43	44
<b>F</b>	55	48	23	23	23	19	54	55
<b>G</b>	7	*	23	22	46	28	65	65
<b>H</b>	35	*	12	11	54	36	63	62

\*  $\Delta\omega_{nm} < \Delta\omega_{ab}$  in Eq. (88).

## A.2.2 Excitonic couplings of dimers at the centre of CBP clusters with and without environment

Table 35: PNO-ADC(2) and TD-LC-DFTB excitonic couplings,  $J_{nm,ab}$  in meV of dimers A, B, and C. PNO-ADC(2) couplings of the clusters are also included. Corresponding excitation energies are given in Appendix A.1.4.

		TD-LC-DFTB	PNO-ADC(2)
<b>A</b>	dimer	28	17
	cluster	-	37
<b>B</b>	dimer	39	15
	cluster	-	22
<b>C</b>	dimer	34	15
	cluster	-	8

Table 36: *GW*-BSE and TD-DFT excitonic couplings computed for dimers A, B and C. Couplings were calculated with the non-symmetric,  $J_{nm,ab}$ , dimer formula (Eq. 88). Values are given in meV. Excitation energies are given in Appendix section A.1.4.

		$J_{nm,ab}$ [meV]	
		GW-BSE	CAM-B3LYP
<b>Cluster A</b>	dimer	10	31
<b>Cluster B</b>	dimer	0*	52
<b>Cluster C</b>	dimer	0*	0*

\*  $\Delta E_{mn} < \Delta E_{ab}$  in Eq. 88.

### A.3 Structural parameters of unrelaxed MD and relaxed DFT geometries of sampled dimers

Table 37: Bond lengths, CBZ-Ph, Ph-Ph, and Ph-CBZ, of unrelaxed MD and relaxed DFT geometries of the dimers at the centre of clusters A, B, and C sampled from a CBP slab. Details on the geometry optimization are given in Section 5.1.1. Reference distances obtained from gas-phase geometry optimizations (Section 3.2):  $r_{\text{cbz-ph}}=r_{\text{ph-cbz}}=1.41$ ,  $r_{\text{ph-ph}}=1.47$ . Distances are given in Å.

		monomer <sub>I</sub>			monomer <sub>II</sub>		
		CBZ-Ph	Ph-Ph	Ph-CBZ	CBZ-Ph	Ph-Ph	Ph-CBZ
dimer A	MD	1.36	1.47	1.39	1.37	1.55	1.37
	DFT	1.42	1.48	1.42	1.42	1.48	1.42
dimer B	MD	1.38	1.51	1.35	1.37	1.50	1.34
	DFT	1.43	1.49	1.42	1.42	1.49	1.42
dimer C	MD	1.38	1.50	1.37	1.39	1.50	1.35
	DFT	1.42	1.48	1.42	1.42	1.48	1.42

Table 38: Main torsion angles, in degrees, and bond distances, in Å, of the unrelaxed MD and relaxed DFT dimer D-H. Parameters are given for each monomer *i* and *ii*. Reference parameters taken from the global minimum R<sub>1</sub> (*cf.* Sec. 3.2): r 1-2=r 3-4=1.41Å, r1-2=1.47Å; Dihedral angles 1-2=3-4=-53.9, 2-3=+36.4

Dimer	monomer I						monomer II										
	1-2	2-3	3-4	1-2	2-3	3-4	Dih. ang. <sup>a</sup>	Bond dist. <sup>b</sup>	CBZ ang. <sup>c</sup>	1-2	2-3	3-4	Dih. ang. <sup>a</sup>	Bond dist. <sup>b</sup>	CBZ ang. <sup>c</sup>		
<b>D</b>	MD	-50.3	3.6	68.5	1.39	1.48	1.39	174.4	161.3	46.9	11.4	-48.3	1.35	1.55	1.35	176.4	176.3
	DFT	-49.7	24.3	44.9	1.41	1.46	1.41	173.2	175.8	52.1	26.2	-53.9	1.42	1.47	1.42	178.9	177.3
<b>E</b>	MD	-82.5	-25.6	-57.0	1.34	1.52	1.37	177.4	159.0	106.1	-32.0	49.3	1.36	1.52	1.33	165.5	158.2
	DFT	-37.4	-40.9	-41.0	1.41	1.46	1.41	176.5	175.6	-57.6	139.3	47.8	1.42	1.46	1.41	177.0	177.9
<b>F</b>	MD	49.3	22.9	79.8	1.38	1.49	1.39	176.6	164.7	-49.5	-29.0	66.4	1.42	1.55	1.36	175.1	177.3
	DFT	52.2	40.2	54.8	1.42	1.48	1.42	179.2	173.6	-48.8	-29.8	57.5	1.41	1.47	1.41	179.8	172.0
<b>G</b>	MD	-52.8	-25.0	55.6	1.42	1.46	1.42	177.0	173.2	53.7	14.5	-32.8	1.33	1.48	1.37	169.3	151.9
	DFT	-37.3	-31.6	48.7	1.41	1.48	1.41	178.8	178.2	45.8	32.8	-58.1	1.42	1.48	1.42	173.2	175.9
<b>H</b>	MD	-59.3	8.8	-60.0	1.37	1.49	1.41	175.3	173.0	-55.0	-28.1	-39.8	1.38	1.49	1.33	174.7	172.0
	DFT	-61.8	21.1	-51.5	1.42	1.47	1.41	178.8	178.6	-50.9	-34.8	-44.7	1.42	1.47	1.41	178.6	173.1

<sup>a</sup> Dihedral angle

<sup>b</sup> Bond distance

<sup>c</sup> Carbazole angle

## Bibliography

- [1] C. Adachi, M. A. Baldo, M. E. Thompson, S. R. Forrest, *J. Appl. Phys.* **2001**, *90*, 5048–5051.
- [2] F. Laquai, Y. S. Park, J. J. Kim, T. Basché, *Macromol. Rapid Comm.* **2009**, *30*, 1203–1231.
- [3] S. Scholz, D. Kondakov, B. Lüssem, K. Leo, *Chem. Rev.* **2015**, *115*, 8449–8503.
- [4] Q. Wang, B. Sun, H. Aziz, *Adv. Funct. Mater.* **2014**, *24*, 2975–2985.
- [5] R. Gedam, N. T. Kalyani, S. Dhoble in *Energy Materials*, (Eds.: S. Dhoble, N. Kalyani, B. Vengadaesvaran, A. Kariem Arof), Elsevier, **2021**, pp. 3–26.
- [6] P. Strohriegl, D. Wagner, P. Schrögel, S. T. Hoffmann, A. Köhler, U. Heine-meyer, I. Münster in SPIE Proceedings, *Vol. 8829*, (Eds.: F. So, C. Adachi), International Society for Optics and Photonics, **2013**, p. 882906.
- [7] S. A. Bagnich, A. Rudnick, P. Schroegel, P. Strohriegl, A. Köhler, *Philos. Trans. Royal Soc. A* **2015**, *373*, 20140446.
- [8] Y. Tao, C. Yang, J. Qin, *Chem. Soc. Rev.* **2011**, *40*, 2943–2970.
- [9] H. Yu, Y. Zhang, Y. J. Cho, H. Aziz, *ACS Appl. Mater. Interfaces* **2017**, *9*, 14145–14152.
- [10] J. H. Jou, M. F. Hsu, W. B. Wang, C. L. Chin, Y. C. Chung, C. T. Chen, J. J. Shyue, S. M. Shen, M. H. Wu, W. C. Chang, C. P. Liu, S. Z. Chen, H. Y. Chen, *Chem. Mater.* **2009**, *21*, 2565–2567.
- [11] D. Jacquemin, D. Escudero, *Chem. Sci.* **2017**, *8*, 7844–7850.
- [12] W. Song, J. Y. Lee, T. Kim, Y. Lee, H. Jeong, *Adv. Polym. Sci.* **2018**, *57*, 158–164.
- [13] D. Y. Kondakov, W. C. Lenhart, W. F. Nichols, *J. Appl. Phys.* **2007**, *101*, 024512.
- [14] D. Y. Kondakov, T. D. Pawlik, W. F. Nichols, W. C. Lenhart, *J. Soc. Inf. Disp.* **2008**, *16*, 37.

- [15] Q. Wang, H. Aziz, *Adv. Polym. Sci.* **2015**, *26*, 464–470.
- [16] Y. Zhang, H. Aziz, *ACS Appl. Mater. Interfaces* **2017**, *9*, 636–643.
- [17] T. Setzer, P. Friederich, V. Meded, W. Wenzel, C. Lennartz, A. Dreuw, *ChemPhysChem* **2018**, *19*, 2961–2966.
- [18] Y. Zhang, H. Aziz, *ACS Appl. Mater. Interfaces* **2016**, *8*, 14088–14095.
- [19] W. Song, J. Y. Lee, *Adv. Opt. Mater.* **2017**, *5*, 1600901.
- [20] S. Kim, H. J. Bae, S. Park, W. Kim, J. Kim, J. S. Kim, Y. Jung, S. Sul, S. G. Ihn, C. Noh, S. Kim, Y. You, *Nat. Commun.* **2018**, *9*, 1–11.
- [21] S. Inanlou, R. Cortés-Mejía, A. D. Özdemir, S. Höfener, W. Klopper, W. Wenzel, W. Xie, M. Elstner, *Phys. Chem. Chem. Phys.* **2022**, *24*, 4576–4587.
- [22] A. Dreuw, M. Head-Gordon, *Chem. Rev.* **2005**, *105*, 4009–4037.
- [23] P. F. Loos, A. Scemama, D. Jacquemin, *J. Phys. Chem. Lett.* **2020**, *11*, 2374–2383.
- [24] M. Huix-Rotllant, N. Ferré, M. Barbatti in *Quantum Chemistry and Dynamics of Excited States*, John Wiley & Sons, Ltd, **2020**, Chapter 2, pp. 13–46.
- [25] A. Dreuw, J. L. Weisman, M. Head-Gordon, *J. Chem. Phys.* **2003**, *119*, 2943–2946.
- [26] A. Dreuw, M. Head-Gordon, *J. Am. Chem. Soc.* **2004**, *126*, 4007–4016.
- [27] T. Ziegler, M. Seth, M. Krykunov, J. Autschbach, F. Wang, *J. Mol. Struct.: THEOCHEM* **2009**, *914*, 106–109.
- [28] M. E. Casida, *J. Mol. Struct.: THEOCHEM* **2009**, *914*, 3–18.
- [29] X. Blase, C. Attaccalite, *Appl. Phys. Lett.* **2011**, *99*, 171909.
- [30] I. Duchemin, T. Deutsch, X. Blase, *Phys. Rev. Lett.* **2012**, *109*, 167801.
- [31] X. Gui, C. Holzer, W. Klopper, *J. Chem. Theory. Comput.* **2018**, *14*, 2127–2136.
- [32] M. Sparta, F. Neese, *Chem Soc Rev* **2014**, *43*, 5032–5041.
- [33] S. A. Bagnich, S. Athanasopoulos, A. Rudnick, P. Schroegel, I. Bauer, N. C. Greenham, P. Strohriegl, A. Köhler, *J. Phys. Chem. C* **2015**, *119*, 2380–2387.
- [34] W. Koch, M. C. Holthausen, *A Chemist’s Guide to Density Functional Theory*, Wiley, **2001**.

- [35] F. Jensen, *Introduction to computational chemistry*, John Wiley & Sons, **2007**, p. 599.
- [36] D. P. Tew, W. Klopper, T. Helgaker, *J. Comput. Chem.* **2007**, *28*, 1307–1320.
- [37] E. Lewars, *Computational Chemistry: Introduction to the Theory and Applications of Molecular and Quantum Mechanics*, Springer Netherlands, **2010**.
- [38] A. Szabo, N. Ostlund, *Modern Quantum Chemistry: Introduction to Advanced Electronic Structure Theory*, Dover Publications, **1996**.
- [39] R. J. Bartlett, J. F. Stanton in *Reviews in Computational Chemistry*, John Wiley & Sons, Ltd, **1994**, Chapter 2, pp. 65–169.
- [40] M. Head-Gordon, R. J. Rico, M. Oumi, T. J. Lee, *Chem. Phys. Lett.* **1994**, *219*, 21–29.
- [41] S. Grimme in *Reviews in Computational Chemistry, Vol. 20*, Wiley-VCH, **2004**, pp. 153–218.
- [42] A. Dreuw, M. Wormit, *WIREs Comput. Mol. Sci.* **2015**, *5*, 82–95.
- [43] J. Schirmer, *Phys. Rev. A* **1982**, *26*, 2395.
- [44] A. B. Trofimov, I. L. Krivdina, J. Weller, J. Schirmer, *Chem. Phys.* **2006**, *329*, 1–10.
- [45] C. Møller, M. S. Plesset, *Phys. Rev.* **1934**, *46*, 618–622.
- [46] J. Schirmer, A. B. Trofimov, *J. Chem. Phys.* **2004**, *120*, 11449.
- [47] H. Li, R. Nieman, A. J. Aquino, H. Lischka, S. Tretiak, *J. Chem. Theory. Comput.* **2014**, *10*, 3280–3289.
- [48] C. M. Krauter, M. Pernpointner, A. Dreuw, *J. Chem. Phys.* **2013**, *138*, 044107.
- [49] Y. Jung, R. C. Lochan, A. D. Dutoi, M. Head-Gordon, *J. Chem. Phys.* **2004**, *121*, 9793.
- [50] N. O. Winter, C. Hättig, *J. Chem. Phys.* **2011**, *134*, 184101.
- [51] P. Hohenberg, W. Kohn, *Phys. Rev.* **1964**, *136*, B864–B871.
- [52] W. Kohn, L. J. Sham, *Phys. Rev.* **1965**, *140*, A1133–A1138.
- [53] E. Runge, E. K. U. Gross, *Phys. Rev. Lett.* **1984**, *52*, 997–1000.
- [54] C. Ullrich, *Time-Dependent Density-Functional Theory: Concepts and Applications*, Oxford University Press, **2012**.
- [55] S. Hirata, M. Head-Gordon, *Chem Phys Lett* **1999**, *314*, 291–299.

- [56] N. S. Hill, M. L. Coote in *Annual Reports in Computational Chemistry*, (Ed.: D. A. Dixon), Annual Reports in Computational Chemistry, Elsevier, **2019**, pp. 203–285.
- [57] S. Kümmel, *Adv. Energy. Mater.* **2017**, *7*, 1700440.
- [58] M. E. Casida, F. Gutierrez, J. Guan, F.-X. Gadea, D. Salahub, J.-P. Daudey, *J. Chem. Phys.* **2000**, *113*, 7062.
- [59] M. J. Peach, M. J. Williamson, D. J. Tozer, *J Chem Theory Comput* **2011**, *7*, 3578–3585.
- [60] M. J. Peach, N. Warner, D. J. Tozer, *Mol Phys* **2013**, *111*, 1271–1274.
- [61] K. Krause, W. Klopper, *J. Comput. Chem.* **2017**, *38*, 383–388.
- [62] D. Golze, M. Dvorak, P. Rinke, *Front. Chem.* **2019**, *7*, 377.
- [63] F. Aryasetiawan, O. Gunnarsson, *Rep. Prog. Phys.* **1998**, *61*, 237–312.
- [64] G. Onida, L. Reining, A. Rubio, *Rev. Mod. Phys.* **2002**, *74*, 601–659.
- [65] L. Hedin, *Phys. Rev.* **1965**, *139*, A796–A823.
- [66] X. Blase, I. Duchemin, D. Jacquemin, P. F. Loos, *J. Phys. Chem. Lett.* **2020**, *11*, 7371–7382.
- [67] S. Höfener, *J. Comput. Chem.* **2014**, *35*, 1716–1724.
- [68] S. Höfener, A. S. P. Gomes, L. Visscher, *J. Chem. Phys.* **2013**, *139*, 104106.
- [69] A. S. P. Gomes, C. R. Jacob, *Annu. Rep. Prog. Chem. Sect. C: Phys. Chem.* **2012**, *108*, 222–277.
- [70] J. Neugebauer, *Phys. Rep.* **2010**, *489*, 1–87.
- [71] S. Höfener, A. S. P. Gomes, L. Visscher, *J. Chem. Phys.* **2012**, *136*, 044104.
- [72] J. Neugebauer, *J. Chem. Phys.* **2007**, *126*, 134116.
- [73] TURBOMOLE V7.4 2019, a development of University of Karlsruhe and Forschungszentrum Karlsruhe GmbH, 1989-2007, TURBOMOLE GmbH, since 2007. <http://www.turbomole.com>.

- [74] S. G. Balasubramani, G. P. Chen, S. Coriani, M. Diedenhofen, M. S. Frank, Y. J. Franzke, F. Furche, R. Grotjahn, M. E. Harding, C. Hättig, A. Hellweg, B. Helmich-Paris, C. Holzer, U. Huniar, M. Kaupp, A. M. Khah, S. K. Khani, T. Müller, F. Mack, B. D. Nguyen, S. M. Parker, E. Perlt, D. Rappoport, K. Reiter, S. Roy, M. Rückert, G. Schmitz, M. Sierka, E. Tapavicza, D. P. Tew, C. V. Wüllen, V. K. Voora, F. Weigend, A. Wodyński, J. M. Yu, *J. Chem. Phys.* **2020**, *152*, 184107.
- [75] O. Treutler, R. Ahlrichs, *J. Chem. Phys.* **1995**, *102*, 346–354.
- [76] M. Von Arnim, R. Ahlrichs, *J. Comput. Chem.* **1998**, *19*, 1746–1757.
- [77] J. P. Perdew, K. Burke, M. Ernzerhof, *Phys Rev Lett* **1996**, *77*, 3865–3868.
- [78] C. Adamo, V. Barone, *J. Chem. Phys.* **1999**, *110*, 6158–6170.
- [79] F. Weigend, R. Ahlrichs, *Phys. Chem. Chem. Phys.* **2005**, *7*, 3297–3305.
- [80] K. Eichkorn, O. Treutler, H. Öhm, M. Häser, R. Ahlrichs, *Chem. Phys. Lett.* **1995**, *242*, 652–660.
- [81] K. Eichkorn, F. Weigend, O. Treutler, R. Ahlrichs, *Theor. Chem. Acc.* **1997**, *97*, 119–124.
- [82] F. Weigend, *Phys. Chem. Chem. Phys.* **2006**, *8*, 1057–1065.
- [83] P. Deglmann, K. May, F. Furche, R. Ahlrichs, *Chem. Phys. Lett.* **2004**, *384*, 103–107.
- [84] C. Holzer, W. Klopper, *J. Chem. Phys.* **2019**, *150*, 204116.
- [85] R. Bauernschmitt, R. Ahlrichs, *Chem. Phys. Lett.* **1996**, *256*, 454–464.
- [86] R. Bauernschmitt, M. Häser, O. Treutler, R. Ahlrichs, *Chem. Phys. Lett.* **1997**, *264*, 573–578.
- [87] F. Furche, D. Rappoport in *Computational Photochemistry*, (Ed.: M. Olivucci), Elsevier Science, Oxford, **2005**, Chapter 3, pp. 93–128.
- [88] F. Furche, R. Ahlrichs, *J. Chem. Phys.* **2002**, *117*, 7433–7447.
- [89] D. Rappoport, F. Furche, *J. Chem. Phys.* **2005**, *122*, 064105.
- [90] M. J. Van Setten, F. Weigend, F. Evers, *J. Chem. Theory. Comput.* **2013**, *9*, 232–246.
- [91] S. T. Hoffmann, P. Schrögel, M. Rothmann, R. Q. Albuquerque, P. Strohriegl, A. Köhler, *J. Phys. Chem. B* **2011**, *115*, 414–421.

- [92] M. Kühn, F. Weigend, *J. Chem. Phys.* **2014**, *141*, DOI [10.1063/1.4902013](https://doi.org/10.1063/1.4902013).
- [93] I. G. Hill, A. Kahn, *J. Appl. Phys.* **1998**, *84*, 5583–5586.
- [94] Z. B. Wang, M. G. Helander, J. Qiu, Z. W. Liu, M. T. Greiner, Z. H. Lu, *J. Appl. Phys.* **2010**, *108*, 024510.
- [95] E. Louis, E. San-Fabián, M. A. Díaz-García, G. Chiappe, J. A. Vergés, *J. Phys. Chem. Lett.* **2017**, *8*, 2445–2449.
- [96] T. Yanai, D. P. Tew, N. C. Handy, *Chem. Phys. Lett.* **2004**, *393*, 51–57.
- [97] J. D. Chai, M. Head-Gordon, *J. Chem. Phys.* **2008**, *128*, 084106.
- [98] D. Rappoport, F. Furche, *J. Chem. Phys.* **2010**, *133*, 134105.
- [99] M. Sierka, A. Hogekamp, R. Ahlrichs, *J. Chem. Phys.* **2003**, *118*, 9136–9148.
- [100] E. Caldeweyher, C. Bannwarth, S. Grimme, *J. Chem. Phys.* **2017**, *147*, 034112.
- [101] E. Caldeweyher, S. Ehlert, A. Hansen, H. Neugebauer, S. Spicher, C. Bannwarth, S. Grimme, *J. Chem. Phys.* **2019**, *150*, 154122.
- [102] M. Häser, R. Ahlrichs, *J Comput Chem* **1989**, *10*, 104–111.
- [103] F. Weigend, *J Comput Chem* **2008**, *29*, 167–175.
- [104] P. Plessow, F. Weigend, *J Comput Chem* **2012**, *33*, 810–816.
- [105] C. Holzer, *J. Chem. Phys.* **2020**, *153*, DOI [10.1063/5.0022755](https://doi.org/10.1063/5.0022755).
- [106] C. Hättig, *Adv Quantum Chem* **2005**, *50*, 37–60.
- [107] C. Hättig, F. Weigend, *J. Chem. Phys.* **2000**, *113*, 5154.
- [108] C. Hättig, A. Hellweg, A. Köhn, *Phys Chem Chem Phys* **2006**, *8*, 1159–1169.
- [109] A. Hellweg, D. Rappoport, *Phys Chem Chem Phys* **2015**, *17*, 1010–1017.
- [110] N. O. Winter, C. Hättig, *Chem Phys* **2012**, *401*, 217–227.
- [111] G. Schmitz, B. Helmich, C. Hättig, *Mol Phys* **2013**, *111*, 2463–2476.
- [112] B. Helmich, C. Hättig, *J. Chem. Phys.* **2013**, *139*, 084114.
- [113] C. Hättig, D. P. Tew, B. Helmich, *J. Chem. Phys.* **2012**, *136*, 204105.

- 
- [114] B. Hourahine, B. Aradi, V. Blum, F. Bonafé, A. Buccheri, C. Camacho, C. Cevallos, M. Y. Deshayé, T. Dumitrica, A. Dominguez, S. Ehlert, M. Elstner, T. van der Heide, J. Hermann, S. Irle, J. J. Kranz, C. Köhler, T. Kowalczyk, T. Kubar, I. S. Lee, V. Lutsker, R. J. Maurr, S. K. Min, I. Mitchell, C. Negre, T. A. Niehaus, A. M. N. Niklasson, A. J. Page, A. Pecchia, G. Penazzi, M. P. Persson, J. Rezáč, C. G. Sánchez, M. Sternberg, Stöhr, F. Stuckenberg, A. Tkatchenko, V. W.-z. Yu, T. Frauenheim, *J. Chem. Phys.* **2020**, *152*, 124101.
- [115] N. Schieschke, B. M. Bold, P. M. Dohmen, D. Wehl, M. Hoffmann, A. Dreuw, M. Elstner, S. Höfener, *J. Comput. Chem.* **2021**, DOI [10.1002/jcc.26552](https://doi.org/10.1002/jcc.26552).
- [116] S. Laricchia, E. Fabiano, F. D. Sala, *J. Chem. Phys.* **2010**, *133*, 164111.
- [117] S. Laricchia, E. Fabiano, L. A. Constantin, F. D. Sala, *J Chem Theory Comput* **2011**, *7*, 2439–2451.
- [118] L. A. Constantin, E. Fabiano, S. Laricchia, F. D. Sala, *Phys Rev Lett* **2011**, *106*, 186406.
- [119] K. A. Kistler, F. C. Spano, S. Matsika, *J. Phys. Chem. B* **2013**, *117*, 2032–2044.



# Acronyms and Abbreviations

- GW-BSE** Bethe-Salpeter equation based on the  $GW$  approximation to Green's single-particle function
- $J$**  Excitonic coupling
- ADC(2)** Algebraic-diagrammatic construction to second order
- BPh** Biphenyl
- BSE** Bethe-Salpeter equation
- CBP** 4,4'-bis(carbazol-9-yl)biphenyl
- CBZ** Carbazole
- CIS(D)** Configuration interaction with singles and perturbative doubles
- CT** Charge transfer
- DFT** Density Functional Theory
- evGW** Eigenvalue-only self consistent  $GW$  method
- FDE** Frozen Density Embedding
- HF** Hartree-Fock theory
- HOMO** Highest Occupied Molecular Orbital
- IE** Ionization energy
- LT-SOS** Laplace-transformed scaled opposite-spin
- LUMO** Lowest Occupied Molecular Orbital
- MAD** Mean absolute deviation
- MD** Molecular dynamics
- MRD** Mean relative difference
- OLED** Organic light emitting diode
- Ph** Phenyl
- PhOLED** Phosphorescent organic light emitting diode

**PNO** Pair natural orbital

**PNO-ADC2** Pair natural orbital based ADC(2)

**QP** Quasiparticle

**TD-DFT** Time-Dependent Density Functional Theory

**TD-LC-DFTB** Time-Dependent Long-range Corrected Density Functional based Tight Binding

## Permissions to Print

This work contains material adapted from work previously published in scientific journals. Permissions for reuse or reprint of the relevant content has been granted by the copyright owner.

- Chapters 3 and 4: Partially adapted from from *Effects of rotational conformation on electronic properties of 4,4'-bis(carbazol-9-yl)biphenyl (CBP): the single-molecule picture and beyond*. R. Cortés-Mejía, S. Höfener, W. Klopper, *Molecular Physics*. **119**, e1876936, (2021). ©Copyright 2021, reprinted by permission of Informa UK Limited, trading as Taylor & Taylor & Francis Group, <http://www.tandfonline.com>.



## List of Publications

- *Effects of rotational conformation on electronic properties of 4,4'-bis(carbazol-9-yl)biphenyl (CBP): the single-molecule picture and beyond.* R. Cortés-Mejía, S. Höfener, W. Klopper, *Mol. Phys.* **119**, e1876936, (2021)
- *Understanding excited state properties of host materials in OLEDs: Simulation of absorption spectrum of amorphous 4,4'-bis(carbazol-9-yl)-2,2-biphenyl (CBP).* S. Inanlou, R. Cortés-Mejía, A. D. Özdemir, S. Höfener, W. Klopper, W. Wenzel, W. Xie, M. Elstner, *Phys. Chem. Chem. Phys.*, **24**, 4576 ,(2022)



# Acknowledgments

First, I would like to express my gratitude to my supervisor Sebastian Höfener, for his continuous support and encouragement throughout my PhD at KIT. Thanks for all the insightful discussions, the guidance, and patience. I also want to thank Professor Wim Klopper for giving me the chance to join the Theoretical Chemistry Group at KIT. I am very grateful for the the motivation, advice, and shared knowledge.

I would like to thank Professors Marcus Elstner and Wolfgang Wenzel for the project discussions and helpful input. A special thanks goes to Samaneh Inanlou and A. Deniz Özdemir, for all the support and great collaborations. I've really enjoyed working alongside you.

A huge thanks to my colleagues in the TC Group, and to all members of the RTG/GRK2450 for the scientific and non-scientific discussions. Also, thanks to Sabine Holthoff, and Manuela Kühn for all the support on the administrative matters.

Further, I want to thank Max Kehry, Jing Liu, Ansgar Pausch, and Andrea Enríquez for proofreading this work, and for the several helpful discussions and comments.

I am grateful for the financial support provided through the Research Training Group (RTG/GRK) 2450 "Tailored Scale-Bridging Approaches to Computational Nanoscience", funded by the Deutsche Forschungsgemeinschaft (DFG).

To all my friends, new and old, thanks for being there. I want to thank my family for always believing in me, and for all the encouragement and support. Finally, thanks to my wife, Andrea, for being who she is, and for everything through all these years.